DESY-00-181 ISSN 0418-9833
December 2000

Deep-Inelastic Inclusive ep Scattering at Low x and a Determination of α_s

H1 Collaboration

Abstract:

A precise measurement of the inclusive deep-inelastic e^+p scattering cross section is reported in the kinematic range $1.5 \leq Q^2 \leq 150\,\mathrm{GeV}^2$ and $3 \cdot 10^{-5} \leq x \leq 0.2$. The data were recorded with the H1 detector at HERA in 1996 and 1997, and correspond to an integrated luminosity of $20\,\mathrm{pb}^{-1}$. The double differential cross section, from which the proton structure function $F_2(x, Q^2)$ and the longitudinal structure function $F_L(x, Q^2)$ are extracted, is measured with typically 1% statistical and 3% systematic uncertainties. The measured derivative $(\partial F_2(x, Q^2)/\partial \ln Q^2)_x$ is observed to rise continuously towards small x for fixed Q^2. The cross section data are combined with published H1 measurements at high Q^2 for a next-to-leading order DGLAP QCD analysis. The H1 data determine the gluon momentum distribution in the range $3 \cdot 10^{-4} \leq x \leq 0.1$ to within an experimental accuracy of about 3% for $Q^2 = 20\,\mathrm{GeV}^2$. A fit of the H1 measurements and the μp data of the BCDMS collaboration allows the strong coupling constant α_s and the gluon distribution to be simultaneously determined. A value of $\alpha_s(M_Z^2) = 0.1150 \pm 0.0017(exp)^{+0.0009}_{-0.0005}\ (model)$ is obtained in NLO, with an additional theoretical uncertainty of about ± 0.005, mainly due to the uncertainty of the renormalisation scale.

To be submitted to Eur. Phys. J. C

C. Adloff[33], V. Andreev[24], B. Andrieu[27], T. Anthonis[4], V. Arkadov[35], A. Astvatsatourov[35], I. Ayyaz[28], A. Babaev[23], J. Bähr[35], P. Baranov[24], E. Barrelet[28], W. Bartel[10], U. Bassler[28], P. Bate[21], A. Beglarian[34], O. Behnke[13], C. Beier[14], A. Belousov[24], T. Benisch[10], Ch. Berger[1], G. Bernardi[28], T. Berndt[14], J.C. Bizot[26], V. Boudry[27], W. Braunschweig[1], V. Brisson[26], H.-B. Bröker[2], D.P. Brown[11], W. Brückner[12], P. Bruel[27], D. Bruncko[16], J. Bürger[10], F.W. Büsser[11], A. Bunyatyan[12,34], H. Burkhardt[14], A. Burrage[18], G. Buschhorn[25], A.J. Campbell[10], J. Cao[26], T. Carli[25], S. Caron[1], E. Chabert[22], D. Clarke[5], B. Clerbaux[4], C. Collard[4], J.G. Contreras[7,41], Y.R. Coppens[3], J.A. Coughlan[5], M.-C. Cousinou[22], B.E. Cox[21], G. Cozzika[9], J. Cvach[29], J.B. Dainton[18], W.D. Dau[15], K. Daum[33,39], M. Davidsson[20], B. Delcourt[26], N. Delerue[22], R. Demirchyan[34], A. De Roeck[10,43], E.A. De Wolf[4], C. Diaconu[22], P. Dixon[19], V. Dodonov[12], J.D. Dowell[3], A. Droutskoi[23], C. Duprel[2], G. Eckerlin[10], D. Eckstein[35], V. Efremenko[23], S. Egli[32], R. Eichler[36], F. Eisele[13], E. Eisenhandler[19], M. Ellerbrock[13], E. Elsen[10], M. Erdmann[10,40,e], W. Erdmann[36], P.J.W. Faulkner[3], L. Favart[4], A. Fedotov[23], R. Felst[10], J. Ferencei[10], S. Ferron[27], M. Fleischer[10], Y.H. Fleming[3], G. Flügge[2], A. Fomenko[24], I. Foresti[37], J. Formánek[30], J.M. Foster[21], G. Franke[10], E. Gabathuler[18], K. Gabathuler[32], J. Garvey[3], J. Gassner[32], J. Gayler[10], R. Gerhards[10], S. Ghazaryan[34], A. Glazov[35,44] L. Goerlich[6], N. Gogitidze[24], M. Goldberg[28], C. Goodwin[3], C. Grab[36], H. Grässler[2], T. Greenshaw[18], G. Grindhammer[25], T. Hadig[13], D. Haidt[10], L. Hajduk[6], W.J. Haynes[5], B. Heinemann[18], G. Heinzelmann[11], R.C.W. Henderson[17], S. Hengstmann[37], H. Henschel[35], R. Heremans[4], G. Herrera[7,41], I. Herynek[29], M. Hildebrandt[37], M. Hilgers[36], K.H. Hiller[35], J. Hladký[29], P. Höting[2], D. Hoffmann[10], W. Hoprich[12], R. Horisberger[32], S. Hurling[10], M. Ibbotson[21], Ç. İşsever[7], M. Jacquet[26], M. Jaffre[26], L. Janauschek[25], D.M. Jansen[12], X. Janssen[4], V. Jemanov[11], L. Jönsson[20], D.P. Johnson[4], M.A.S. Jones[18], H. Jung[20], H.K. Kästli[36], D. Kant[19], M. Kapichine[8], M. Karlsson[20], O. Karschnick[11], F. Keil[14], N. Keller[37], J. Kennedy[18], I.R. Kenyon[3], S. Kermiche[22], C. Kiesling[25], M. Klein[35], C. Kleinwort[10], G. Knies[10], B. Koblitz[25], S.D. Kolya[21], V. Korbel[10], P. Kostka[35], S.K. Kotelnikov[24], R. Koutouev[12], A. Koutov[8], M.W. Krasny[28], H. Krehbiel[10], J. Kroseberg[37], K. Krüger[10], A. Küpper[33], T. Kuhr[11], T. Kurča[35,16], R. Lahmann[10], D. Lamb[3], M.P.J. Landon[19], W. Lange[35], T. Laštovička[30], E. Lebailly[26], A. Lebedev[24], B. Leißner[1], R. Lemrani[10], V. Lendermann[7], S. Levonian[10], M. Lindstroem[20], B. List[36], E. Lobodzinska[10,6], B. Lobodzinski[6,10], A. Loginov[23], N. Loktionova[24], V. Lubimov[23], S. Lüders[36], D. Lüke[7,10], L. Lytkin[12], N. Magnussen[33], H. Mahlke-Krüger[10], N. Malden[21], E. Malinovski[24], I. Malinovski[24], R. Maraček[25], P. Marage[4], J. Marks[13], R. Marshall[21], H.-U. Martyn[1], J. Martyniak[6], S.J. Maxfield[18], A. Mehta[18], K. Meier[14], P. Merkel[10], F. Metlica[12], A.B. Meyer[11], H. Meyer[33], J. Meyer[10], P.-O. Meyer[2], S. Mikocki[6], D. Milstead[18], T. Mkrtchyan[34], R. Mohr[25], S. Mohrdieck[11], M.N. Mondragon[7], F. Moreau[27], A. Morozov[8], J.V. Morris[5], K. Müller[13], P. Murín[16,42], V. Nagovizin[23], B. Naroska[11], J. Naumann[7], Th. Naumann[35], G. Nellen[25], P.R. Newman[3], T.C. Nicholls[5], F. Niebergall[11], C. Niebuhr[10], O. Nix[14], G. Nowak[6], T. Nunnemann[12], J.E. Olsson[10], D. Ozerov[23], V. Panassik[8], C. Pascaud[26], G.D. Patel[18], E. Perez[9], J.P. Phillips[18], D. Pitzl[10], R. Pöschl[7], I. Potachnikova[12], B. Povh[12], K. Rabbertz[1], G. Rädel[9], J. Rauschenberger[11], P. Reimer[29], B. Reisert[25], D. Reyna[10], S. Riess[11], C. Risler[25], E. Rizvi[3], P. Robmann[37], R. Roosen[4], A. Rostovtsev[23], C. Royon[9], S. Rusakov[24], K. Rybicki[6], D.P.C. Sankey[5], J. Scheins[1], F.-P. Schilling[13], P. Schleper[13], D. Schmidt[33], D. Schmidt[10], S. Schmitt[10], L. Schoeffel[9], A. Schöning[36], T. Schörner[25], V. Schröder[10], H.-C. Schultz-Coulon[7], C. Schwanenberger[10], K. Sedlák[29], F. Sefkow[37], V. Shekelyan[25], I. Sheviakov[24], L.N. Shtarkov[24], G. Siegmon[15], P. Sievers[13], Y. Sirois[27], T. Sloan[17], P. Smirnov[24], V. Solochenko[23,†], Y. Soloviev[24], V. Spaskov[8], A. Specka[27], H. Spitzer[11], R. Stamen[7], J. Steinhart[11],

B. Stella[31], A. Stellberger[14], J. Stiewe[14], U. Straumann[37], W. Struczinski[2], M. Swart[14], M. Taševský[29], V. Tchernyshov[23], S. Tchetchelnitski[23], G. Thompson[19], P.D. Thompson[3], N. Tobien[10], D. Traynor[19], P. Truöl[37], G. Tsipolitis[10,38], I. Tsurin[35], J. Turnau[6], J.E. Turney[19], E. Tzamariudaki[25], S. Udluft[25], A. Usik[24], S. Valkár[30], A. Valkárová[30], C. Vallée[22], P. Van Mechelen[4], S. Vassiliev[8], Y. Vazdik[24], A. Vichnevski[8], S. von Dombrowski[37], K. Wacker[7], R. Wallny[37], T. Walter[37], B. Waugh[21], G. Weber[11], M. Weber[14], D. Wegener[7], M. Werner[13], G. White[17], S. Wiesand[33], T. Wilksen[10], M. Winde[35], G.-G. Winter[10], C. Wissing[7], M. Wobisch[2], H. Wollatz[10], E. Wünsch[10], A.C. Wyatt[21], J. Žáček[30], J. Zálešák[30], Z. Zhang[26], A. Zhokin[23], F. Zomer[26], J. Zsembery[9], and M. zur Nedden[10]

[1] *I. Physikalisches Institut der RWTH, Aachen, Germany*[a]
[2] *III. Physikalisches Institut der RWTH, Aachen, Germany*[a]
[3] *School of Physics and Space Research, University of Birmingham, Birmingham, UK*[b]
[4] *Inter-University Institute for High Energies ULB-VUB, Brussels; Universitaire Instelling Antwerpen, Wilrijk; Belgium*[c]
[5] *Rutherford Appleton Laboratory, Chilton, Didcot, UK*[b]
[6] *Institute for Nuclear Physics, Cracow, Poland*[d]
[7] *Institut für Physik, Universität Dortmund, Dortmund, Germany*[a]
[8] *Joint Institute for Nuclear Research, Dubna, Russia*
[9] *CEA, DSM/DAPNIA, CE-Saclay, Gif-sur-Yvette, France*
[10] *DESY, Hamburg, Germany*[a]
[11] *II. Institut für Experimentalphysik, Universität Hamburg, Hamburg, Germany*[a]
[12] *Max-Planck-Institut für Kernphysik, Heidelberg, Germany*[a]
[13] *Physikalisches Institut, Universität Heidelberg, Heidelberg, Germany*[a]
[14] *Kirchhoff-Institut für Physik, Universität Heidelberg, Heidelberg, Germany*[a]
[15] *Institut für experimentelle und angewandte Kernphysik, Universität Kiel, Kiel, Germany*[a]
[16] *Institute of Experimental Physics, Slovak Academy of Sciences, Košice, Slovak Republic*[e,f]
[17] *School of Physics and Chemistry, University of Lancaster, Lancaster, UK*[b]
[18] *Department of Physics, University of Liverpool, Liverpool, UK*[b]
[19] *Queen Mary and Westfield College, London, UK*[b]
[20] *Physics Department, University of Lund, Lund, Sweden*[g]
[21] *Physics Department, University of Manchester, Manchester, UK*[b]
[22] *CPPM, CNRS/IN2P3 - Univ Mediterranee, Marseille - France*
[23] *Institute for Theoretical and Experimental Physics, Moscow, Russia*
[24] *Lebedev Physical Institute, Moscow, Russia*[e,h]
[25] *Max-Planck-Institut für Physik, München, Germany*[a]
[26] *LAL, Université de Paris-Sud, IN2P3-CNRS, Orsay, France*
[27] *LPNHE, Ecole Polytechnique, IN2P3-CNRS, Palaiseau, France*
[28] *LPNHE, Universités Paris VI and VII, IN2P3-CNRS, Paris, France*
[29] *Institute of Physics, Czech Academy of Sciences, Praha, Czech Republic*[e,i]
[30] *Faculty of Mathematics and Physics, Charles University, Praha, Czech Republic*[e,i]
[31] *Dipartimento di Fisica Università di Roma Tre and INFN Roma 3, Roma, Italy*
[32] *Paul Scherrer Institut, Villigen, Switzerland*
[33] *Fachbereich Physik, Bergische Universität Gesamthochschule Wuppertal, Wuppertal, Germany*[a]
[34] *Yerevan Physics Institute, Yerevan, Armenia*
[35] *DESY, Zeuthen, Germany*[a]

[36] *Institut für Teilchenphysik, ETH, Zürich, Switzerland*[j]
[37] *Physik-Institut der Universität Zürich, Zürich, Switzerland*[j] [38] *Also at Physics Department, National Technical University, Zografou Campus, GR-15773 Athens, Greece*
[39] *Also at Rechenzentrum, Bergische Universität Gesamthochschule Wuppertal, Germany*
[40] *Also at Institut für Experimentelle Kernphysik, Universität Karlsruhe, Karlsruhe, Germany*
[41] *Also at Dept. Fis. Ap. CINVESTAV, Mérida, Yucatán, México*[k]
[42] *Also at University of P.J. Šafárik, Košice, Slovak Republic*
[43] *Also at CERN, Geneva, Switzerland*
[44] *Now at Enrico Fermi Institute, Chicago, USA*
† *Deceased*

[a] *Supported by the Bundesministerium für Bildung, Wissenschaft, Forschung und Technologie, FRG, under contract numbers 7AC17P, 7AC47P, 7DO55P, 7HH17I, 7HH27P, 7HD17P, 7HD27P, 7KI17I, 6MP17I and 7WT87P*
[b] *Supported by the UK Particle Physics and Astronomy Research Council, and formerly by the UK Science and Engineering Research Council*
[c] *Supported by FNRS-NFWO, IISN-IIKW*
[d] *Partially Supported by the Polish State Committee for Scientific Research, grant no. 2P0310318 and SPUB/DESY/P03/DZ-1/99, and by the German Federal Ministry of Education and Science, Research and Technology (BMBF)*
[e] *Supported by the Deutsche Forschungsgemeinschaft*
[f] *Supported by VEGA SR grant no. 2/5167/98*
[g] *Supported by the Swedish Natural Science Research Council*
[h] *Supported by Russian Foundation for Basic Research grant no. 96-02-00019*
[i] *Supported by GA AV ČR grant no. A1010821*
[j] *Supported by the Swiss National Science Foundation*
[k] *Supported by CONACyT*

1 Introduction

Deep-inelastic lepton-nucleon scattering (DIS) has been pivotal in the development of the understanding of strong interaction dynamics. Measurements of the inclusive DIS cross section have been essential for testing Quantum Chromodynamics (QCD) [1]. Previous fixed target DIS experiments have observed scaling violations, i.e. the variation of the structure functions with Q^2, the squared four-momentum transfer between lepton and nucleon, for fixed values of Bjorken-x, which are well described by perturbative QCD. The Q^2 evolution of the proton structure function $F_2(x, Q^2)$ is related to the gluon momentum distribution in the proton, $xg(x, Q^2)$, and to the strong interaction coupling constant, α_s. These can be determined with precision deep-inelastic scattering cross section data measured over a wide range of Bjorken-x and Q^2.

The first measurements of F_2 at low $x \sim 10^{-3}$ and $Q^2 \sim 20$ GeV^2 at HERA revealed a steep rise of $F_2(x, Q^2)$ towards low x for fixed Q^2 [2, 3]. Strong scaling violations are observed at low x and are attributed to a high gluon density in the proton. The validity of the DGLAP evolution equations [4], which neglect higher-order terms [5, 6] proportional to $\alpha_s \cdot \ln(1/x)$, is questionable in the low x range and therefore has to be tested against data. At extremely low x, non-linear gluon interaction effects have been considered in order to damp the rise of the cross section in accordance with unitarity requirements [7]. The study of quark-gluon interaction dynamics at high parton densities therefore continues to be a challenging subject. Knowledge of the parton densities at low x is also necessary for interpreting measurements at hadron colliders and of cosmic neutrino interactions.

This paper presents new cross section measurements for the neutral current process $e^+p \rightarrow e^+X$ in the kinematic region $1.5 \leq Q^2 \leq 150$ GeV^2 and $3 \cdot 10^{-5} \leq x \leq 0.2$, obtained from data taken in the years 1996 and 1997 with positrons of energy $E_e = 27.6$ GeV and protons of energy $E_p = 820$ GeV, corresponding to a centre of mass energy $\sqrt{s} = 300.9$ GeV. Cross section measurements at low x and medium Q^2, based on the 1994 HERA data, were previously published by the H1 collaboration [8] and by the ZEUS collaboration [9]. The present measurement uses upgraded detectors to measure and identify the scattered positron, including new precision tracking for low Q^2 scattering. It also benefits from increased luminosity from HERA which enables an accuracy of typically 3% to be reached for the DIS cross section. Thus it considerably improves the former structure function measurements of the H1 collaboration [8,10,11] at $Q^2 \leq 150$ GeV^2. The kinematic range is extended to larger x, yielding an overlap of H1 data with measurements from fixed target muon-proton scattering experiments for the first time. The paper includes a measurement of the derivative $(\partial F_2/\partial \ln Q^2)_x$, which serves as a sensitive test of the dynamics of strong interactions.

The longitudinal structure function $F_L(x, Q^2)$ is obtained with improved precision in an extended range of inelasticity y and Q^2, as compared to its first determination at low x [11]. A new method is introduced to extend the extraction of F_L to Q^2 values below 10 GeV^2 which uses the derivative $(\partial \sigma_r/\partial \ln y)_{Q^2}$ of the reduced cross section σ_r.

A next-to-leading order (NLO) DGLAP QCD analysis is performed using inclusive lepton-proton scattering data by introducing a new flavour decomposition of the structure function

F_2 . Hence it is independent of nuclear binding effects in the deuteron or heavier nuclei. The QCD analysis of the present low x data and of the recently published high Q^2 H1 data [12] determines the gluon distribution $xg(x, Q^2)$ at low $x \geq 3 \cdot 10^{-4}$. The combination of the low x H1 data with large x data from the BCDMS experiment [13] enables an accurate, simultaneous determination of both $xg(x, Q^2)$ and $\alpha_s(M_Z^2)$. The present analyses use all of the available information regarding the experimental uncertainties of the data sets considered and explore the QCD model and fit parameter variations in a systematic way.

The paper is organised as follows. Section 2 defines the inclusive cross section and the methods used to reconstruct the event kinematics. The detector, the event selection and the simulation are described in section 3. Section 4 presents the alignment and calibration methods, and summarises the cross section measurement. Section 5 presents the measurement of $(\partial\sigma_r/\partial \ln y)_{Q^2}$ and the determination of the longitudinal structure function F_L . The results for the proton structure function F_2 and its derivative $(\partial F_2/\partial \ln Q^2)_x$ are given in section 6. The QCD interpretation of the data is discussed in section 7, which refers to an appendix presenting details of the analysis. The paper is summarised in section 8.

2 Cross Section and Kinematic Reconstruction

The inclusive DIS cross section of the measured reaction $e^+p \rightarrow e^+X$ depends on two independent kinematic variables, chosen to be x and Q^2, and on the centre of mass energy squared s, with the inelasticity variable $y = Q^2/sx$. In the one-photon exchange approximation the neutral current double differential cross section, $d^2\sigma/dxdQ^2$, is given by

$$\frac{d^2\sigma}{dxdQ^2} = \frac{2\pi\alpha^2 Y_+}{Q^4 x} \cdot \sigma_r \tag{1}$$

where the reduced cross section is defined as

$$\sigma_r \equiv F_2(x, Q^2) - \frac{y^2}{Y_+} \cdot F_L(x, Q^2) \tag{2}$$

and $Y_+ = 1 + (1-y)^2$. Due to the positivity of the cross sections for longitudinally and transversely polarised photons scattering off protons, the two proton structure functions F_2 and F_L obey the relation $0 \leq F_L \leq F_2$. Thus the contribution of the longitudinal structure function F_L to the cross section can be sizeable only at large values of the inelasticity y, and in most of the kinematic range the relation $\sigma_r \approx F_2$ holds to a very good approximation.

The HERA collider experiments allow DIS kinematics to be reconstructed using the scattered positron, the hadronic final state, or a combination of the two. This is important for maximum coverage of the kinematic range and the control of systematic uncertainties.

In the "electron method" the event kinematics are determined using the measured energy of the scattered positron E'_e and its polar angle θ_e according to the relations

$$y_e = 1 - \frac{E'_e}{E_e}\,\sin^2(\theta_e/2), \qquad Q^2_e = \frac{E'^2_e \sin^2\theta_e}{1 - y_e}. \tag{3}$$

The coordinate system of H1 is defined such that the positive z axis is in the direction of the incident proton beam. Polar angles θ are defined with respect to the proton beam direction. While the electron method is accurate at large y, corresponding to low E'_e, the resolution rapidly degrades with $1/y$ as E'_e approaches the positron beam energy E_e.

The inelasticity y can also be determined as [14]

$$y_h = \frac{\Sigma_i (E_i - p_{z,i})}{2E_e} \equiv \frac{\Sigma}{2E_e}, \tag{4}$$

where E_i and $p_{z,i}$ are the energy and longitudinal momentum component of a particle i in the hadronic final state, the masses being neglected. In this analysis the kinematics are also reconstructed with the "Σ method" using the variables [15]

$$y_\Sigma = \frac{\Sigma}{\Sigma + E'_e(1-\cos\theta_e)}, \qquad Q^2_\Sigma = \frac{E'^2_e \sin^2\theta_e}{1-y_\Sigma}. \tag{5}$$

For all reconstruction methods, Bjorken-x is calculated as $x = Q^2/sy$. Due to energy-momentum conservation the variable

$$E - p_z = \Sigma + E'_e(1-\cos\theta_e) \tag{6}$$

is approximately equal to $2E_e$. The hadronic variables y_h and y_Σ are related according to

$$y_\Sigma = \frac{y_h}{1 + y_h - y_e} \tag{7}$$

and can be well measured down to low $y \simeq 0.004$. The variable y_Σ is less sensitive to initial state radiation than y_h since the initial energy E_e in the denominator in equation 4 can be calculated using the total energy reconstructed in the detector which leads to equation 5.

The hadronic scattering angle is defined as

$$\tan\frac{\theta_h}{2} = \frac{\Sigma}{P_{t,h}}, \tag{8}$$

where $P_{t,h}$ is the total transverse momentum of the hadronic final state particles. In the naive quark parton model, θ_h defines the direction of the struck quark related to θ_e as

$$\tan\frac{\theta_h}{2} = \frac{y}{1-y} \cdot \tan\frac{\theta_e}{2}. \tag{9}$$

For $y > 0.5$ the positron scattering angle θ_e is smaller than θ_h. This relation, together with the definition of y_e (equation 3), determines the scattered positron energy from θ_e and θ_h in the "double angle method" [16].

3 Experimental Procedure

3.1 H1 Detector

The H1 detector [17] combines tracking in a solenoidal magnetic field of 1.15 T with nearly hermetic calorimetry to investigate high-energy ep interactions at HERA. The low Q^2 cross section measurement relies mainly on the central and backward tracking systems, the backward calorimeter (SPACAL) and the Liquid Argon (LAr) calorimeter. These components are briefly described below.

The energy of the positron, when scattered into the backward region of the H1 detector ($153^\circ < \theta_e < 177^\circ$), is measured in the SPACAL, a lead-fibre calorimeter [18, 19]. The SPACAL has an electromagnetic section with an energy resolution of $7\%/\sqrt{E/GeV} \oplus 1\%$, which together with a hadronic section represents a total of two interaction lengths. The SPACAL time resolution of less than 1 ns allows proton beam induced background to be vetoed. The calorimeter has a high transverse granularity which provides a determination of the transverse coordinates of electromagnetic clusters with an accuracy of a few millimeters and positron identification capability. Identification of the scattered positron is improved and the polar angle measured with a backward drift chamber (BDC), situated in front of the SPACAL, and a new backward silicon strip detector (BST) [20]. The BST consists of four detector planes, arranged perpendicularly to the beam axis which are equipped with 16 wedge shaped, double metal silicon strip detectors. The BST measures the polar angle of tracks with an internal resolution of about 0.2 mrad from radial coordinates between 5.9 cm and 12.0 cm.

The hadronic final state is reconstructed with the Liquid Argon calorimeter [21], the tracking detectors and the SPACAL. The LAr calorimeter is built of eight wheels of modules with an octant structure. The total depth of the calorimeter varies between 4 and 8.5 interaction lengths depending on the polar angle. In test beam measurements pion induced hadronic energies were reconstructed with a resolution of about $50\%/\sqrt{E/GeV} \oplus 2.0\%$ after software energy weighting [22].

The interaction vertex is determined with the central tracking detector consisting of two concentric jet drift chambers (CJC) and two concentric z drift chambers (CIZ and COZ). The vertex determination is complemented by the inner proportional chamber CIP, for $167^\circ < \theta_e < 171^\circ$, and by the silicon tracker BST, for $171^\circ < \theta_e < 176.5^\circ$.

The luminosity is determined using the small-angle bremsstrahlung process $ep \rightarrow ep\,\gamma$. The final state photon and the positron, scattered at very low Q^2, can be detected in calorimeters ("electron and photon taggers") which are situated close to the beam pipe at distances of 33 m and 103 m from the interaction point in the positron beam direction. The luminosity is measured with a precision of 1.5% using the method outlined in [23].

3.2 Data Samples and Interaction Triggers

The analysis comprises two different DIS event samples:

- Sample A - data taken in the years 1996 and 1997 with luminosities of 4.5 pb^{-1} and 13.4 pb^{-1}, respectively. These two data sets are combined to provide the cross section measurement for Q^2 values from 15 GeV^2 to 150 GeV^2 and for $Q^2 = 12\,\mathrm{GeV}^2$ at $y > 0.17$.

- Sample B - data taken in the autumn of 1997 during a two week period dedicated to the lower Q^2 region. The data from this special run with a luminosity of 1.8 pb^{-1} are used in the Q^2 range from 1.5 GeV^2 to 8.5 GeV^2 and for Q^2 =12 GeV^2 at low $y < 0.17$.

DIS events at low Q^2 are characterised by a positron scattered into the backward part of the H1 apparatus. The event trigger for sample A requires local energy sums in the SPACAL calorimeter to be above an energy threshold of 6 GeV. This threshold is lowered to 5 GeV in sample B.

Both data samples are contaminated by photoproduction events in which the scattered positron escapes through the beam pipe and a particle in the hadronic final state mimics the signature of a scattered positron. For a fraction of these background events the scattered positron is detected in the electron tagging calorimeter. This background is significant only at low energies E'_e, corresponding to values of $y > 0.6$.

The region of high $y > 0.75$ is accessed with a dedicated trigger which requires a compact energy deposition (cluster) of more than 2 GeV of energy in the SPACAL, and a vertex signature in the proportional chamber system. The data accumulated with this trigger correspond to a luminosity of 2.8 pb^{-1} in 1996 and 3.4 pb^{-1} in 1997.

The SPACAL energy triggers are monitored with independent track triggers and found to be fully efficient for energies of about 1 GeV above threshold. The high y trigger efficiency is determined to be 97% using independent calorimeter triggers. The online data reconstruction leads to a maximum loss of 0.5% of DIS events. This loss is estimated from monitor data and corrected for.

3.3 Event Selection

The scattered positron is identified with the cluster of maximum transverse momentum p_t in the SPACAL calorimeter, for which requirements on the cluster shape are satisfied. Electromagnetic energy deposition leads to clusters of smaller transverse extension than hadronic energy deposition. The transverse energy distribution of positron showers is determined experimentally using QED Compton events, and from radiative DIS events in which a photon is radiated from the incoming positron and detected in the photon tagger. The positron cluster radius [19, 24] can thus be measured at all energies considered in the analysis, and a cluster radius cut of 4 cm is chosen. This cut removes a sizeable fraction of the photoproduction background while retaining more than 99% of the DIS signal.

A positron candidate cluster is required to be associated with a track segment in the BDC. The efficiency of the BDC is measured to be 98% on average with small radius dependent variations. A signal is also required in either the CIP or the BST where geometrically available. The efficiency of the CIP is about 98%. The track efficiency of the BST in the 1997 special run period is found to be about 93%. Efficiencies at low energies are determined using QED Compton scattering events and radiative DIS events.

Reconstruction of the interaction vertex is necessary to determine the event kinematics and to suppress beam background events. In the intermediate y region, hadrons measured in the central tracking chambers allow vertex reconstruction with an efficiency exceeding 98%. However, at very low y and also at very high y, where no hadron may be measured in the central tracking chambers, the vertex can be defined by the scattered positron if it falls within the acceptance of the CIP or the BST.

SPACAL energy	$>$ 6.9 GeV
radius of cluster	< 4 cm
fraction of energy in the hadronic section	$<$ 15% of E'_e
cluster-BDC track distance	< 1.5 cm
cluster-BST track distance	< 1.0 cm
z vertex position	$\|z\| < 30$ cm
$E - p_z$	> 35 GeV

Table 1: *Basic DIS event selection criteria. The radius of the cluster [19, 24] defines the lateral shape of the energy deposition. The high y region, corresponding to energies between $E'_e = 3$ GeV and 6.9 GeV, is accessed with additional cuts, as discussed in Section 4.3.*

Longitudinal momentum conservation in neutral current DIS events gives the constraint that $E - p_z$, summed over the final state particles is about equal to $2E_e$ (equation 6). In radiative events a photon may carry a significant fraction of the $E - p_z$ sum. Such events are thus suppressed by requiring $E - p_z > 35$ GeV.

The criteria applied to select DIS events are summarised in table 1.

3.4 Simulation

For the calculation of the detector acceptance and efficiency control about 10^7 inelastic events are simulated. Deep-inelastic events are generated using the DJANGO [25] event generator. This program is based on HERACLES [26] for the electroweak interaction and on the Lund Monte Carlo generator program ARIADNE [27], which includes the generation of diffractive events. This generator, when tuned to HERA data [28], presently gives the most reliable description of the final state properties [29]. To describe higher order QCD radiation processes the ARIADNE program uses the Colour Dipole Model (CDM) [30]. For hadron fragmentation the JETSET program is used [31]. Comparisons are done using the generator LEPTO [32]. QED Compton events are generated using the program COMPTON [33]. DIS events are also generated with the HERWIG event generator [34], which includes resonant final state production. This is important for the description of rejected events at very low y [35]. Photoproduction background is generated with the PHOJET [36] program using the parameterisation of CKMT [37] to determine the virtual photon-proton interaction cross section. The normalisation of the PHOJET event sample is adjusted to the data measured with the electron tagging calorimeter. It is found to agree within 20% with the calculation of the cross section using the Weizsäcker-Williams approximation. Using the leading logarithmic approximation [38] the effect of photon radiation is estimated to be negligible.

The detector response is simulated in detail with a program based on GEANT3 [39]. The Monte Carlo events are subject to the same reconstruction and analysis chain as the real data. In the comparisons shown here, the simulated distributions are normalised to the measured luminosity. In the event generation the DIS cross section is calculated with the parton distributions of [40] and with the longitudinal structure function $F_L = 0$. A QCD fit to all the data is used to reweight the simulated cross section.

4 Measurement of the Cross Section

This section presents briefly the methods and results of the measurement of the deep-inelastic scattering cross section. Further details of the analysis are described in [24, 35, 41, 42].

4.1 Detector Alignment

The coordinate system of the H1 detector is defined by the central tracking chambers which determine the spatial coordinates of the interaction vertex. The variation of the vertex position in the x, y plane along the beam direction is used to determine the inclination of the beam axis with respect to the z axis.

The central tracking chambers are aligned with respect to each other using cosmic muon tracks. The alignment of the BDC and of the SPACAL with respect to the central tracker is done by studying the difference of the polar angles measured by these detectors as a function of the azimuthal angle. This results in 1 to 2 mm adjustments of the nominal detector positions. QED Compton events, which have the signature of back-to-back positron and photon clusters, provide a cross check for the alignment [24] of the SPACAL in the transverse plane to an accuracy of 0.2 mm. After internal adjustment of the strip detector planes, the spatial position of the BST is determined using the event vertex z coordinate measured with the central tracker.

In the BST angular acceptance range the polar angle is measured both by the BDC using the interaction vertex, and by the BST track segment. This allows the alignment procedure to be checked to within an accuracy of $\Delta\theta$ of 0.1 mrad [35]. From the residual dependence of $\Delta\theta$ on the azimuthal angle and from the uncertainties of the alignment procedure, a measurement error of 0.3 mrad is estimated for the angle of the scattered positron.

4.2 Calibration of the Energy Measurements

The energy of the scattered positron is measured in the SPACAL, which has a transverse cell size of 4×4 cm^2 and a Molière radius of 2.5 cm. In a first step the responses of the SPACAL cells are equalised using cosmic muons. The energy scale of each cell is determined with DIS events using the double angle method, which allows the energy of the scattered positron to be expressed as a function of θ_e and θ_h. This method is applied to the data of the various run periods, and also to the simulated events. Agreement of the energy scales is found at the level of 0.2%. The calibration procedure leads to a systematic error of the E'_e scale of 0.3% for most of the SPACAL area and energies E'_e above 20 GeV. The energy calibration at lower energies is performed using QED Compton events. This leads to an estimated maximum energy scale uncertainty of 2.7% at 3 GeV. This uncertainty is observed to approach linearly the 0.3% level at maximum energies $E'_e \simeq E_e$. The SPACAL response at the lowest energies is cross checked by studying the π^0 mass reconstructed from pairs of photons in the energy range of $0.8 - 4$ GeV [24, 43]. Material in front of the calorimeter leads to showering and energy losses, which are corrected for using the backward drift chamber as a preshower detector [41]. Figures 1a,b and 2a,b show the energy and polar angle distributions for data samples A and B. These are described by the simulation of DIS and photoproduction events.

The cross section measurement at low y relies on the measurement of y using the hadronic final state (equation 4). The determination of y is optimised by combining calorimeter energy deposits with low momentum tracks. The sum over energy clusters in the calorimeters can be strongly affected by electronic noise, in particular for low $y < 0.03$. Thus an additional noise suppression is performed which excludes isolated depositions of energy less than 400 MeV (800 MeV) in the central (forward) region of the LAr calorimeter from the analysis of both data and simulated events. This leads to a small signal loss but improves the y resolution at low y. The uncertainty of this subtraction procedure is estimated to correspond to a quarter of the suppressed noise contribution to the reconstructed hadron energy.

The calibration of the hadronic energy measurement uses the p_t balance between the scattered positron and the hadronic final state. The energy scales for the electromagnetic and hadronic sections of wheels and octants [35] of the LAr calorimeter result from a Lagrangian multiplier technique which simultaneously determines all 128 calibration constants. A systematic uncertainty of 2% on the hadronic energy scale in the LAr calorimeter is determined, based on a binwise comparison of different calibration methods. The results of the energy calibration procedure are consistent with those recently presented [12].

Figures 1c and 2c show the experimental y_h distributions over three orders of magnitude in y. In the simulation, the y_h reconstruction is found to be accurate to within a few % over a wide range of y_h and down to the small Q^2 region. The worse y resolution at low y is accounted for with an increased bin size, allowing the y range to be extended down to $y \simeq 0.004$.

The response of the SPACAL to hadronic energy flow is calibrated using longitudinal momentum conservation in the DIS events [24] to within an uncertainty of 5%. This scale uncertainty affects the final cross section data at large y through the $E - p_z$ momentum balance requirement.

4.3 Measurement at Large y

For the measurement of the longitudinal structure function it is essential to reach the maximum possible values of y (see equation 2). This requires an efficient rejection of photoproduction background events in which low energy deposits in the SPACAL can mimic the signature of a deep-inelastically scattered positron.

At Q^2 below 10 GeV^2, the range $y \leq 0.75$ is accessed by requiring a track signal in the BST. This requirement removes a sizeable fraction of the background where a cluster in the SPACAL is due to photons from $\pi^0 \to \gamma\gamma$ decays. The remaining background is due to photon conversion and showering in the passive material, possible overlap of π^0 decays with charged tracks, and misidentified charged pions. This background is subtracted bin by bin using the PHOJET event simulation. Figures 3a and 3b illustrate the range of polar angle and energy for high y events with a track in the BST. The photoproduction background can be estimated experimentally using a data sample of events which have a positron detected in the electron tagger. Figure 3c shows the energy spectrum of SPACAL clusters for those events which satisfy the DIS selection criteria, apart from the $E - p_z$ requirement. This distribution is well described by the simulation.

At Q^2 above 10 GeV^2, for $y < 0.75$, the photoproduction background is subtracted using the PHOJET event simulation. For y above 0.75, however, experimental information is used by employing the charge assignment of central tracks associated with SPACAL energy clusters. This allows the energy range to be extended down to $E'_e = 3$ GeV, corresponding to $y \leq 0.89$. For $12 \leq Q^2 \leq 35\,\mathrm{GeV}^2$ tracks reconstructed in the CJC can be linked to low energy SPACAL clusters with an efficiency of 95% (93)% in 1996 (1997). For such tracks with energies up to 15 GeV the charge is determined with an efficiency of 99.5% [24]. The sample of candidates with negative charge is taken to represent the background in the positron data sample.

The statistical subtraction procedure requires the study of any process which may cause a charge asymmetry. This asymmetry can be measured using tagged photoproduction events which fulfill the DIS event selection criteria. A small charge asymmetry $(N_+ - N_-)/(N_+ + N_-)$ is found with an average of -4.8% with a statistical accuracy of 1.9%, for $0.65 < y < 0.89$. Here $N_+(N_-)$ is the number of events with positive (negative) charge of the track associated with the SPACAL cluster. Comparing the energy distribution for a sample of negative tracks in e^+p scattering, taken in 1996/1997, with that for a sample of positive tracks in e^-p scattering, taken in 1999, a consistent asymmetry of $(-3.5 \pm 2.5)\%$ is measured. Background simulation studies and measurements of the ionisation losses in the CJC reveal that this small asymmetry is due to the antiproton interaction cross section exceeding that for proton interactions at low energies [44]. Annihilation leads to larger energy deposits in SPACAL than proton interactions which introduces an asymmetry for low energies above a given threshold. This charge asymmetry is taken into account in the measurement of the positron DIS cross section at high y. Selected control distributions [24,42] are shown in figure 4 illustrating the good understanding of this kinematic region down to scattered positron energies of $E'_e = 3$ GeV.

4.4 Results

An iterative bin wise correction procedure is adopted for the extraction of the double differential cross section σ_r. This procedure requires that the bin sizes are adapted to the resolution in the measurement of the kinematic variables. The data and the simulated events are binned in a grid in x with five bins per decade and in Q^2 with eight bins per decade, as illustrated in figure 5. At low y the resolution of the measurement degrades and the bin size is widened. For $y > 0.6$ the data are divided in bins of y, and the Q^2 division is kept. In this region the cross section may receive a large negative contribution from F_L proportional to y^2 and therefore a fine binning in y is desirable. Bins are accepted if the purity and stability are bigger than 30% with typical values being 60%. Here the purity (stability) is defined as the number of simulated events which originate from a bin and which are reconstructed in it, divided by the number of reconstructed (generated) events in that bin.

The longitudinal momentum conservation constraint, $E - p_z > 35$ GeV, limits the amount of radiative corrections to at most 5% at high y. The program HERACLES [26], which is used in the DIS event simulation, accounts for first order radiative corrections to the one photon exchange approximation. The radiative corrections are extracted using a high statistics calculation within the HERACLES Monte Carlo program, and compared with the results of the numerical program HECTOR [45], which includes higher order and hadronic corrections. The corrections are found to agree within the statistical accuracy of the radiative event simulation of 0.5%.

The results of the measurement are summarised in tables 9-12. At $y > 0.17$ the kinematics are reconstructed using the quantities Q^2_e and y_e. At $y < 0.17$, where the resolution of y_e degrades, the variables Q^2_Σ and y_Σ are used. The error calculation for the measurement is discussed below. The full error correlation matrix can be obtained from the H1 Collaboration [46].

The cross section measurement is shown in figure 6 as a function of x for different Q^2. Due to the extension of the measurement towards low y, the H1 data overlap with data of fixed target μp experiments. The H1 measurement agrees well with the fixed target data within the uncertainty of about 7 %. The cross section rises towards low x. This rise is observed to be damped at the smallest values of x, which is attributed to the longitudinal structure function, see section 5. The cross section can be well described by a QCD fit to the data as discussed in section 7.

4.5 Systematic Errors

The statistics of the data presented here exceed 10^4 events in most of the bins. The precision for this measurement is dominated by systematic uncertainties of typically 3%. These are classified into a global normalisation uncertainty, kinematically correlated errors (δ_{cor}), the statistical errors of the data (δ_{sta}) and uncorrelated errors (δ_{unc}). The uncorrelated errors contain the statistical uncertainty of the simulation and further errors due to local systematic effects.

Table 2 lists those errors which result in a possible global change of all data points. The resulting total normalisation uncertainty of the data is 1.7%. It is dominated by the error on the luminosity measurement.

source	cross section error [%]
online event selection	0.5
BDC efficiency	0.5
trigger efficiency	0.5
luminosity measurement	1.5

Table 2: *Sources and sizes of normalisation errors.*

Energy calibration and alignment uncertainties cause systematic errors which depend on the kinematics and introduce correlations between the measured data points. These errors are determined using the simulation program and verified by an analytic calculation. They are found to be symmetric to good approximation. The uncertainty of the photoproduction background simulation is estimated to be 20% . The correlated error sources are listed in table 3.

source	size of uncertainty	typical cross section error [%]
scattered positron energy scale	0.3% at $E'_e \simeq 27.5\,\mathrm{GeV}$	1
	2.7% at $E'_e = 3\,\mathrm{GeV}$	2
scattered positron angle	0.3 mrad	0.5
hadronic energy scale in LAr	2%	2
LAr noise	25% of noise	max of 5 at lowest y
photoproduction background	20% of background	3 at large y

Table 3: *Sources of correlated systematic errors and their typical effect on the cross section measurement accuracy.*

As a cross check of the positron identification, the scattered positron is also considered to be the cluster of maximum energy. When this alternative positron identification criterion is used, the cross section changes by less than 1%. This is accounted for in the systematic error. Detailed studies using different event generators with differing simulations of the hadronic final state verify the reliability of the positron identification procedure within the quoted systematic uncertainty [24].

Uncertainties due to radiative corrections, positron identification and final state simulation details are treated as uncorrelated systematic errors. The errors introduced by the track based background subtraction procedure in the high y data analysis (section 4.3) are summarised in table 4.

For each kinematic bin the resulting cross section errors are given in the cross section tables 9-12.

source	error of cross section [%]
positron identification	1
track charge determination	0.5
charge asymmetry	1
CJC-SPACAL track link efficiency	2
hadronic track requirement in CJC	1
high y trigger efficiency	1
radiative corrections	1

Table 4: *Additional sources of systematic errors and effect on the cross section for the analysis, in the range $12 < Q^2 < 25$ GeV^2, in which central jet chamber tracks are used to measure the charge of the positron candidate.*

5 Longitudinal Structure Function $F_L(x, Q^2)$

The extraction of the longitudinal structure function is based on the reduced double differential cross section (equation 2), which depends on two proton structure functions, $F_2(x, Q^2)$ and $F_L(x, Q^2)$. The contribution of F_L is enhanced with y^2, and the reduced cross section σ_r tends to $F_2 - F_L$ for $y \to 1$. In the quark-parton model, the longitudinal structure function is zero for spin 1/2 quarks [47]. In QCD, parton radiation processes [48] lead to non-zero values of F_L. Thus F_L contains information about the gluon distribution and about the strong interaction dynamics which is complementary to that obtained from the analysis of the scaling violations in $F_2(x, Q^2)$. At low Q^2 the longitudinal structure function is expected to be particularly sensitive to higher-order corrections to DGLAP QCD [49–51].

The longitudinal structure function can be extracted from the inclusive cross section only in the region of large y. An important advantage of HERA, compared to fixed target DIS lepton-nucleon experiments, is the wide range of y values covered. This allows the behaviour of F_2 at low y to be determined reliably and to be extrapolated into the region of high y. Two methods are used here to perform an extraction of the longitudinal structure function. For larger Q^2, a NLO DGLAP QCD fit is used to extrapolate F_2 into the high y region, and F_L is obtained with the "extrapolation method" introduced previously [11]. This fit uses only H1 data in the restricted kinematic range $y < 0.35$ and $Q^2 \geq 3.5$ GeV^2. Details of this and other QCD fits to H1 and fixed target data are presented in section 7. At low $Q^2 < 10$ GeV^2, the behaviour of F_2 as a function of $\ln y$ is used in a new extraction method [42], termed the "derivative method" as it is based on the cross section derivative $(\partial\sigma_r/\partial \ln y)_{Q^2}$.

5.1 Cross Section Derivative $(\partial\sigma_r/\partial \ln y)_{Q^2}$

The derivative of the reduced cross section, taken at fixed Q^2, is given by

$$\left(\frac{\partial\sigma_r}{\partial \ln y}\right)_{Q^2} = \left(\frac{\partial F_2}{\partial \ln y}\right)_{Q^2} - F_L \cdot 2y^2 \cdot \frac{2-y}{Y_+^2} - \frac{\partial F_L}{\partial \ln y} \cdot \frac{y^2}{Y_+} \qquad (10)$$

For $y \to 1$ the cross section derivative tends to the limit $(\partial F_2/\partial \ln y)_{Q^2} - 2 \cdot F_L$, neglecting the contribution from the derivative of F_L. At largest y the F_L contribution dominates the derivative of the reduced cross section σ_r. This is in contrast to the influence of F_L on σ_r which is dominated by the contribution of F_2 for all y. A further advantage of the derivative method is that it can be applied down to very low $Q^2 \simeq 1\,\mathrm{GeV}^2$ where a QCD description of $F_2(x, Q^2)$ is complicated due to higher order and possible non-perturbative corrections.

To obtain an accurate determination of $(\partial\sigma_r/\partial \ln y)_{Q^2}$ the data are rebinned in Q^2 by combining data of two adjacent Q^2 intervals. Differences $\Delta\sigma_r$ are calculated between cross section points adjacent in y at fixed Q^2. A bin-centre correction is applied to obtain the derivative at each y point, which is chosen to be the average of the two y values of the cross section measurements used to calculate the derivative. A full error analysis is performed in order to account for the correlations of errors, which partially cancel. The two adjacent data points of the derivative are anti-correlated since they use the same cross section measurement with different sign. The cross section derivatives are shown in figure 7, and the values are given in tables 13 and 14. The measured derivatives are well described by the QCD calculation (section 7.2).

For low Q^2 and $y < 0.3$ the derivative is observed to be a linear function of $\ln y$. The structure function $F_2(x, Q^2)$, at fixed Q^2, behaves like $x^{-\lambda} \propto y^{\lambda}$. At low Q^2 the exponent λ is observed to be small and the derivative is thus expected to be approximately linear in $\ln y$. This approximation is used to determine the longitudinal structure function at low Q^2. For larger Q^2 the exponent λ rises and a curvature is expected as can be seen in figure 7.

5.2 Determination of F_L

For the determination of F_L for $Q^2 < 10\,\mathrm{GeV}^2$ straight line fits are performed in $\ln y$ to the derivative $(\partial\sigma_r/\partial \ln y)_{Q^2}$ for $y \leq 0.2$. These straight lines describe the data well (figure 7) and are extrapolated to estimate the contribution of $\partial F_2/\partial \ln y$ at high y. The uncertainty on this extrapolation is included in the systematic errors of the F_L determination, taking into account the correlations of errors at low y with those at high y. The extrapolations are compared with the values obtained from the QCD analysis and very good agreement has been found. The contribution of $\partial F_L/\partial \ln y$ to the derivative (equation 10) is neglected. The uncertainty of this approximation is estimated using the derivative of F_L as calculated in QCD. It is taken as an additional uncertainty on the measurement, and amounts to about a quarter of the systematic uncertainty of F_L.

For $Q^2 > 10\,\mathrm{GeV}^2$, the NLO QCD fit of the H1 data for $y < 0.35$ is used to estimate F_2 in the high y (i.e. small x) region. In this Q^2 range, the extrapolation method is more accurate than the derivative method. The derivative method is statistically limited at maximum y since this region is accessed only with a combined SPACAL and track trigger. Figure 8 compares the fit with the measured cross section for those five Q^2 bins above 10 GeV^2 which access the high y region. The difference between the measured σ_r and the extrapolated F_2 is used to determine $F_L(x, Q^2)$ as described in [11]. Systematic errors, which are common to the lower y and the large y region, are considered in the fit as described in [52].

The F_L values obtained are presented in table 15. The uncertainties on the longitudinal structure function include several sources: the statistical errors, uncorrelated systematic errors and correlated systematic errors, resulting e.g. from the y dependent amount of subtracted photoproduction background. In addition, errors are associated with the assumptions inherent to the extraction methods. For the derivative method these errors are dominated by the uncertainty of the straight line fit, and for the extrapolation method by the variation of the smallest Q^2 of data used in the QCD fit, see section 7.2. As can be seen in table 15, these errors are smaller than the experimental systematic errors. In the region of overlap, for Q^2 between 4 GeV^2 and 15 GeV^2, the derivative method and the extrapolation method give consistent results. Further details of this analysis are described in [42].

The values for $F_L(x, Q^2)$, given in table 15, are consistent with the previous determination of F_L by the H1 collaboration [11], but they are more precise and obtained in a wider kinematic range. The H1 data extend the knowledge of the longitudinal structure function beyond that obtained from fixed target lepton-proton scattering experiments into the region of much lower x, see figure 9. The increase of $F_L(x, Q^2)$ towards low x is consistent with the NLO QCD calculation (section 7.2), reflecting the rise of the gluon momentum distribution towards low x. The values of $F_L(x, Q^2)$ are thus severely constrained unless there are deviations from the assumed extrapolation of F_2 into the region of large y corresponding to the smallest x. A measurement of the x dependence of $F_L(x, Q^2)$ can be performed independently of assumptions about the behaviour of F_2 with a variation of the proton beam energy at HERA [53].

6 Structure Function F_2 and Derivative $(\partial F_2/\partial \ln Q^2)_x$

The proton structure function $F_2(x, Q^2)$ is obtained from the measured reduced cross section using equation 2 rewritten as

$$F_2 = \sigma_r \cdot \left(1 - \frac{y^2}{Y_+} \cdot \frac{R}{1+R}\right)^{-1}. \tag{11}$$

The ratio $R = F_L/(F_2 - F_L)$ is determined using the standard DGLAP QCD fit to the H1 data (section 7.2), calculating F_L to order α_s^2. In order to reduce the dependence of the measurement on F_L, the F_2 extraction is limited to the range $y \leq 0.6$. The results for $F_2(x, Q^2)$ and the calculated values of $F_L(x, Q^2)$ are given in tables 9-12. This measurement is consistent with, and improves upon, the previous results [8], which were obtained with a different backward apparatus.

In figure 10 the measurement of the structure function $F_2(x, Q^2)$ at low x is shown as a function of Q^2. The data are well described by the NLO QCD fit, as is discussed in detail in section 7.2. The $\ln Q^2$ dependence of F_2 is observed to be non-linear. It can be well described by a quadratic expression

$$P_2(x, Q^2) = a(x) + b(x) \ln Q^2 + c(x)(\ln Q^2)^2, \tag{12}$$

which nearly coincides with the QCD fit in the kinematic range of this measurement.

The DGLAP evolution equations are governed by the derivative $(\partial F_2/\partial \ln Q^2)_x$ taken at fixed x. Measurement of this derivative has long been recognised as a powerful constraint on xg and α_s [54]. In the low x DIS region its behaviour is a direct reflection of the behaviour of the gluon density [55]. This quantity has also been studied in [56] in view of possible non-linear gluon interaction effects [7]. A study of the derivative $(\partial F_2/\partial \ln Q^2)_x$ at low x was presented previously by the ZEUS Collaboration [57] where $F_2(x, Q^2)$ was assumed to depend linearly on $\ln Q^2$. This approximation is inconsistent with the data presented here, as can be deduced from figure 10. Fits with $c(x) = 0$ yield χ^2/dof values about twice as large as the quadratic fit, Eq.12.

Using the procedure adopted for the derivatives $(\partial \sigma_r/\partial \ln y)_{Q^2}$ (section 5.1) the local derivatives $(\partial F_2/\partial \ln Q^2)_x$ are measured. The results are shown in figure 11 for different x as a function of Q^2, and the values are quoted in tables 16,17 and 18. For each bin of x these derivatives can be described by the function $b(x) + 2 \cdot c(x) \ln Q^2$ (solid lines). Small deviations of $(\partial F_2/\partial \ln Q^2)_x$ from the linearity in $\ln Q^2$ occur in NLO QCD (dashed lines). Using the linear expression the derivatives are calculated at fixed $Q^2 \geq 3\,\mathrm{GeV}^2$ and are shown as functions of x in figure 12. The derivatives show a continuous rise towards low x for fixed Q^2 which is well described by the NLO DGLAP QCD to the H1 data (section 7.2). The shape of $(\partial F_2/\partial \ln Q^2)_x$ reflects the behaviour of the gluon distribution in the associated kinematic range.

7 QCD Analysis

In this section the predictions of the DGLAP evolution equations in NLO are confronted with the reduced differential cross section measurement. By comparison to the cross section data, the strong coupling constant α_s, and the shape and normalisation of the gluon and quark distributions are determined. This is done using a χ^2 minimisation procedure (fit) and a suitable choice of parameterisations for the input parton distributions at an initial scale Q_0^2.

Traditionally, this kind of analysis makes use of both lepton-proton and lepton-deuteron data [58–62] in order to separate the non-singlet and singlet evolution, and also to determine the parton distributions of up and down quarks simultaneously. The present analysis introduces a new parameterisation of quark distributions which permits lepton-proton data to be analysed alone. Thus the use of deuteron scattering data, which involves bound state corrections and their uncertainties, is avoided.

Two complete analyses are performed, one with H1 data only to determine the gluon distribution $xg(x, Q^2)$ at low x, and a second one in which the H1 data are combined with data from the BCDMS experiment in order to simultaneously determine the strong coupling constant $\alpha_s(M_Z^2)$ and the gluon distribution.

The most difficult aspect of these fits is an adequate treatment of systematic errors, which lead to strong correlations among the data points. The present analysis uses a sophisticated treatment of systematic error correlations allowing their true effect on the extracted quantities to be estimated by the fit [52]. This procedure is used to identify data regions which are strongly affected by correlated systematic errors. The present analysis is therefore based on a minimum number of data sets in regions where their systematic errors are well understood. Uncertainties due to physics and analysis assumptions are estimated by a systematic exploration of the parameter space.

The Q^2 evolution of parton distributions is the result of processes of radiation from gluons which dominate the scaling violations at small $x \leq 0.1$, and from quarks which dominate at large x. The present H1 data allow the gluon contribution to be well determined for fixed α_s. The strong correlation between the gluon distribution with α_s can be much reduced by using DIS data at large x and low Q^2, in addition to the H1 data. Thus, the analysis is extended to include the precise μp data at large x from the BCDMS collaboration. This allows the gluon distribution and α_s to be determined simultaneously.

7.1 Analysis Procedure

In the quark-parton model, the proton structure function $F_2(x, Q^2)$ is given by a sum of quark and anti-quark momentum distribution functions

$$F_2(x, Q^2) = x \sum_q Q_q^2 \cdot [q(x, Q^2) + \overline{q}(x, Q^2)], \tag{13}$$

where Q_q represents the electric charges of quarks. In the present analysis, the sum extends over up, down and strange ($u,\ d,\ s$) quarks. The charm and beauty contributions are added using NLO QCD calculations [63] using $m_c = 1.4\,\mathrm{GeV}$ and $m_b = 4.5\,\mathrm{GeV}$. At low x about 20-30% of the inclusive cross section is due to charm production, dominated by the photon-gluon fusion process.

The present QCD analysis, described in detail in [41], uses a flavour decomposition of $F_2(x, Q^2)$ into two independent combinations of parton distribution functions $V(x, Q^2)$ and $A(x, Q^2)$, according to

$$F_2 = \frac{1}{3} xV + \frac{11}{9} xA. \tag{14}$$

The x dependences of xg, V and A are parameterised at an initial scale Q_0^2, and a χ^2 minimisation determines these distributions and α_s. The function V is defined by the valence-quark distributions, i.e.

$$V = \frac{9}{4} u_v - \frac{3}{2} d_v. \tag{15}$$

It is thus constrained by the relation

$$\int_0^1 V dx = 3, \tag{16}$$

which is used in the fit procedure together with the momentum-sum rule. The function A contains the sea-quark distribution and a small valence-quark correction. It is given as

$$A = \overline{u} - \frac{1}{4}(u_v - 2d_v), \tag{17}$$

and determines the low x behaviour of $F_2(x, Q^2)$.

These equations hold for a strange contribution $s + \overline{s} = (\overline{u} + \overline{d})/2$ and flavour symmetry of the sea, $u_{sea} = \overline{u} = d_{sea} = \overline{d}$. This ansatz is generalised in Appendix A.1 to account for the observed small deviations of the strange [64] and antiquark [65] distributions from the conventional assumptions about the sea. In the analysis target-mass corrections are applied using the integral relations for F_2 and F_L as given in [66].

The analysis is performed in the $\overline{MS}$ renormalisation scheme using the DGLAP evolution equations [4] in NLO [67]. Thus the formulae for F_2 given here are modified by replacing the sums over parton distributions by sums over integrals of products of coefficient functions times parton distributions.

The strong coupling constant is defined by the solution of the renormalisation group equation to order α_s^3,

$$\frac{da_s}{d\ln\mu_r^2} = -\beta_0 a_s^2 - \beta_1 a_s^3, \tag{18}$$

where $a_s = \alpha_s/4\pi$, μ_r is the renormalisation scale, and the β functions are defined in [67]. The longitudinal structure function is calculated to order α_s^2. The analysis uses an x space program developed inside the H1 collaboration [68, 69]. This program has been checked in detail against different evolution codes [59, 70, 71], and very good agreement is found.

In the fit procedure, a χ^2 function is minimised which is defined in Appendix A.2. This definition takes into account correlations of data points caused by systematic uncertainties. It is desirable that the fit results depend neither significantly on the functional form of the parameterisations which are used for the input distributions, nor on the input scale Q_0^2 at which these are defined. Thus, for each fit described below, a grid of nearly 10^3 initial fit conditions is considered, with about tenfold variations of each of the parameters Q_0^2, Q_{min}^2 and α_s. Here Q_{min}^2 denotes the smallest Q^2 value of data included in the fit.

The quality of the fits is studied in a statistical evaluation of the parameter space for all data sets and parton distribution parameterisations considered. As described in Appendix A.3, this leads to a best choice of

$$xq(x) = a_q x^{b_q}(1-x)^{c_q}[1 + d_q\sqrt{x} + e_q x], \tag{19}$$

for the parameterisations of the functions V, A and xg. The standard value of Q_0^2 is 4 GeV^2, but it can be varied over a reasonable range without significantly influencing the result.

7.2 Fit to H1 Data and Determination of the Gluon Distribution

The measurements of the reduced differential cross section presented here are combined with recent data of the H1 collaboration [12] from the same data taking period, which cover the large x range at high $Q^2 \geq 150\,\mathrm{GeV}^2$. A cut $Q^2 \leq 3000$ GeV^2 is applied to eliminate the region where electroweak interference effects are important, which involve the structure function xF_3. Since the H1 data have still limited precision at large x, the parameter d_g in the expression for the gluon distribution (equation 19) is superfluous, see Appendix A.3. For the fits to the H1 data alone it is therefore set to $d_g = 0$.

The standard fit assumes a fixed $\alpha_s(M_Z^2) = 0.115$ and uses all H1 data for $Q^2 \geq 3.5$ GeV^2 . In this range derivatives of F_2 with respect to $\ln Q^2$ are measured and found to be described by the DGLAP evolution equations (see section 6). The momentum fraction carried by the gluons is $0.43 \pm 0.02\ (exp)$ at the input scale $Q_0^2 = 4$ GeV^2 where the error is due to the measurement uncertainties. The variation of the gluon momentum fraction with Q^2 is shown in figure 13. The result agrees with previous determinations at $Q^2 = 7$ GeV^2 [58, 72]. The stability of this result has been checked by adding μp and also μd data of the BCDMS collaboration. As is shown in figure 13, no significant change is observed. The fit is also repeated without using the constraint given by the momentum sum rule. This fit determines the integral $\int_0^1 x(\Sigma + g)dx$ to be $1.016 \pm 0.017(exp)$, where Σ is the singlet parton distribution function, see Appendix A.3. This value is found to be nearly independent of the minimum Q^2 value of the data included in the analysis.

The structure function $F_2(x, Q^2)$ is extracted from the reduced cross section data using the prediction of the fit for the longitudinal structure function $F_L(x, Q^2)$. The result is shown in figures 14 and 15. The data are compared to published μp data of the fixed target muon-proton scattering experiments BCDMS and NMC. The solid lines give the result of the QCD fit with $Q^2_{min} = 3.5$ GeV^2 to the H1 data. This fit also describes the fixed target data in the non-overlapping regions rather well, except for the data points at $x = 0.65$ where the fit curve is below the BCDMS data. The H1 data at this value of x [12] have a correlated systematic uncertainty of 12%, due to the energy scale error for the scattered positron, which accommodates the observed difference.

The x range is restricted at small x by the choice of Q^2_{min}. An extension of the analysis to low values of Q^2 and x is of interest to study possible deviations from NLO DGLAP evolution. The dependence of the fit result on the chosen Q^2_{min} is studied systematically. Figure 16 shows the H1 F_2 data for $x \leq 8 \cdot 10^{-4}$ together with the fit curves for different values of Q^2_{min}. The fit with $Q^2_{min} = 1.5$ GeV^2 describes all the data very well. If Q^2_{min} is raised, the fit curves extrapolated below $Q^2 = Q^2_{min}$ tend to undershoot the data excluded from the fit. The gluon distributions at $Q^2 = 5$ GeV^2 obtained from these fits are shown in figure 17 in the low x range where the gluon distribution is constrained[1]. They are consistent within the estimated uncertainty in the overlapping regions. Extension of this study into

[1]The measurement of the slope $(\partial F_2/\partial \ln Q^2)_x$ requires at least two data points with different Q^2 above Q^2_{min} for fixed x. Thus the minimum value x_{min} at which this slope can be measured depends on Q^2_{min}. It has been shown in [55] that the derivative $(\partial F_2/\partial \ln Q^2)_x$ determines the gluon distribution at a value of approximately $2x$. The gluon distributions in figure 17 are therefore shown only down to $x \simeq 2x_{min}$.

the region of $Q^2 \simeq 1\,\text{GeV}^2$ is of interest. It requires precision data in a large range of x. For such Q^2 values the gluon distribution $xg(x,Q^2)$, in twist 2 NLO QCD, is observed to approximately vanish at low x acquiring a valence-like shape.

The fit to the H1 data determines $\alpha_s(M_Z^2)$ to be 0.115 with an experimental error of ± 0.005 and an optimum χ^2 of 180 for 224 degrees of freedom. This is the first measurement of α_s with HERA inclusive cross section data alone. The result for the gluon distribution obtained from the H1 measurements is shown in figure 18. The innermost error band is due to the experimental measurement uncertainty, which for $3 \cdot 10^{-4} \leq x \leq 0.1$ is about 5% and decreases to about 3% at $Q^2 = 20\,\text{GeV}^2$. The middle error band illustrates the effect of an α_s uncertainty of ± 0.0017, which is derived in the fit to the combined H1 and BCDMS data (see below). The outer error band includes in addition the uncertainty of the QCD model as described subsequently. For values of $x > 0.1$ this analysis is not able to reliably determine the shape of the gluon distribution because in this range the scaling violations are dominated by quark radiation rather than gluon radiation. Yet, the integrated momentum fraction carried by gluons at large x is constrained by the momentum sum rule as discussed above. The fit determines this contribution to be $\int_{0.1}^{1} xg(x,Q^2)dx = 0.13 \pm 0.04\ (exp)$ for $Q^2 = 4\,\text{GeV}^2$.

The result for the gluon distribution depends on the theoretical framework since xg is not an observable. For example, if the massive quark description for charm and beauty production is replaced by the massless treatment of heavy quarks, the gluon distribution changes as illustrated in figure 19. The gluon distribution in the massless fit is about 15% lower at small x compared to the standard result. A consistent cross check of this massless fit result is obtained with a Mellin n space program [73].

The analysis of the longitudinal structure function F_L (section 5.2) uses a QCD fit to the reduced cross section for $y \leq 0.35$. This fit follows exactly the same procedure as that described above. It results in a χ^2 of 151 for 180 degrees of freedom and agrees very well with the full fit. In particular, the gluon distribution obtained in this fit is nearly indistinguishable from xg obtained in the standard fit covering the full y range which is sensitive to F_L. Thus, $xg(x,Q^2)$ appears to be determined by the scaling violations of $F_2(x,Q^2)$.

7.3 Simultaneous Determination of $\alpha_s(M_Z^2)$ and the Gluon Distribution

The precision of the large x, high Q^2 H1 data [12] is not sufficient to enable a competitive determination of $\alpha_s(M_Z^2)$ and of the gluon distribution simultaneously from the H1 data alone. The most precise measurement of the DIS inclusive cross section at large x was obtained by the BCDMS μp scattering experiment [13] (figure 15). These data are therefore combined with the H1 measurements.

In a first step, a fit is performed to the complete data sets. The correlated systematic errors of the data are fitted, together with the other parameters. Regions of data are identified in which the fit causes large systematic shifts of the data points. For the BCDMS data in the range $y_{BCDMS} = y_\mu < 0.3$ the data points are shifted by more than the quoted systematic error. The low y region in this experiment is particularly strongly affected by the energy scale uncertainty of the scattered muon, which leads to correlated systematic errors $\propto 1/y$. These become large at low y for each of the four data sets at different muon energy. Note that the low y data of BCDMS differ from measurements of the ep scattering cross section at SLAC [74,75] in the region of overlap. In this region the BCDMS data accuracy is dominated by systematic errors while the SLAC measurement is statistically limited. This also suggests the presence of large systematic effects in the low y region of the BCDMS data which were studied previously [76]. Therefore in all analyses only BCDMS data with $y_\mu > 0.3$ are used.

The result of the QCD fit to the combined H1 and BCDMS data sets, leaving α_s as a free fit parameter, is shown in figures 14 and 15 as dashed curve. It describes the data very well with a χ^2/dof of 394/451. The fit to the H1 and BCDMS data is nearly indistinguishable from the fit to the H1 data alone, except for the two highest x bins. The parameterisations used in the fit to the H1 and BCDMS data are given in equation 19, and the parameters are summarised in table 5. The choice of these particular shapes results from a detailed analysis of the behaviour of the χ^2 function, similar to the fit to the H1 data which is described in Appendix A.3.

	a	b	c	d	e
gluon	1.10	-0.247	17.5	-4.83	68.2
V	86.3	1.47	4.48	-2.12	1.60
A	0.229	-0.130	19.7	-3.82	29.8

Table 5: *Parameters of the input distributions $xq(x) = a_q x^{b_q}(1-x)^{c_q}[1 + d_q\sqrt{x} + e_q x]$ for $xg(x, Q^2)$, $V(x, Q^2)$ and $A(x, Q^2)$ at the initial scale $Q_0^2 = 4$ GeV^2 using H1 and BCDMS data for $Q^2 \geq 3.5$ GeV^2 and $y_\mu > 0.3$. A fit with $d_g = e_g = 0$ yields $c_g = 6.5$, not far from the dimensional counting rule expectation [77], yet with a worsened χ^2.*

The α_s value obtained in the NLO analysis of the H1 and BCDMS proton data is

$$\alpha_s(M_Z^2) = 0.1150 \ \pm \ 0.0017 \ (exp) \ ^{+\ 0.0009}_{-\ 0.0005} \ (model). \tag{20}$$

In this combined fit both data sets consistently favour a value of $\alpha_s(M_Z^2) \simeq 0.115$ with comparable accuracy. The first error represents the experimental uncertainty of the data sets. The second error includes all uncertainties associated with the construction of the QCD model for the measured cross section. These are summarised in table 6. The strong coupling constant is defined here by the solution of the renormalisation group equation to order α_s^3. In the double logarithmic approximation the value for $\alpha_s(M_Z^2)$ is calculated to be lower by 0.0003.

The value obtained for $\alpha_s(M_Z^2)$ is nearly independent of Q_0^2 and of the chosen parameterisation for the large set of input distributions considered in Appendix A.3. Residual effects are included in the estimation of the systematic error on α_s. The dependence of α_s on Q^2_{min} is shown in figure 20. No systematic trend is observed. Note that the BCDMS data are limited to $Q^2 \geq 7.5$ GeV^2, such that a choice of Q^2_{min} below this value affects the low x H1 data only.

analysis uncertainty	+$\delta\ \alpha_s$	-$\delta\ \alpha_s$
$Q^2_{min} = 2$ GeV^2		0.00002
$Q^2_{min} = 5$ GeV^2	0.00016	
parameterisations	0.00011	
$Q^2_0 = 2.5$ GeV^2	0.00023	
$Q^2_0 = 6$ GeV^2		0.00018
$y_e <$ 0.35	0.00013	
$x <$ 0.6	0.00033	
$y_\mu >$ 0.4	0.00025	
$x > 5 \cdot 10^{-4}$	0.00051	
uncertainty of $\overline{u} - \overline{d}$	0.00005	0.00005
strange quark contribution $\epsilon = 0$	0.00010	
$m_c + 0.1$ GeV	0.00047	
$m_c - 0.1$ GeV		0.00044
$m_b + 0.2$ GeV	0.00007	
$m_b - 0.2$ GeV		0.00007
total uncertainty	0.00088	0.00048

Table 6: *Contributions to the error of $\alpha_s(M_Z^2)$ in the analysis of H1 ep and BCDMS μp data which are due to the selection of data and to the fit assumptions.*

The combination of low x data with high x data constrains the gluon distribution and α_s. A correlation is observed (figure 21) between α_s and the parameter b_g, which governs the shape of the gluon distribution at low x (equation 19). In a fit to the BCDMS data alone, for $y_\mu > 0.3$ and using $xg = ax^b(1-x)^c$, a value of $\alpha_s(M_Z^2) = 0.111 \pm 0.003\ (exp)$ is found [2], and b_g is positive. A positive value of b_g implies that $xg(x, Q_0^2)$ falls as x decreases. An early α_s analysis [60], in the absence of detailed information about the low x behaviour of xg, assumed $b_g = 0$. A positive or zero value of b_g, for $Q_0^2 \geq 4$ GeV^2, is found to be incompatible with the data which is consistent with previous studies [75]. The fit to the BCDMS data, when complemented with low x H1 data, leads to a negative b_g parameter, and therefore a larger value of $\alpha_s(M_Z^2)$ is obtained with the BCDMS data than hitherto. The results of these fits to the H1 and BCDMS data are shown in figure 22a. In the combined fit both data sets give a consistent and comparable contribution to the error on α_s. This is illustrated in figure 22b.

A rather large theoretical uncertainty of the NLO analysis results from the choices of the renormalisation scale $\mu_r^2 = m_r \cdot Q^2$ (equation 18), and of the factorisation scale $\mu_f^2 = m_f \cdot Q^2$ which leads to scale dependent parton distributions. In the $\overline{MS}$ scheme both scales are set equal to Q^2, i.e. $m_r = m_f = 1$. In the absence of a clear theoretical prescription, the effect of both scales on α_s is estimated by varying the scale factors m_r and m_f between 0.25 and 4. The results are summarized in table 7. In agreement with previous studies [62] it is found that

[2] The requirement $y_\mu > 0.3$ causes $\alpha_s(M_Z^2)$ to increase by about 0.004 in the fit to the BCDMS data only, and by about 0.002 in the fit to the H1 and BCDMS data combined.

	$m_r = 0.25$	$m_r = 1$	$m_r = 4$
$m_f = 0.25$	-0.0038	-0.0001	$+0.0043$
$m_f = 1$	-0.0055	$--$	$+0.0047$
$m_f = 4$	$--$	$+0.0005$	$+0.0063$

Table 7: *Dependence of $\alpha_s(M_Z^2)$ on the renormalisation and factorisation scales m_f and m_r, respectively, expressed as the difference of $\alpha_s(M_Z^2)$ obtained for scales different from one and the central value of $\alpha_s(M_Z^2)$=0.1150. The combination $m_f = 4$ and $m_r = 0.25$ is abandoned since the splitting function term $\propto \ln(m_r/m_f)^2$ becomes negative at low Q^2 which causes a huge increase of χ^2.*

the renormalisation scale causes a much larger uncertainty on $\alpha_s(M_Z^2)$ than the factorisation scale. Depending on which set of m_r and m_f is chosen, the obtained χ^2 differs by several units. This suggests that the assumed variation of the scales is too large. These scales, however, are not considered to represent physics quantities which may be determined in the minimisation procedure. The estimated overall uncertainty of about 0.005 on $\alpha_s(M_Z^2)$ is much larger than the experimental error. It is expected to be significantly reduced when next-to-NLO calculations become available [71, 78]. Recently an α_s analysis of moments of structure functions, measured in charged lepton-nucleon scattering, was presented extending to NNLO QCD [79].

The stability of the fit results is checked further with respect to possible changes in the analysis procedure:

- The value of $\alpha_s(M_Z^2)$ increases by 0.0005 if the correlation due to systematic errors is neglected, i.e. if the correlated systematic error parameters are not part of the minimisation (see Appendix A.2).
- In the present analysis, the relative normalisations of the data sets are left free. The change imposed by the fit to the BCDMS data is about -1.5% within a total normalisation uncertainty of 3%. The H1 data are moved by about 1% within the experimental error of 1.7%. Thus the selected H1 and BCDMS data are compatible with each other. If the fit is repeated with all normalisations fixed then χ^2 increases by 26, and $\alpha_s(M_Z^2)$ increases by 0.0005.
- If the BCDMS data is replaced by data of the NMC collaboration [80], imposing the low Q^2 limit of the BCDMS data, a consistent value of $\alpha_s(M_Z^2) = 0.116 \pm 0.003\ (exp)$ is obtained.
- If the heavy flavour treatment is changed and a massless, four flavour fit performed, $\alpha_s(M_Z^2)$ is enlarged by +0.0003.
- The addition of the BCDMS deuteron target data, with $y_\mu > 0.3$, to the H1 and BCDMS proton data yields $\alpha_s(M_Z^2)$= 0.1158 ± 0.0016 (exp), i.e. $\alpha_s(M_Z^2)$ increases by 0.0008. In this analysis nuclear corrections [81] are applied, and the conventional flavour decomposition into valence and sea quarks is used.

The gluon distribution from the fit to the H1 and the BCDMS proton cross section data is shown in figure 23 for $Q^2 = 5\,\mathrm{GeV}^2$. The inner error band represents the experimental uncertainty of the determination of xg for α_s fixed. This fit, however, simultaneously determines $xg(x, Q^2)$ and α_s , which leads to a small increase of the experimental error of xg as is illustrated by the middle error band. The full error band includes in addition the uncertainties connected with the fit ansatz, as listed in table 6 for the determination of $\alpha_s(M_Z^2)$. For the low x behaviour of $xg(x, Q^2)$ these are dominated by the choice of Q^2_{min}, as is discussed in section 7.2. The gluon distribution from the combined fit is shown also for two higher Q^2 values, 20 and 200 GeV^2 . The DGLAP evolution leads to a gluon distribution which rises dramatically at small x with increasing Q^2 (figure 23). The inner solid line illustrates the behaviour of $xg(x, Q^2)$, as determined with the H1 data alone, which is seen to be in very good agreement. The fits with deuteron data or NMC data lead to very similar gluon distributions. This analysis determines xg from the scaling violations of F_2 . It is more accurate but consistent with determinations of the gluon distribution by the H1 experiment in charm [82] and deep-inelastic dijet [83] production.

8 Summary

A new measurement of the deep-inelastic positron-proton scattering cross section is presented for squared four-momentum transfers $1.5 \leq Q^2 \leq 150\ \mathrm{GeV}^2$ and Bjorken-x values $3 \cdot 10^{-5} \leq x \leq 0.2$ which is more precise than previous measurements in this kinematic range. The statistical accuracy of the present inclusive cross section measurement is better than 1%, for a large part of the kinematic region. The systematic uncertainty has decreased to about 3%, apart from the edges of the covered range. This is due to improved detectors in the backward region used for the identification and measurement of the scattered positrons at low Q^2. These are an electromagnetic calorimeter (SPACAL) with very good spatial and energy resolutions, a drift chamber (BDC) and a silicon tracker (BST).

The kinematic range is extended down to $y = 0.004$ such that the present data overlap kinematically with the measurements of muon-proton scattering experiments. This is achieved with higher statistics, improved event vertex reconstruction and calibration of the forward parts of the calorimeter. The present data agree with the μp data in the region of overlap within the accuracy of about 7%. The kinematic range is extended also up to $y = 0.82$ using track reconstruction in front of the SPACAL in an extended angular range.

The cross section measurement is used to determine derivatives with respect to $\ln y$ and to $\ln Q^2$ as functions of x and Q^2. The partial derivative $(\partial F_2/\partial \ln Q^2)_x$ is measured in the full x, Q^2 range of this measurement. When considered as a function of x at fixed Q^2, for $3 \leq Q^2 \leq 40$ GeV^2 , it is observed to rise continuously towards low x in agreement with QCD.

The partial derivative of the reduced cross section $(\partial \sigma_r/\partial \ln y)_{Q^2}$ is used to extract F_L at low $Q^2 < 10\,\mathrm{GeV}^2$. This is complemented by a determination of F_L at $Q^2 > 10\,\mathrm{GeV}^2$ using the difference between the measured reduced cross section, σ_r, and F_2 calculated from an extrapolation of a NLO QCD fit to low y data. Thus the longitudinal structure function F_L at low x is determined more precisely than hitherto, and in a larger Q^2 range.

A detailed, systematic analysis is presented of the structure function data using the DGLAP evolution equations in NLO. The salient features of this analysis are a new formalism for charged lepton-proton scattering and a comprehensive study of the influence of model parameters and parton distribution parameterisations on the results. These are obtained from a minimum number of data sets with special emphasis on the treatment of correlated systematic errors.

The scaling violations of F_2 , the behaviour of the derivatives and of the longitudinal structure function at low x are found to agree with DGLAP QCD. The present precise low x data, when combined with high Q^2 data of H1 from the same running period, determine the shape of the gluon distribution at small x. The gluon distribution $xg(x, Q^2)$ is determined at $Q^2 = 20\,\mathrm{GeV}^2$ to an experimental accuracy of about 3% in the kinematic range $3 \cdot 10^{-4} \leq x \leq 0.1$.

A simultaneous determination of the gluon distribution and of α_s is obtained by combining the low x data of H1 with μp scattering data of the BCDMS collaboration at large x. A value of the coupling constant $\alpha_s(M_Z^2) = 0.1150 \pm 0.0017(exp)^{+\,0.0009}_{-\,0.0005}(model)$ is obtained. The value of α_s changes by about 0.005, much more than the experimental error, if the renormalisation scale is allowed to vary by a factor of four, and to a lesser extent if the factorisation scale is changed by the same amount. This uncertainty is expected to be reduced significantly in next-to-NLO perturbation theory.

Acknowledgements We are very grateful to the HERA machine group whose outstanding efforts made this experiment possible. We acknowledge the support of the DESY technical staff. We appreciate the substantial effort of the engineers and technicians who constructed and maintain the detector. We thank the funding agencies for financial support of this experiment. We wish to thank the DESY directorate for the support and hospitality extended to the non-DESY members of the collaboration. We thank J. Blümlein, M. Botje, W. van Neerven, R. Roberts, and W.-K. Tung for interesting discussions on the QCD interpretation of this data. We are particularly grateful to A. Vogt for his cooperative effort in the analysis of higher-order effects on α_s and to R. Engel for help in the photoproduction background simulation.

A Details of the QCD Analysis

A.1 Flavour Decomposition of F_2

The structure function F_2 can be written as

$$F_2 = \frac{4}{9} \cdot xU + \frac{1}{9} \cdot xD, \tag{21}$$

with $U = u + \overline{u}$ and $D = d + \overline{d} + s + \overline{s}$ (equation 13). A modified projection yields

$$F_2 = \frac{2}{9} \cdot x\Sigma + \frac{1}{3} \cdot x\Delta. \tag{22}$$

The sum $\Sigma = U + D$ defines a singlet combination of quark distributions which has a Q^2 evolution coupled to the gluon momentum distribution xg. The difference $\Delta = (2U - D)/3$ defines a non-singlet distribution which evolves independently of xg. Thus F_2 is defined by two independent quark distribution functions.

In this analysis two specific functions $V(x, Q^2)$ and $A(x, Q^2)$ are chosen which are related to U and D according to

$$U = \frac{2}{3}V + 2A \tag{23}$$

and

$$D = \frac{1}{3}V + 3A. \tag{24}$$

The inverse relations defining V and A are

$$V = \frac{3}{4}(3U - 2D) = \frac{9}{4}u_v - \frac{3}{2}d_v + \frac{9}{2}\overline{u} - 3(\overline{d} + \overline{s}) \tag{25}$$

and

$$A = \frac{1}{4}(2D - U) = \overline{d} + \overline{s} - \frac{1}{2}\overline{u} - \frac{1}{4}u_v + \frac{1}{2}d_v, \tag{26}$$

which for the conventional assumption $\overline{u} = \overline{d} = 2\overline{s}$ lead to the relations presented in the introduction of the QCD analysis, see section 7.1. In this approximation the V distribution vanishes for small $x < 0.01$. The behaviour for large x is defined by u_v. For small x the function A is given by the sea distribution $A \simeq \overline{u}$.

Recent measurements of Drell-Yan muon pair production at the Tevatron [65] have established a difference between the $\overline{u}$ and $\overline{d}$ distributions. Charged current neutrino-nucleon experiments determined the relative amount of strange quarks in the nucleon sea to be

$$s + \overline{s} = (\frac{1}{2} + \epsilon) \cdot (\overline{u} + \overline{d}), \tag{27}$$

with a recent value of $\epsilon = -0.08$ [84]. These results lead to modifications of the simple assumptions on the sea[3]. They have been accounted for by modifying equation 24 according to

$$D = \frac{1}{3}V + kA, \tag{28}$$

which, using equation 23, results in

$$V = \frac{3}{2} \cdot \frac{1}{k-1}(kU - 2D) \tag{29}$$

and $\Sigma = V + A \cdot (2 + k)$. Choosing $k = 3 + 2\epsilon$ can be shown to remove the strange contribution to the function V yielding

$$V = \frac{3}{4} \cdot \frac{1}{1+\epsilon}[(3+2\epsilon)u_v - 2d_v + (5+2\epsilon)(\overline{u} - \overline{d})], \tag{30}$$

which coincides with equation 15 for $\epsilon = 0$ and $\overline{u} = \overline{d}$. Because the integral $\delta = \int(\overline{u} - \overline{d})dx$ is finite [4], this choice of k allows the counting rule constraint (equation 16) to be maintained as

$$\int_0^1 V dx = 3 + \delta \cdot \frac{3}{4} \cdot \frac{5+2\epsilon}{1+\epsilon} = v(\epsilon, \delta). \tag{31}$$

If this constraint is released in a fit to the H1 data, a value of $\int V dx = 2.24 \pm 0.13(exp)$ is obtained instead of about 2.5 following from equation 31. The modified expression for the A function in terms of quark distributions becomes

$$A = \frac{1}{4} \cdot \frac{1}{1+\epsilon}[4\overline{u} - (u_v - 2d_v) - 5(\overline{u} - \overline{d}) + 2\epsilon(\overline{u} + \overline{d})]. \tag{32}$$

For the naive assumptions $\epsilon = 0$ and $\overline{u} = \overline{d}$ this yields the approximate relation 17 and $A \simeq \overline{u}$ at low $x < 0.1$. In the analysis these generalised expressions are used for V, its integral and A.

A.2 Definition of Minimisation Procedure

The χ^2 is computed as

$$\begin{aligned} \chi^2 &= \sum_e \sum_d \frac{[\sigma_{r\,d,e} - \sigma_{r\,d,e}^{fit} \times (1 - \nu_e \delta_e - \sum_k s_e^k \cdot \delta_{d,e}^k)]^2}{[\sigma_{r\,d,e}]^2(\delta_{sta}^2 + \delta_{unc}^2)} \\ &+ \sum_e \nu_e^2 + \sum_e \sum_k (s_e^k)^2. \end{aligned} \tag{33}$$

[3] The evolution of $s + \overline{s}$ in DGLAP QCD is found to yield a linear dependence of ϵ on $\ln Q^2$ which is used to extrapolate the NuTeV result [84], obtained at $16\,\mathrm{GeV}^2$, to $Q^2 = Q_0^2$.

[4] The most accurate measurement of $\int_0^1(\overline{u} - \overline{d})dx$ has been performed by the E866/NuSea Collaboration [65] which obtained a value of -0.118 ± 0.011 at $\langle Q^2 \rangle = 54\,\mathrm{GeV}^2$.

The first two sums run over the data (index d) of the various experiments (index e). δ_e is the relative overall normalisation uncertainty and ν_e its change observed in the fit. $\delta^k_{d,e}$ denotes the relative correlated systematic error for a given error source k and s^k_e its observed change in the fit. δ_{sta} and δ_{unc} are the relative statistical and uncorrelated systematic errors, respectively, where the indices d and e have been omitted for clarity. For this measurement the relative correlated systematic errors $\delta^k_{d,e}$ are given in [46] and δ_{sta} and δ_{unc} are quoted in tables 9-12.

A.3 Parameterisations

As explained above, three parton distributions (xg, V and A) are necessary to describe the proton structure function $F_2(x, Q^2)$ and its Q^2 evolution. The following general type of parameterisation is used

$$xq = a_q x^{b_q} (1-x)^{c_q} [1 + d_q \sqrt{x} + e_q x + f_q x^2] \tag{34}$$

for $q = g,\ V$ and A. An attempt is made to describe these functions with the least number of parameters in the brackets of equation 34. All distributions are first calculated using recent parameterisations of parton distributions, by GRV98 [85], MRS99 [75] and CTEQ5 [86]. The resulting functions are fitted using the expressions of equation 34 in order to obtain initial information about how the new linear combinations of parton distributions V and A are possibly parameterised best. All global analysis distributions require the presence of d_V and e_V but allow f_V to be set to zero. This defines the parameterisation of V which mainly is a combination of valence quark distributions, see equation 30. For xg and A, however, different parameter combinations are tested in a systematic way using fits to data.

The choice of a set of parameterisations is guided by the desire for a weak dependence of the χ^2 function on the initial scale Q^2_0, and by the observed saturation of the χ^2 when the number of parameters becomes too large. This is demonstrated in figure 24 for the fit to H1 data alone. The functions without a term $\propto \sqrt{x}$ in the A distribution, see table 8, yield a steady decrease of χ^2 with Q^2_0.

Stability is observed for $Q^2_0 \geq 4$ GeV^2 for the other parameterisations. Three of them have a similar χ^2. For the H1 fit the parameterisation CP3 is chosen. The functions CP4 and CP8 have one more parameter but only one unit of χ^2 is gained which points to saturation of the parameter list. Although for CP7 a somewhat better χ^2 is found, this parameterisation is not considered. It yields a too large gluon momentum as compared to the other fits performed, including those using H1 and BCDMS data. These all agree for the gluon momentum fraction among each other and also with a previous analysis by the NMC collaboration [58]. In the CP7 fit to the H1 data apparently too many parameters are assigned to describe the quark distributions at large x since this leads also to a distorted V distribution.

The choice of parameterisation depends on the data set considered. In a similar study for the fit to H1 and BCDMS data, the parameterisation CP4 is chosen. Use of parameterisations with a high x term $(1 + \alpha x^\beta)$, as introduced by the CTEQ collaboration [86], worsens the χ^2 by eleven units and has thus not been considered further.

type	gluon	A
CP1	$1+ex$	$1+ex$
CP2	$1+d\sqrt{x}+ex$	$1+ex$
CP3	$1+ex$	$1+d\sqrt{x}+ex$
CP4	$1+d\sqrt{x}+ex$	$1+d\sqrt{x}+ex$
CP5	$1+ex$	$1+ex+fx^2$
CP6	$1+d\sqrt{x}+ex$	$1+ex+fx^2$
CP7	$1+ex$	$1+d\sqrt{x}+ex+fx^2$
CP8	$1+d\sqrt{x}+ex$	$1+d\sqrt{x}+ex+fx^2$

Table 8: *Types of parameterisations of the xg and A distributions at the initial scale Q_0^2.*

References

[1] For recent reviews see:
W. Van Neerven, *Deep-Inelastic Lepton-Hadron Scattering as a Test of Perturbative QCD*, Nucl. Phys. **B79** Proc. Suppl. (1999) 79, Proc. DIS'99 Workshop, Zeuthen, 1999, ed. by J. Blümlein and T. Riemann, hep-ph/9905503 (1999);
M. Klein, *Structure Functions in Deep-Inelastic Lepton-Nucleon Scattering*, Proc. Lepton-Photon Symposium, Stanford, August 1999, World Scientific, Singapore, ed. by J. Jaros and M. Peskin, p. 467, hep-ex/0001059 (2000).

[2] H1 Collaboration, I. Abt et al., Nucl.Phys. **B407** (1993) 515.

[3] ZEUS Collaboration, M. Derrick et al., Phys. Lett. **B316** (1993) 412.

[4] Yu. L. Dokshitzer, Sov. Phys. JETP **46** (1977) 641;
V. N. Gribov and L. N. Lipatov, Sov. J. Nucl. Phys. **15** (1972) 438 and 675;
G. Altarelli and G. Parisi, Nucl. Phys. **B126** (1977) 298.

[5] E. A. Kuraev, L. N. Lipatov and V. S. Fadin, Sov. Phys. JETP **44** (1976) 443;
E. A. Kuraev, L. N. Lipatov and V. S. Fadin, Sov. Phys. JETP **45** (1977) 199;
Y. Y. Balitsky and L. N. Lipatov, Sov. Journ. Nucl. Phys. **28** (1978) 822.

[6] M. Ciafaloni, Nucl. Phys. **B296** (1988) 49;
S. Catani, F. Fiorani and G. Marchesini, Nucl. Phys. **B336** (1990) 18;
G. Marchesini, Nucl. Phys. **B445** (1995) 49.

[7] L. V. Gribov, E. M. Levin and M. G. Ryskin, Phys. Rep. **100** (1983) 1.

[8] H1 Collaboration, S. Aid et al., Nucl. Phys. **B470** (1996) 3.

[9] ZEUS Collaboration, M. Derrick et al., Zeitschrift f. Physik **C72** (1996) 399.

[10] H1 Collaboration, C. Adloff et al., Nucl. Phys. **B497** (1997) 3.

[11] H1 Collaboration, S. Aid et al., Phys. Lett. **B393** (1997) 452.

[12] H1 Collaboration, C. Adloff et al., Eur. Phys. J. **C13** (2000) 609.

[13] BCDMS Collaboration, A.C. Benvenuti et al., Phys. Lett. **B223** (1989) 485;
CERN preprint CERN-EP/89-06.

[14] A. Blondel and F. Jacquet, Proc. ep Facility for Europe, Amsterdam 1979, DESY 79/48 (1979) 391.

[15] U. Bassler and G. Bernardi, Nucl. Instr. and Meth. **A361** (1995) 197.

[16] S. Bentvelsen, J. Engelen and P. Kooijman, Proc. Workshop on HERA Physics, Vol 1, eds. W. Buchmüller and G. Ingelman, Hamburg, DESY (1992), p. 25;
K. C. Höger, ibid, p. 43.

[17] H1 Collaboration, I. Abt et al., Nucl. Instr. and Meth. **A386** (1997) 310 and **A386** (1997) 348.

[18] T. C. Awes et al., Nucl. Instr. Meth. **A311** (1992) 130.

[19] R. Appuhn et al., Nucl. Instr. and Meth. **A386** (1996) 397.

[20] W. Eick et al., Nucl. Instr. and Meth. **A386** (1997) 81.

[21] B. Andrieu et al., Nucl. Instr. and Meth. **A336** (1993) 460.

[22] B. Andrieu et al., Nucl. Instr. and Meth. **A336** (1993) 499.

[23] H1 Collaboration, I. Abt et al., Z. Phys. **C66** (1995) 529.

[24] A. A. Glazov, PhD Thesis, Berlin, Humboldt-University, 1998, DESY-Thesis-1998-005; also at
http://www-h1.desy.de/publications/theses_list.html.

[25] G. A. Schuler and H. Spiesberger, Proc. Workshop on HERA Physics, Vol 3, eds. W. Buchmüller and G. Ingelman, Hamburg, DESY (1992), p. 1419.

[26] A. Kwiatkowski, H. Spiesberger and H.-J. Möhring, Comp. Phys. Comm. **69** (1992) 155.

[27] L. Lönnblad, Comp. Phys. Comm. **71** (1992) 15.

[28] N. H. Brook et al., *Tuning Monte Carlo Event Generators to HERA Data*, Workshop on Future Physics at HERA, eds. G. Ingelmann, A. DeRoeck and R. Klanner, Hamburg, DESY (1996), p. 613.

[29] N. H. Brook et al., *A Comparison of Deep-Inelastic Scattering Monte Carlo Event Generators to HERA Data*, Proc. Workshop 1998/99 on Monte Carlo Generators for HERA Physics, eds. T. Doyle, G. Grindhammer and G. Ingelmann, Hamburg, DESY (1999).

[30] G. Gustafson and U. Pettersson, Nucl. Phys. **B306** (1988) 746;
B. Andersson et al., Z. Phys. **C43** (1989) 625.

[31] T. Sjöstrand and M. Bengtsson, Comp. Phys. Comm. **43** (1987) 367.

[32] G. Ingelman, A. Edin and J. Rathsman, Comp. Phys. Comm. **101** (1997) 108.

[33] A. Courau and P. Kessler, Phys. Rev. **D46** (1992) 117.

[34] G. Marchesini et al., Comp. Phys. Comm. **67** (1992) 465.

[35] V.V. Arkadov, PhD Thesis, Berlin, Humboldt-University, 2000, DESY-Thesis-2000-046; also at
http://www-h1.desy.de/publications/theses_list.html.

[36] R. Engel and J. Ranft, Phys. Rev. **D54** (1996) 4244.

[37] A. Capella et al., Phys. Lett. **B337** (1994) 358.

[38] J. Blümlein, private communication.

[39] R. Brun et al., GEANT3 User's Guide, CERN-DD/EE 84-1, Geneva (1987).

[40] M. Glück, E.Reya and A.Vogt, Z. Phys. **C67** (1995) 433.

[41] R. Wallny, PhD Thesis, University of Zürich, in preparation; also at
http://www-h1.desy.de/publications/theses_list.html.

[42] D. Eckstein, PhD Thesis, Berlin, Humboldt-University, in preparation; also at
http://www-h1.desy.de/publications/theses_list.html.

[43] H1 Collaboration, C. Adloff et al., DESY preprint 00-085, hep-ex/0006017 (2000), subm. to Eur.Phys.J. **C**.

[44] Particle Data Group Report, D.E. Groom et al., Eur. Phys. J. **C15** (2000) 1.

[45] A. Arbuzov et al., Comput. Phys. Comm. **94** (1996) 128.

[46] For access to the data and full error matrix see:
http://www-h1.desy.de/h1/www/publications/htmlsplit/DESY-00-181.long.html

[47] C. Callan and D.J. Gross, Phys. Rev. Lett. **22** (1969) 156.

[48] G. Altarelli and G. Martinelli, Phys. Lett. **B76** (1978) 89;
M. Glück and E. Reya, Nucl. Phys. **B145** (1978) 24.

[49] E. B. Zijlstra and W. van Neerven, Nucl. Phys. **B383** (1992) 525.

[50] A.D. Martin, R.G. Roberts, W.J. Stirling and R. Thorne, Eur. Phys. J. **C18** (2000) 117.

[51] J. Bartels, K. Golec-Biernat and K. Peters, Eur. Phys. J. **C17** (2000) 121.

[52] C. Pascaud and F. Zomer, LAL preprint, LAL/95-05 (1995).

[53] L. Bauerdick, A. Glazov and M. Klein, *Future Measurement of the Longitudinal Proton Structure Function at HERA*, Proc. Workshop on Future Physics at HERA, eds. G. Ingelmann, A. DeRoeck and R. Klanner, Hamburg, DESY (1996), p. 77; hep-ex/9609017 (1996).

[54] P. W. Johnson and W. K. Tung, Phys. Rev. **D16** (1977) 2769.

[55] K. Prytz, Phys. Lett. **B311** (1993) 286.

[56] J. Bartels, K. Charchula and J. Feltesse, Proc. Workshop on HERA Physics, Vol 1, eds. W. Buchmüller and G. Ingelman, Hamburg, DESY (1992), p.193.

[57] ZEUS Collaboration, J. Breitweg et al., Eur. Phys. J. **C7** (1999) 609.

[58] M. Arneodo et al., NMC Collaboration, Phys. Lett. **B309** (1993) 222.

[59] M. Botje, QCDNUM, ZEUS internal notes 98-062(1998) and 99-027(1999); Phys. Lett. **B472** (2000) 175.

[60] A. Milsztaijn and M. Virchaux, Phys. Lett. **B274** (1992) 221.

[61] A. Alekhin, IHEP-2000-39, hep-ph/0011002 (2000).

[62] A. Vogt, Proc. DIS'99, Nucl. Phys. **B79** Proc. Suppl. (1999)102, ed. by J. Blümlein and T. Riemann; hep-ph/9906337.

[63] E. Laenen et al., Nucl. Phys. **B392** (1993) 162;
S. Riemersma, J. Smith and W. van Neerven, Phys. Lett. **B347** (1995) 143.

[64] CCFR Collaboration, A.O. Bazarko et al., Z. Phys. **C65** (1995) 189.

[65] E866/NuSea Collaboration, E.A. Hawker et al., Phys. Rev. Lett. **80** (1998) 3715.

[66] H. Georgi and H.D. Politzer, Phys. Rev. **D14** (1976) 1829.

[67] W. Furmanski and R. Petronzio, Z. Phys. **C11** (1982) 293.

[68] C. Pascaud and F. Zomer, DESY preprint, DESY 96-266 (1996).

[69] V. Barone, C. Pascaud and F. Zomer, Eur. Phys. J. C **12** (2000) 243.

[70] J. Blümlein et al., *A detailed comparison of NLO QCD evolution codes*, Workshop on Future Physics at HERA, eds. G. Ingelmann, A. DeRoeck and R. Klanner, Hamburg, DESY (1996), p. 23.

[71] A. Vogt, private communication.

[72] H.L. Lai et al., CTEQ Collaboration, Phys. Rev. **D55** (1997) 1280.

[73] T. Hadig, PhD Thesis, RWTH Aachen, preprint PITHA 99/41 (1999).
The program is based on J. Blümlein and A. Vogt, Phys. Rev. **D58** (1998) 014020.

[74] L. W. Whitlow et al., Phys. Lett. **B282** (1992) 475.

[75] A.D. Martin et al., Eur. Phys. J. **C4** (1998) 463.

[76] A. Milsztaijn et al., Z. Phys. **C49** (1991) 527.

[77] S.J. Brodsky and G. Farrar, Phys. Rev. Lett. **31** (1973) 1153.

[78] W.L. van Neerven and A. Vogt, Nucl. Phys. **B588** (2000) 345.

[79] J. Santiago and F.J. Yndurain, Nucl. Phys. **B563** (1999) 45 and Nucl. Phys. Proc. Suppl. **86** (2000) 69.

[80] NMC Collaboration, M. Arneodo et al., Nucl. Phys. **B483** (1997) 3.

[81] W. Melnitchouk and A.W. Thomas, Phys.Rev. **C52** (1995) 3373.

[82] H1 Collaboration, I. Abt et al., Nucl. Phys. **B545** (1999) 21.

[83] H1 Collaboration, C. Adloff et al., DESY preprint 00-145 (2000), hep-ex/0010054 (2000), subm. to. Eur. Phys. J. **C**.

[84] T. Adams et al., NuTeV Collaboration, hep-ex/9906038 (1999).

[85] M. Glück, E.Reya and A.Vogt, Eur. Phys. J. **C5** (1998) 461.

[86] CTEQ Collaboration, H.L. Lai et al., Phys. Rev. **D55** (1997) 1280;
hep-ph/9903282 (1999).

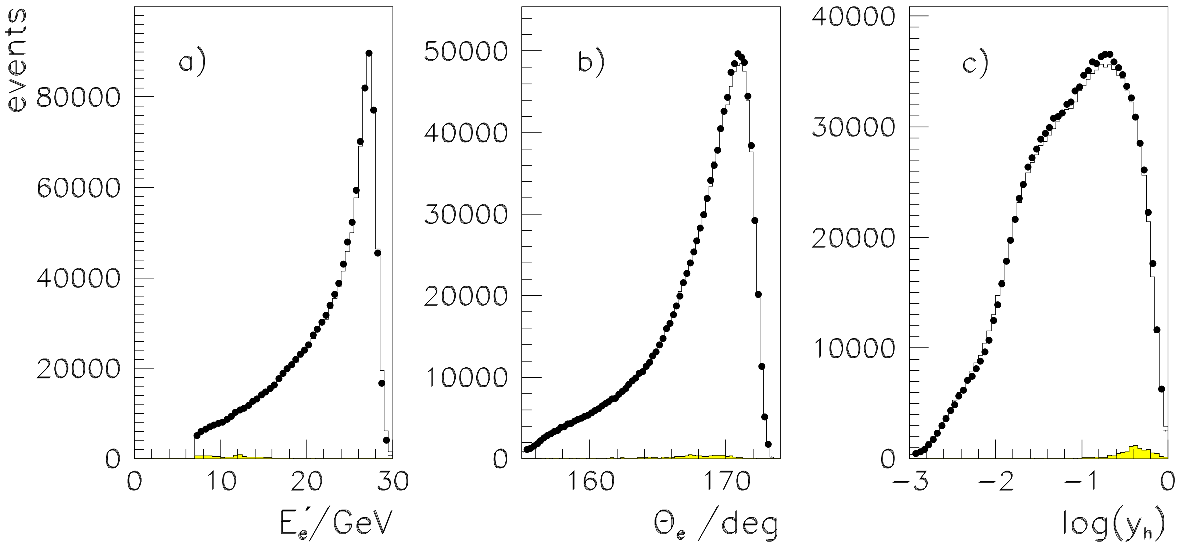

Figure 1: *Distributions of a) the energy, b) the polar angle of the scattered positron, and c) y_h for the data sample A taken in 1996/97 (solid points). The histograms show the simulation of DIS and the small photoproduction background (shaded), normalised to the luminosity of the data.*

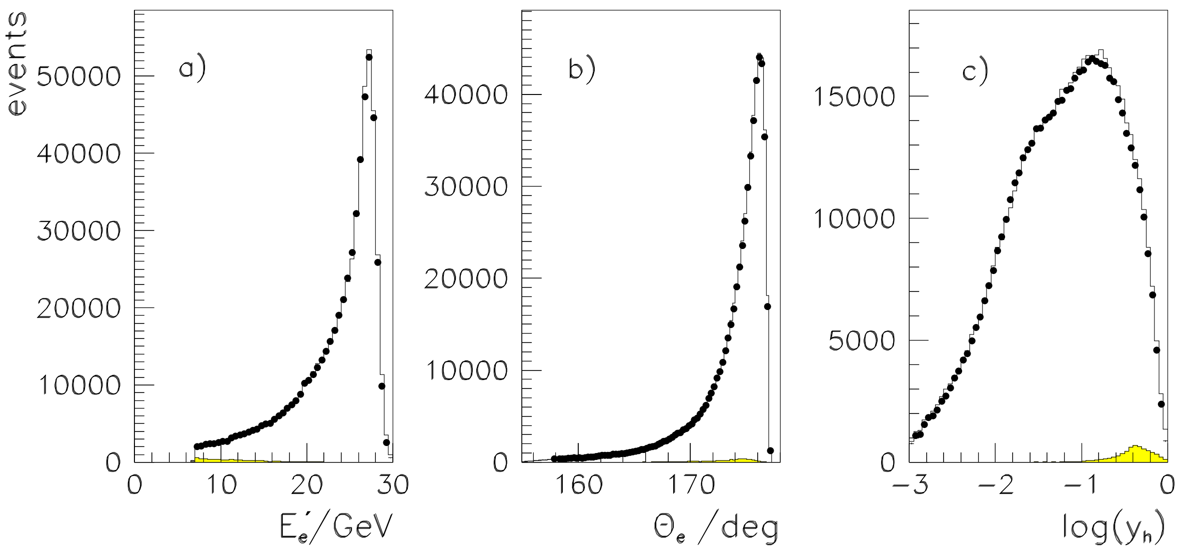

Figure 2: *Distributions of a) the energy, b) the polar angle of the scattered positron, and c) y_h for the low Q^2 data sample B taken in 1997. The histograms represent the simulation of DIS and the small photoproduction background (shaded), normalised to the luminosity of the data.*

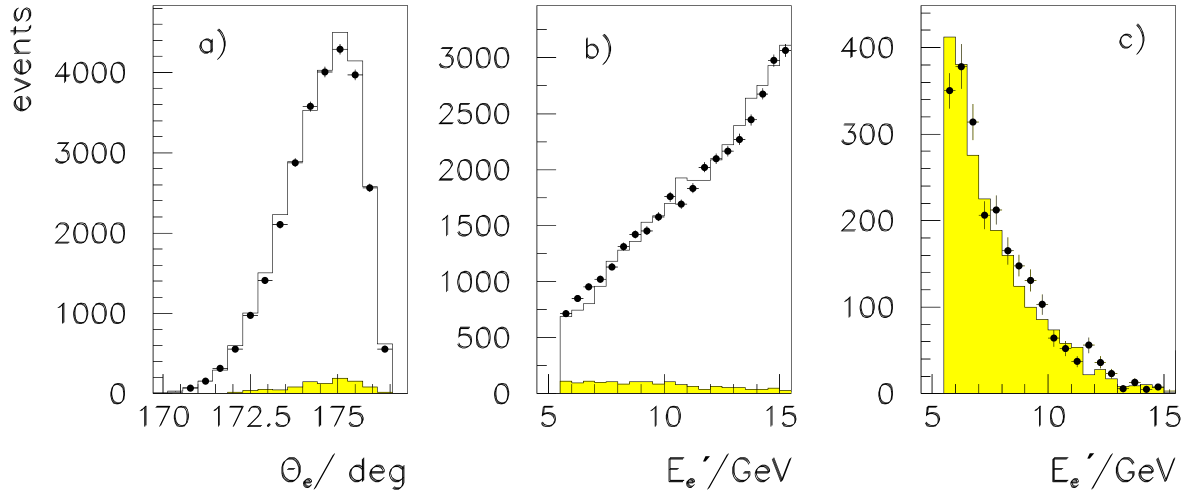

Figure 3: *Distributions illustrating the cross-section measurement at high* y $(0.46 < y < 0.82)$ *and low* Q^2 $(2 < Q^2 < 5$ GeV$^2)$ *for events in the BST acceptance range. DIS event distributions of a) the polar angle and b) the SPACAL energy of the scattered positron candidate. c) SPACAL energy distribution for tagged photoproduction events fulfilling the DIS event selection criteria, apart from the* $E - p_z$ *requirement. Solid points: H1 data; shaded histograms: simulation of photoproduction events; open histograms: added distributions of simulated DIS and photoproduction events.*

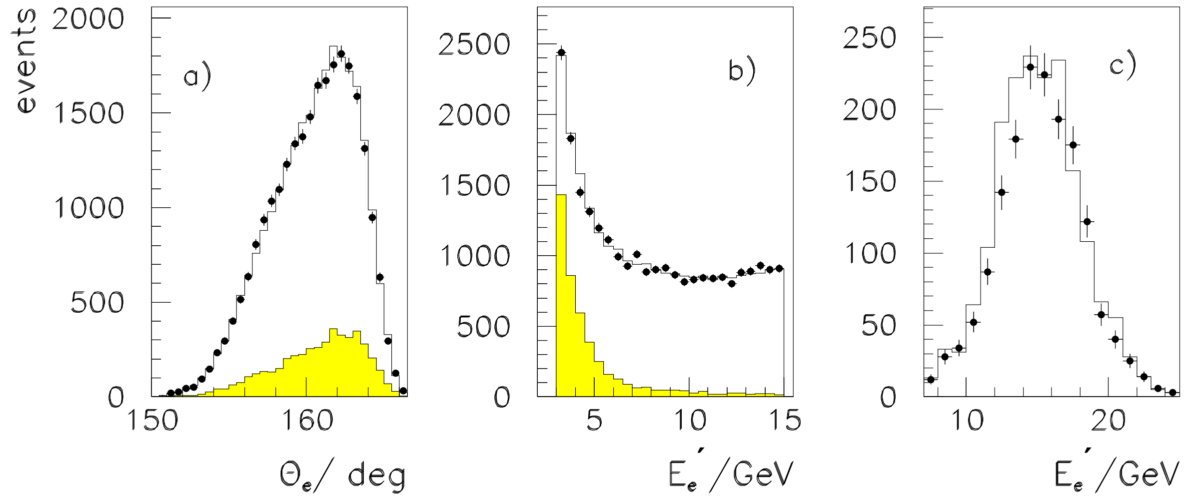

Figure 4: *Distributions illustrating the cross-section measurement at high* y $(0.46 < y < 0.89)$ *and large* Q^2 $(10 < Q^2 < 35$ GeV$^2)$*. a) Polar angle and b) SPACAL energy distributions before subtraction of the photoproduction background using the charge measurement by the CJC. Solid points: data with positive charge assignment. Shaded histogram: data with negative charge assignment. Open histogram: sum of data with negative charge assignment and DIS event simulation, normalized to the data luminosity. c) Spectrum of energy measured in the electron tagger for DIS candidate events with a linked track of either positive charge (solid points) or of negative charge (histogram).*

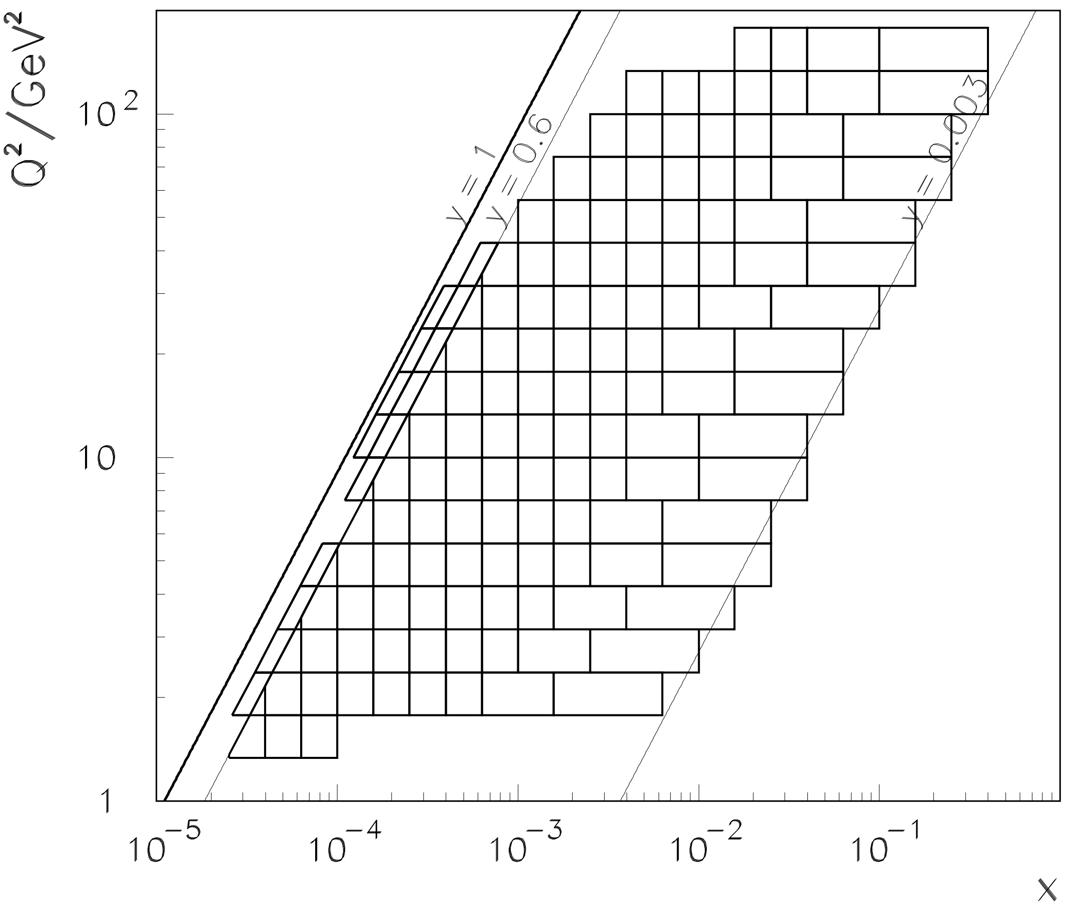

Figure 5: *Division of the (x, Q^2) plane for the measurement of the inclusive DIS cross section. At low y the bin size increases as the resolution deteriorates. At large y the data are binned in intervals of Q^2 and y in order to account for the y dependent effect of F_L on the cross-section and the variation of the systematics with y. The triangular regions inside the acceptance do not represent valid analysis bins.*

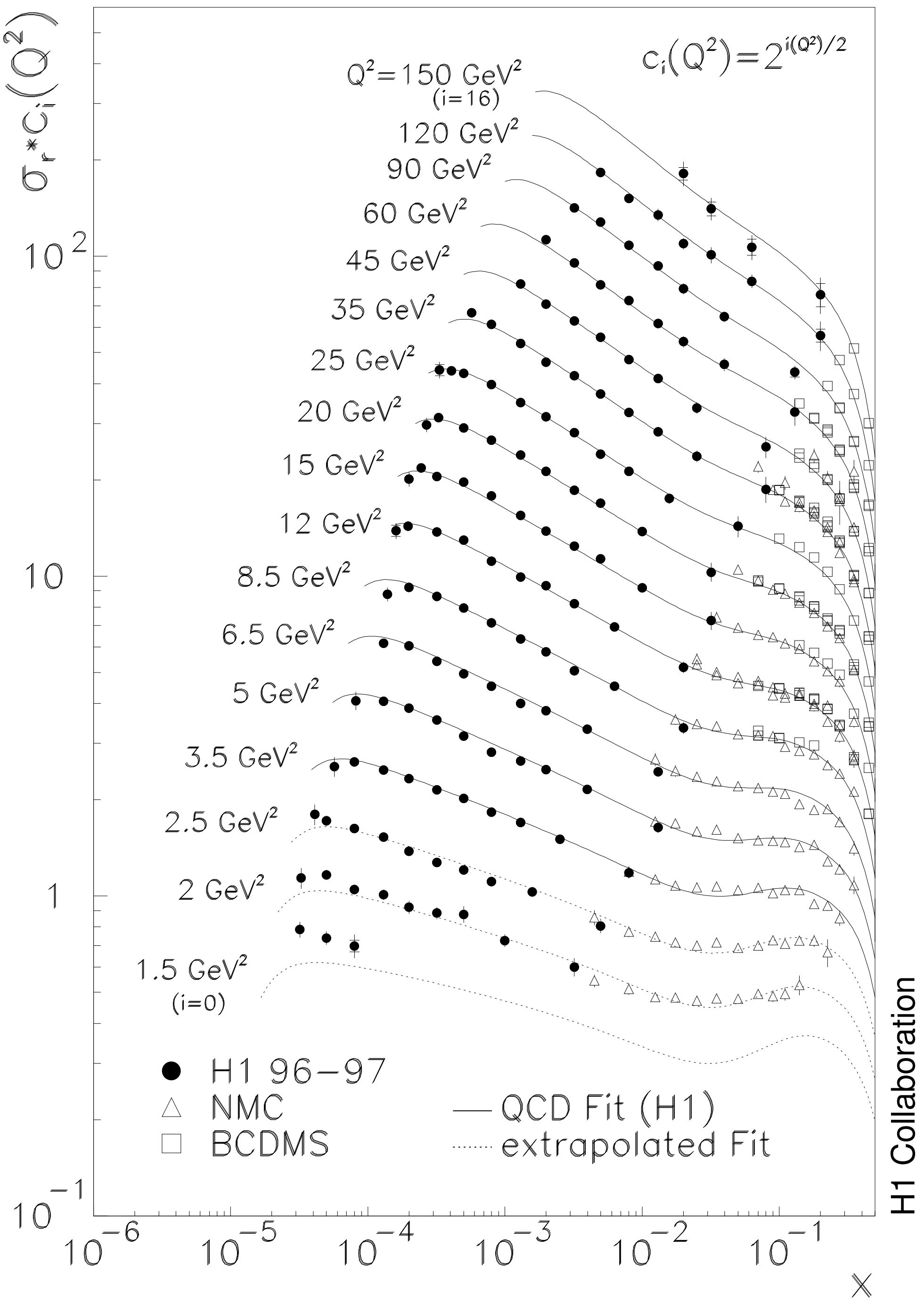

Figure 6: *Measurement of the reduced DIS scattering cross section (closed points). Triangles (squares) represent data from the NMC (BCDMS) muon-proton scattering experiments. The solid curves illustrate the cross section obtained in a NLO DGLAP QCD fit to the present data at low x, with $Q^2_{min} = 3.5$ GeV^2, and to the H1 data at high Q^2. The dashed curves show the extrapolation of this fit towards lower Q^2. The curves are labelled with the Q^2 value the data points belong to and scale factors are conveniently chosen to separate the measurements.*

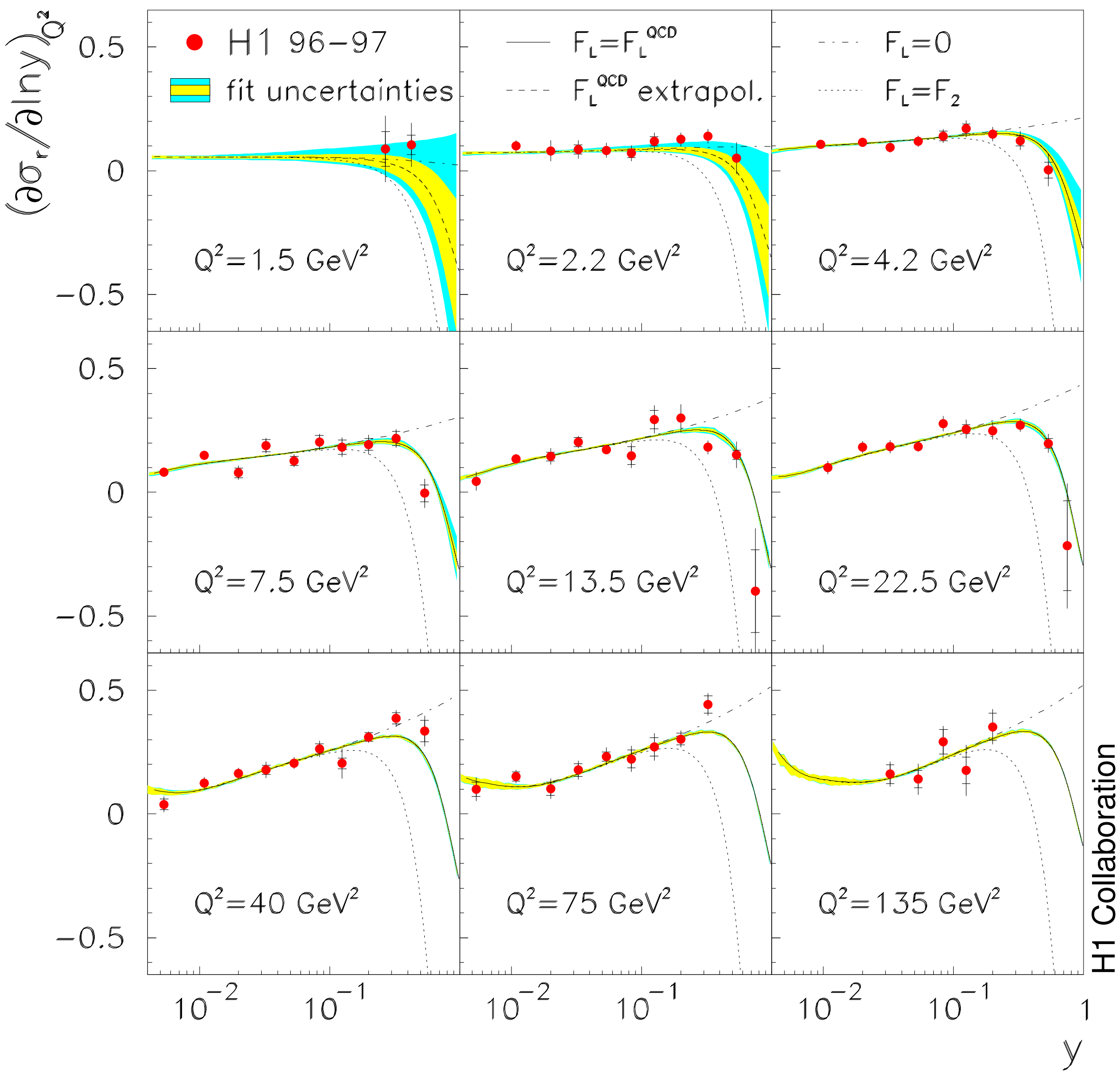

Figure 7: *Measurement of the derivative $\partial\sigma_r/\partial \ln y$ at fixed Q^2. The inner error bars represent the statistical errors and the total error bars the statistical and systematic errors, added in quadrature. The curves represent the QCD fit result to the H1 data, for $y < 0.35$ and $Q^2 \geq 3.5$ GeV^2, calculated with different assumptions about F_L. The solid curves use the QCD prediction of F_L, the dashed (dashed dotted) curves assume $F_L = F_2$ ($F_L = 0$). The inner error band is the experimental uncertainty of the fit result (section 7.2), the outer band represents the additional uncertainty due to the fit assumptions. The fit results shown for $Q^2 < 3.5$ GeV^2 (dashed) are obtained by backward extrapolation.*

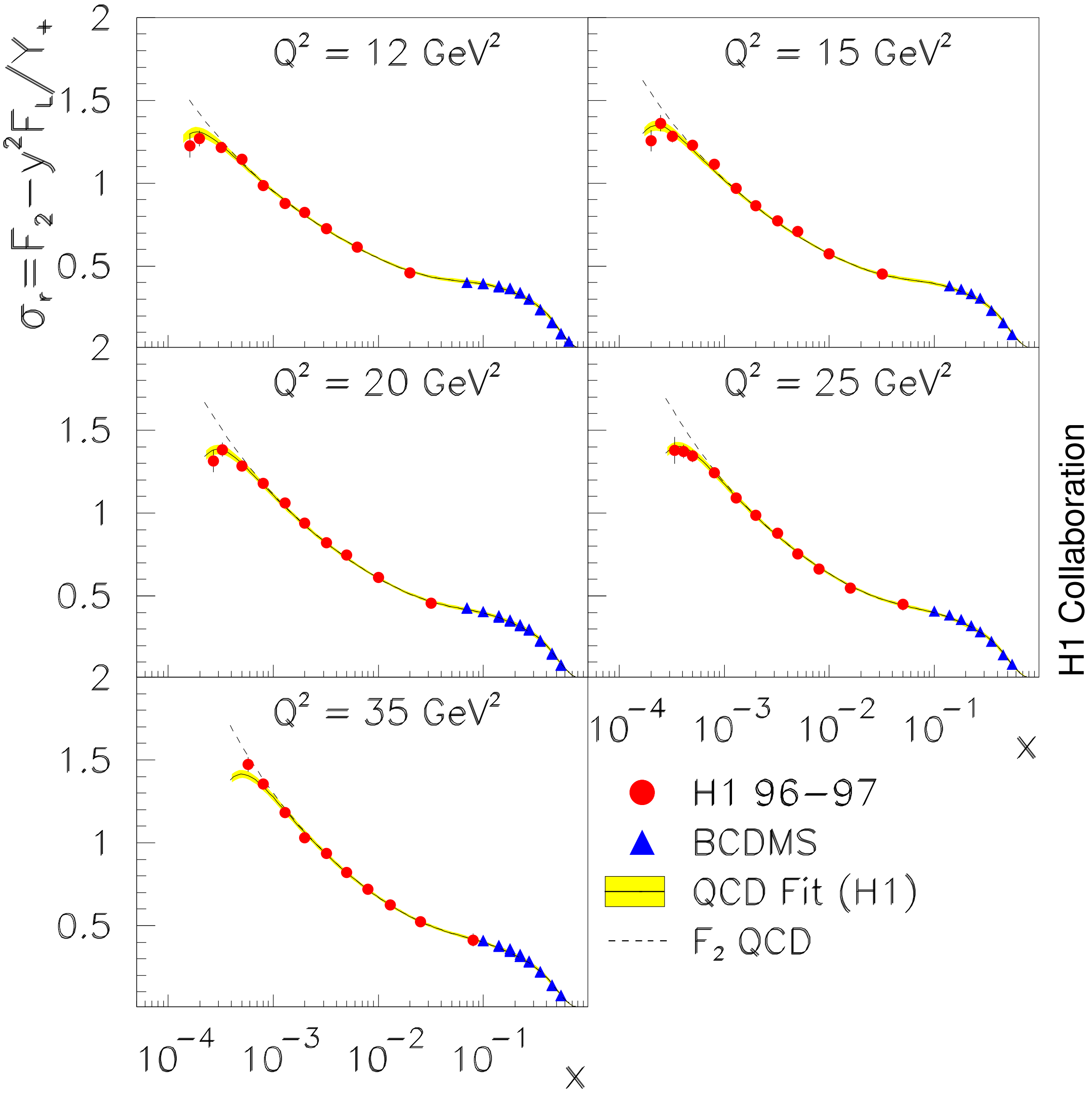

Figure 8: *Measurement of the reduced DIS scattering cross section (closed points). Triangles represent data from the BCDMS muon-proton scattering experiment. The curves represent a NLO QCD fit to the H1 data alone, using data with $y < 0.35$ and $Q^2 \geq 3.5$ GeV^2 . The dashed curves show the F_2 structure function as determined with this fit. The error bands represent the experimental and model uncertainty of the QCD fit.*

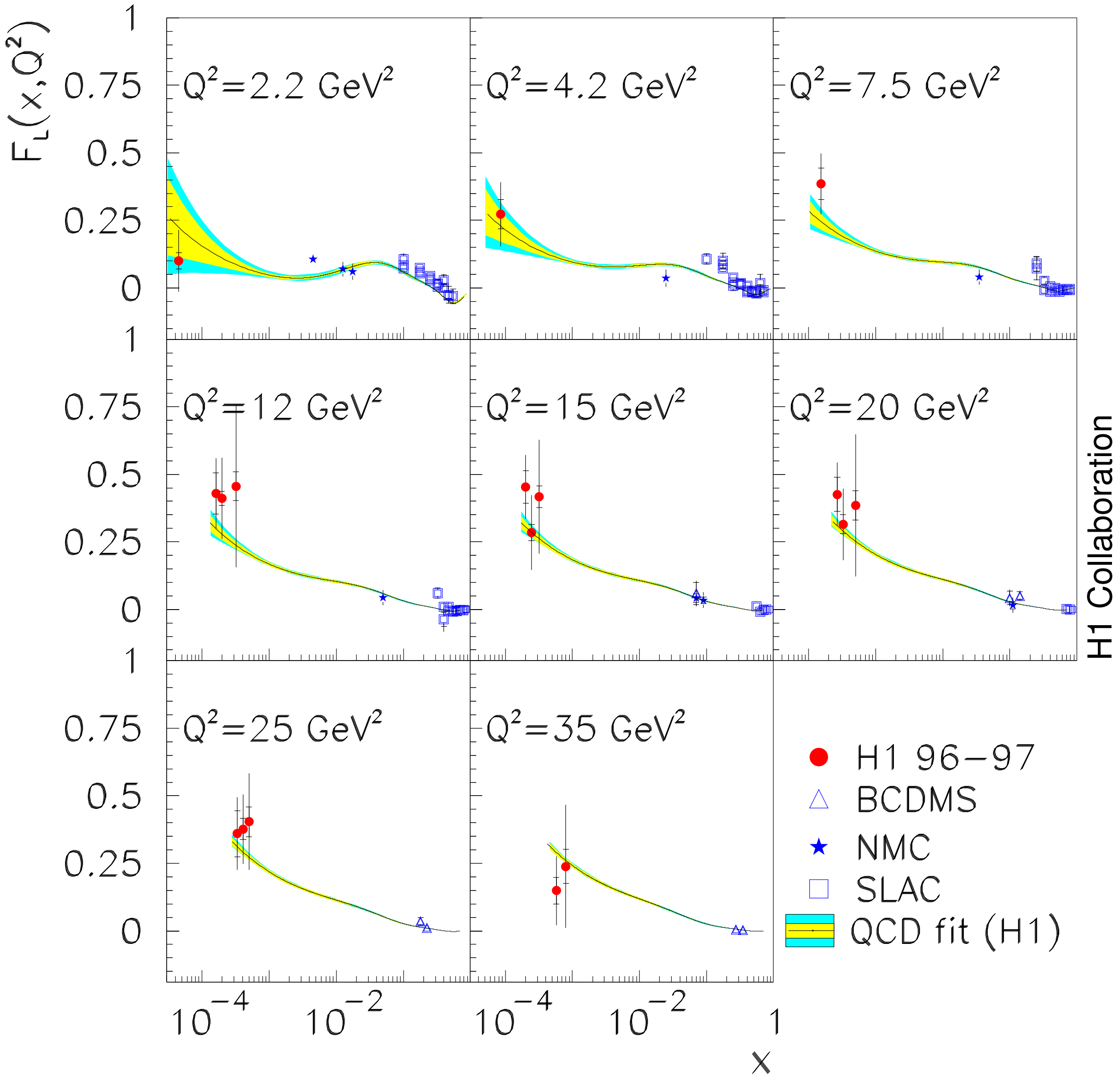

Figure 9: *The longitudinal structure function $F_L(x,Q^2)$ for different bins of Q^2 as obtained by H1 at low x, and by charged lepton-nucleon fixed target experiments at large x. The measurements for $Q^2 < 10$ GeV^2 are determined with the derivative method while the points for larger Q^2 are due to the extrapolation method. The error on the data points is the total uncertainty of the determination of F_L representing the statistical, the systematic and the model errors added in quadrature. The inner error bars show the statistical error. The error bands are due to the experimental (inner) and model (outer) uncertainty of the calculation of F_L using the NLO QCD fit to the H1 data for $y < 0.35$ and $Q^2 \geq 3.5$ GeV^2 .*

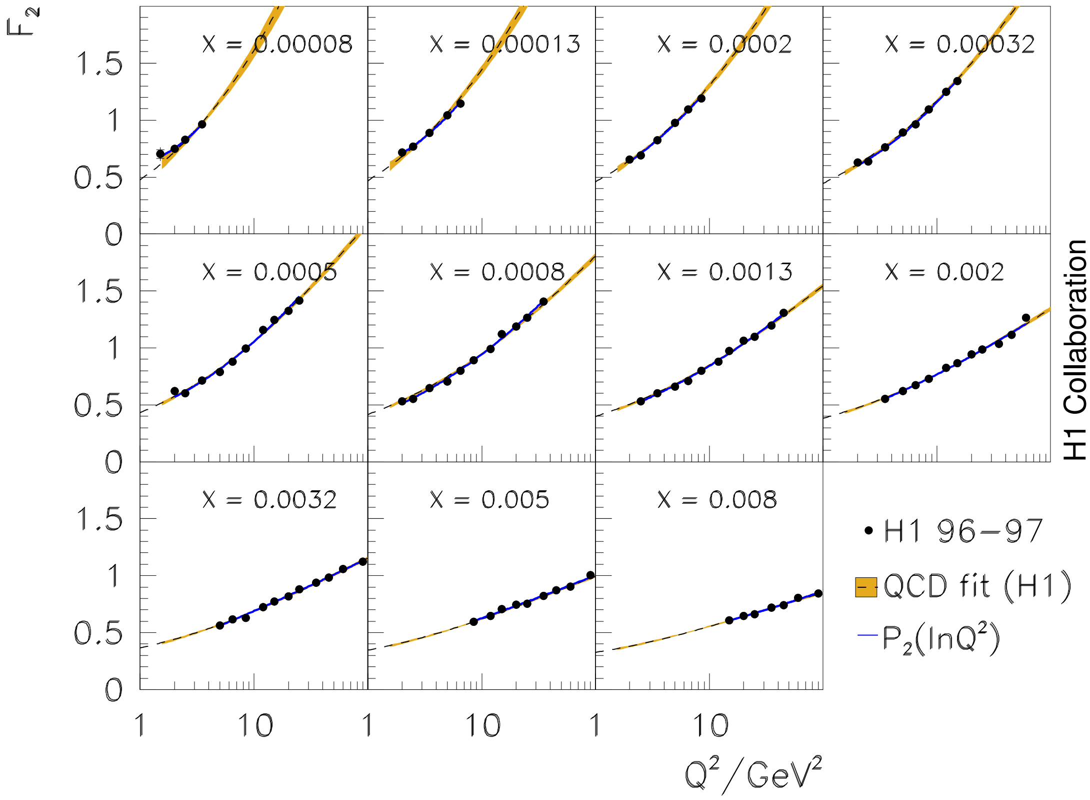

Figure 10: *Measurement of the proton structure function* $F_2(x, Q^2)$*, plotted as functions of* Q^2 *in bins of* x *(points). The solid lines represent fits to* F_2 *in bins of* x *according to a polynomial* $P_2(x, Q^2) = a(x) + b(x)\ln Q^2 + c(x)(\ln Q^2)^2$*. The dashed lines are obtained from the NLO QCD fit to the H1 data (section 7.2), for* $Q^2 \geq 3.5$ *GeV*^{2} *. The error bands are due to the experimental and model uncertainties in the QCD fit.*

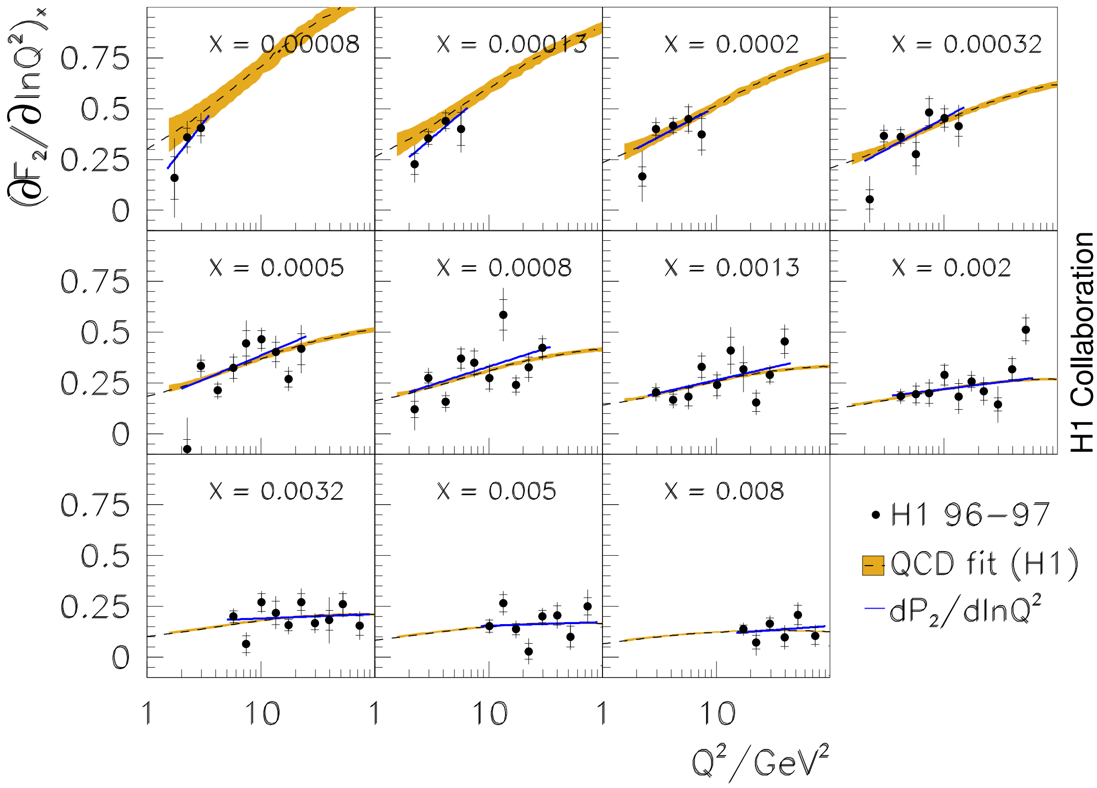

Figure 11: *Measurement of the partial derivative* $(\partial F_2/\partial \ln Q^2)_x$ *taken at fixed* x *and plotted as functions of* Q^2*. The error bars represent the quadratic sum of statistical and systematic errors. The straight solid lines are given by the function* $b(x) + 2c(x)\ln Q^2$ *determined in fits to* $F_2(x, Q^2)$ *at fixed* x*. The dashed lines represent the derivatives as calculated with the QCD fit to the H1 data. The error bands are due to the experimental and model uncertainties in the QCD fit which includes data for* $Q^2 \geq 3.5$ *GeV*^{2} *.*

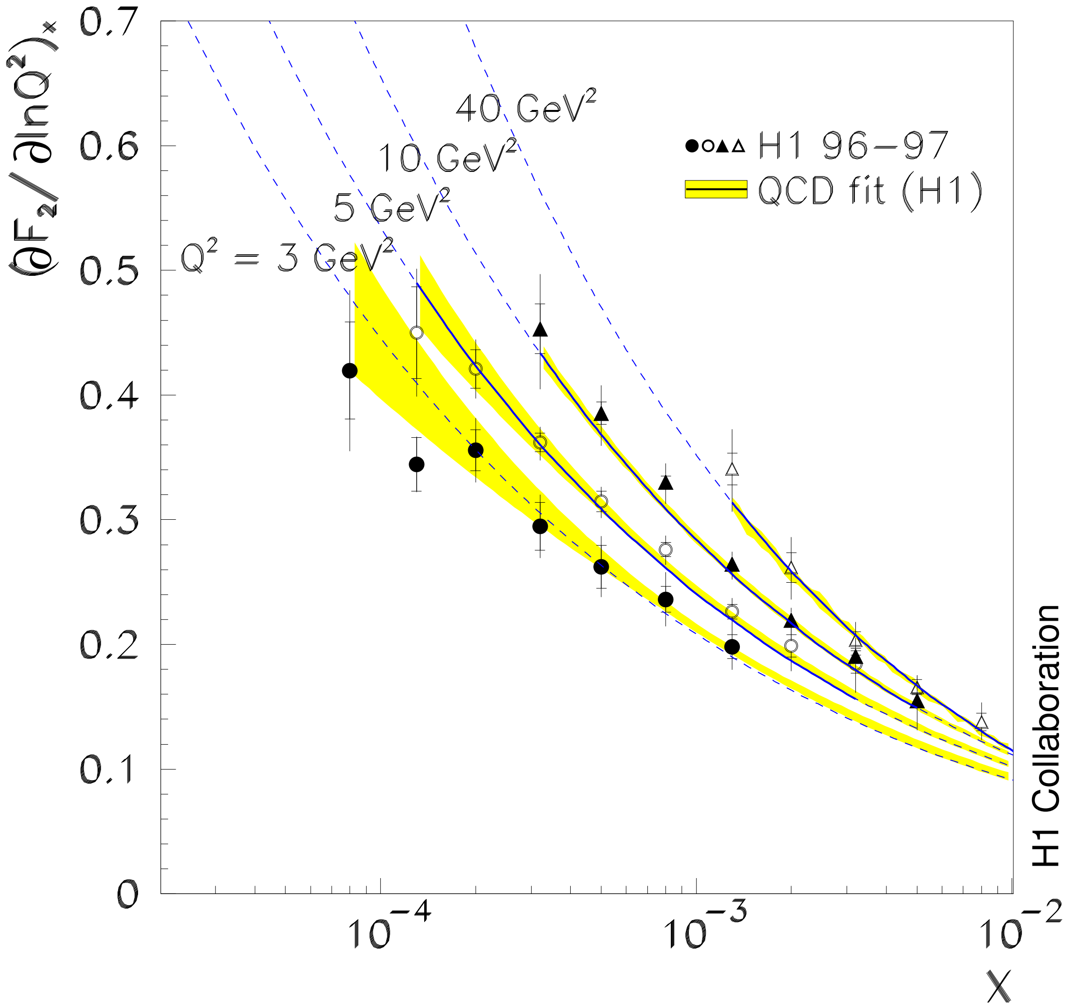

Figure 12: *The derivative* $(\partial F_2/\partial \ln Q^2)_x$ *plotted as functions of* x *for fixed* Q^2*, for the H1 data (symbols) and the QCD fit to the H1 data, for* $Q^2 \geq 3.5$ *GeV*^{2} *(solid lines). The dashed curves extrapolate this fit below* Q^2_{min} *and outside the range of* x*. The error bands represent the model uncertainty of the QCD analysis.*

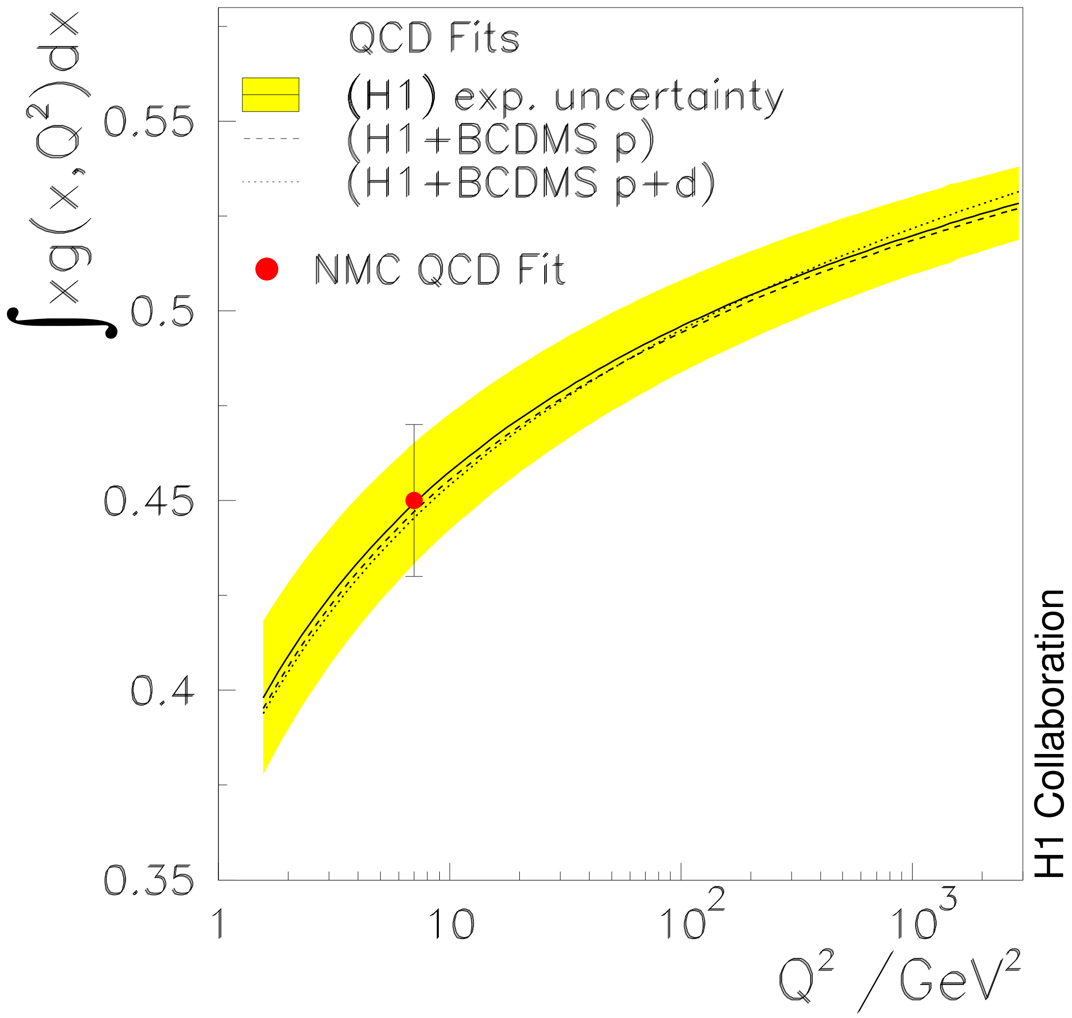

Figure 13: *The fraction of the proton momentum carried by gluons as a function of Q^2, obtained in different NLO DGLAP fits. Solid curve: fit to H1 data alone; dashed curve: fit to H1 and BCDMS proton data; dotted curve: fit to H1 ep and BCDMS μp and μd data. The shaded error band represents the experimental uncertainty in the analysis of the H1 data alone. The solid point is due to a QCD analysis by the NMC collaboration [58].*

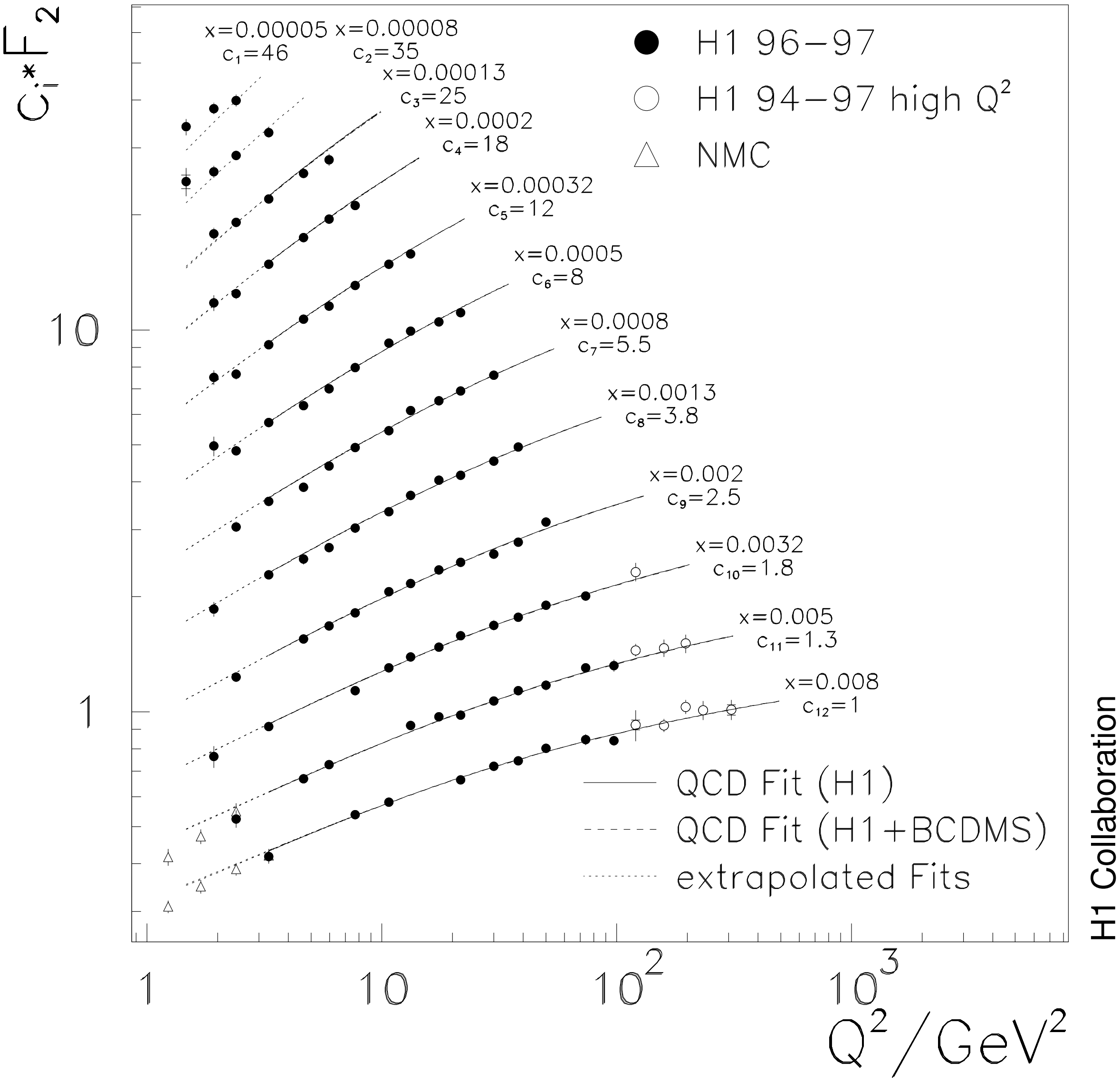

Figure 14: *Measurements of the proton structure function $F_2(x, Q^2)$ by the H1 and the NMC experiments. Solid curves: NLO DGLAP QCD fit to the H1 cross section data. Overlayed as dashed curves are the results of the QCD fit to the H1 ep and BCDMS μp data, for $y_\mu > 0.3$, which are indistinguishable from those of the pure H1 fit. Dotted curves: fit extrapolations at fixed x into the region below $Q^2 = 3.5$ GeV^2 .*

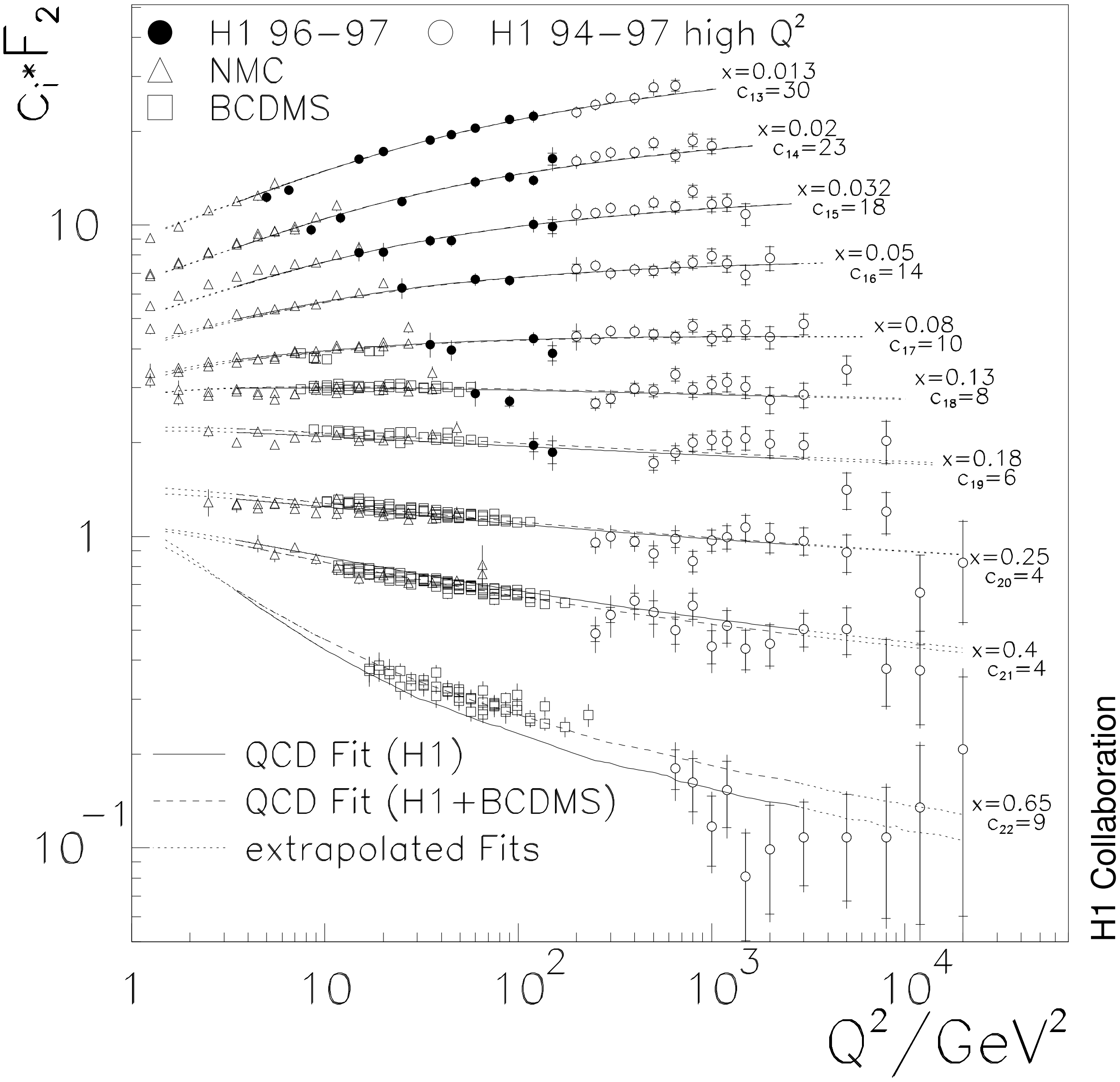

Figure 15: *Measurements of the proton structure function $F_2(x, Q^2)$ by the H1 experiment and by fixed target muon-proton scattering experiments. The error on the data points is the total measurement uncertainty. The inner error bars represent the statistical error. Solid curves: fit to the H1 cross section data. Dashed curves: fit to the H1 ep and BCDMS μp data, for $y_\mu > 0.3$. Dotted curves: extrapolations to data not used in the fit.*

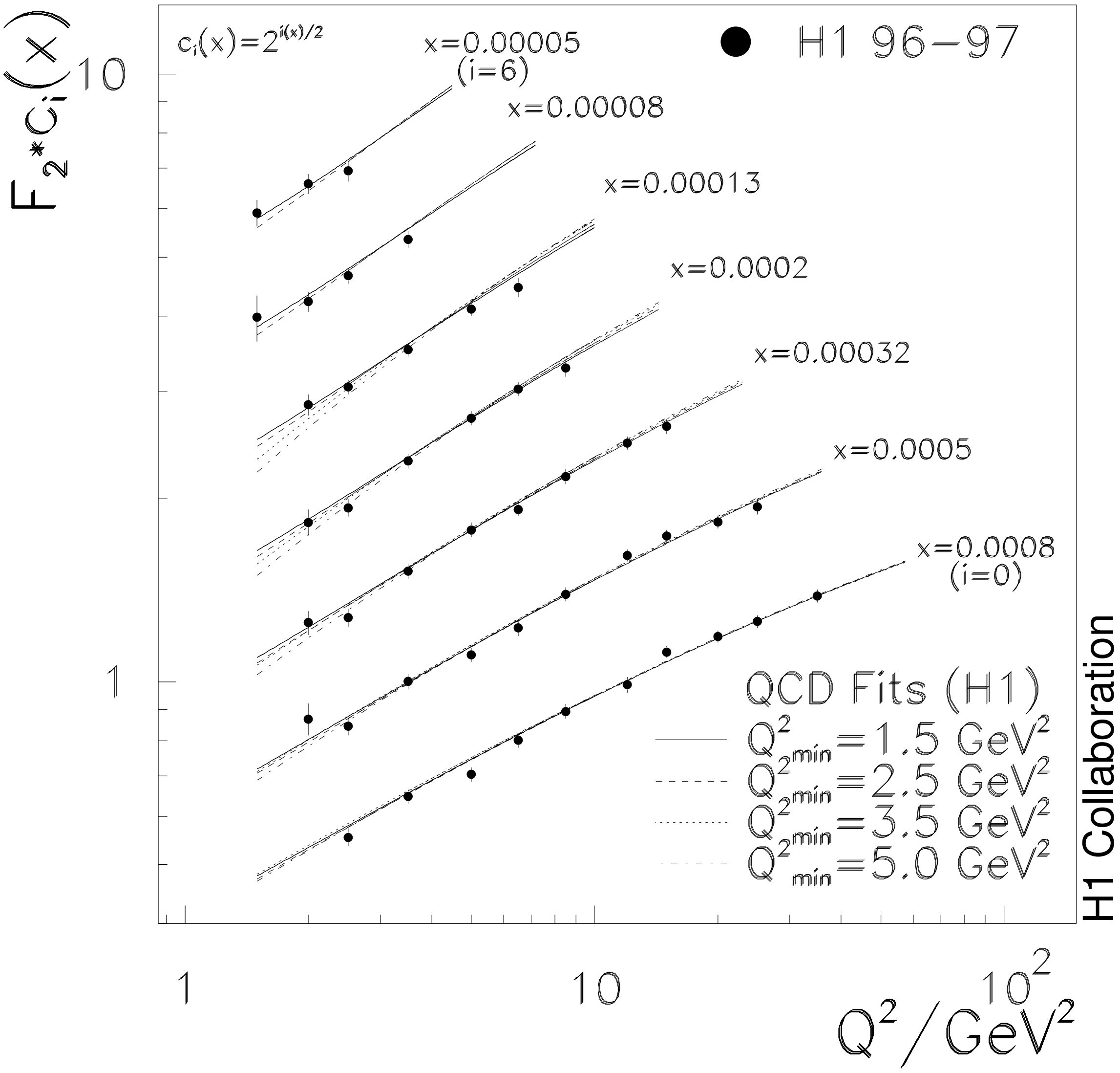

Figure 16: *Effect of the Q^2_{min} cut on the structure function F_2 in the DGLAP QCD fit to the H1 data (points). The curves represent fits with different minimum Q^2 values. The analysis uses $Q^2_{min} = 3.5$ GeV^2 as default.*

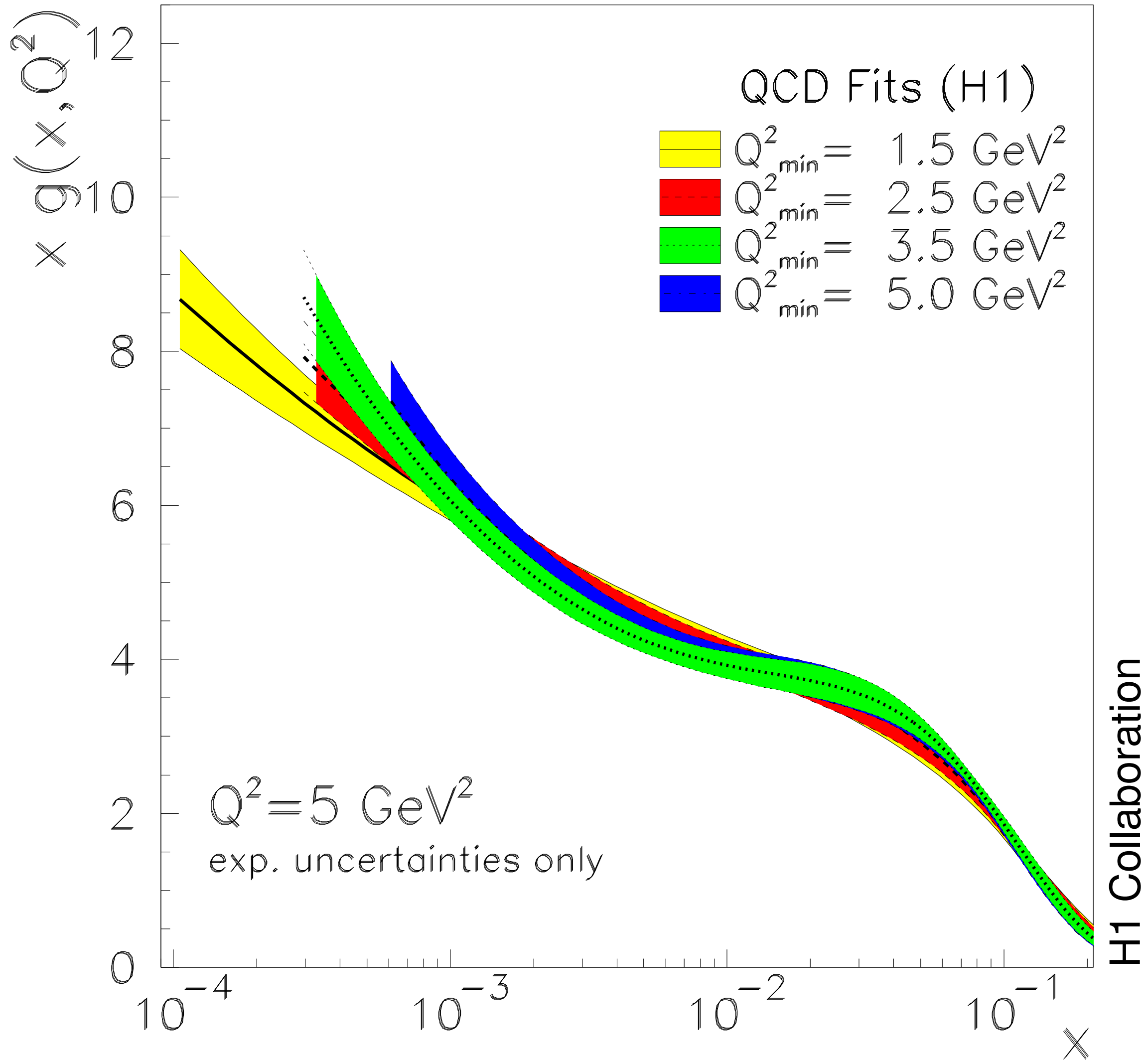

Figure 17: *Effect of the Q^2_{min} cut, applied in the DGLAP QCD fit to the H1 data, on the gluon distribution at $Q^2 = 5$ GeV^2 . The error bands represent the uncertainty of xg resulting from the measurement uncertainties only. The gluon distributions are shown down to x values corresponding to twice the minimum x values of the data which allow a Q^2 slope to be measured.*

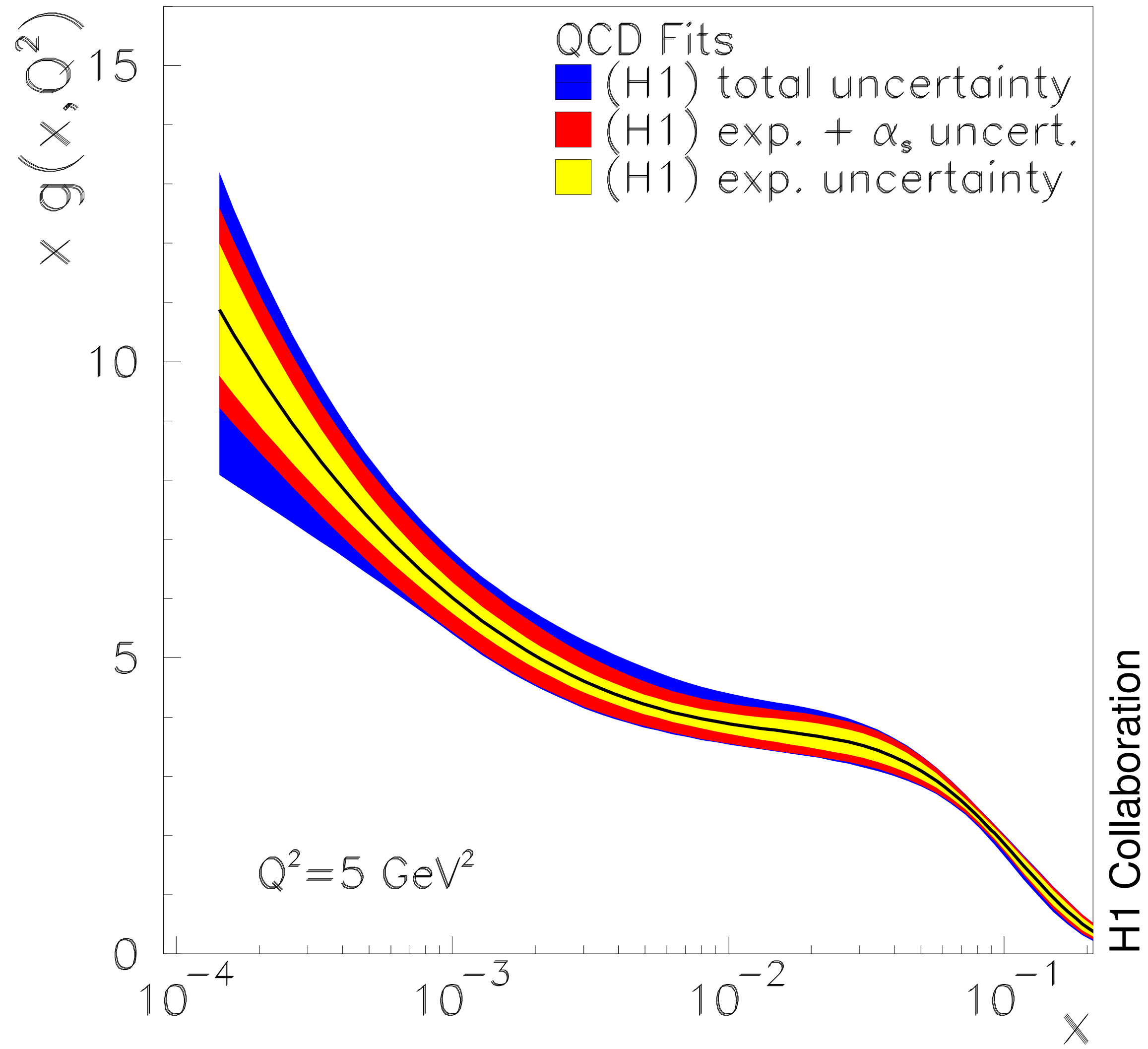

Figure 18: *The gluon distribution $xg(x, Q^2)$ at $Q^2 = 5$ GeV^2, determined in the NLO DGLAP QCD fit to the H1 data. Inner error band: experimental uncertainty; middle error band: effect of the experimental error and of the $\alpha_s(M_Z^2)$ uncertainty of ± 0.0017; outer error band: effect of experimental, α_s and model uncertainties.*

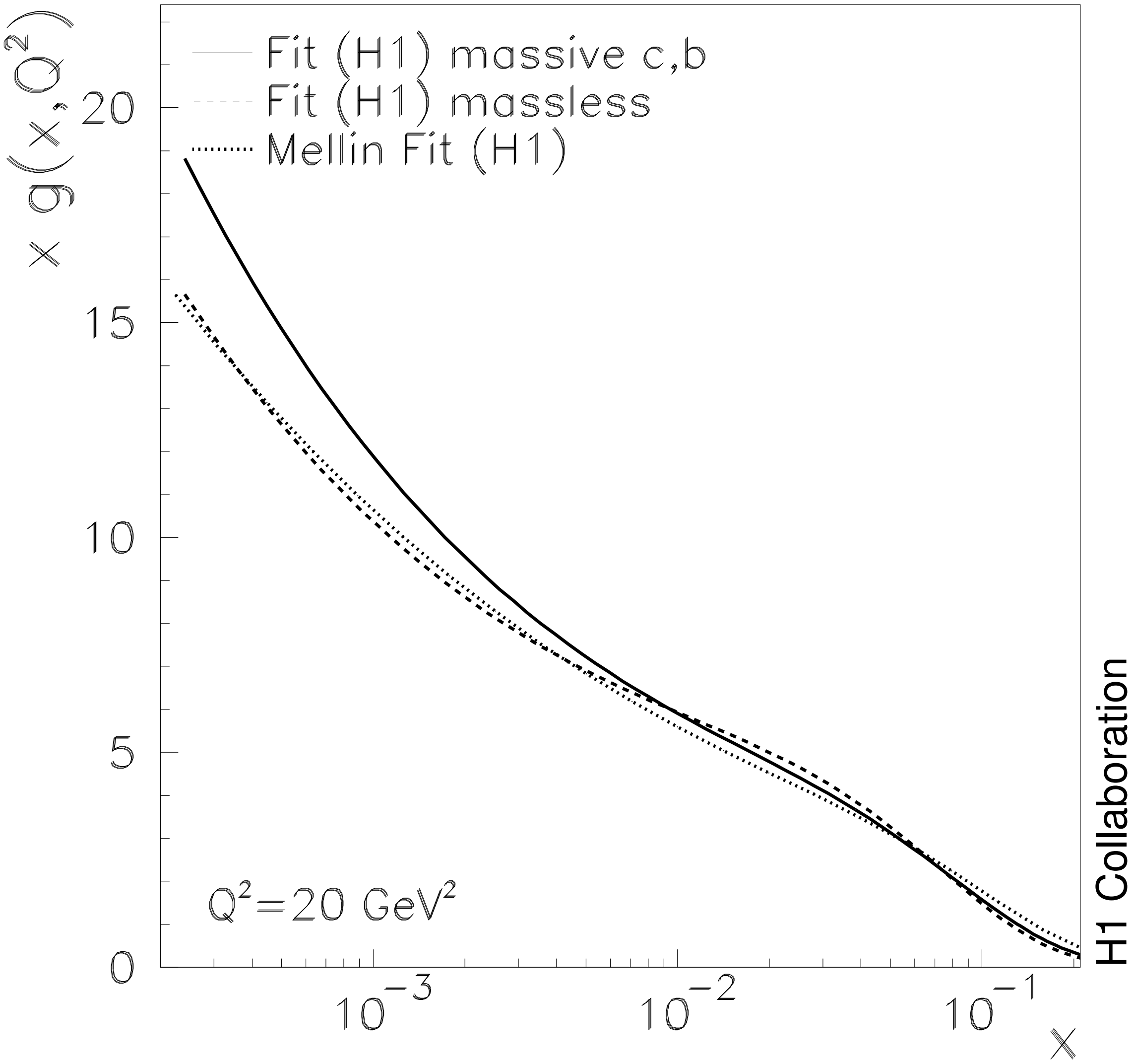

Figure 19: *Comparison of gluon distributions obtained in NLO DGLAP QCD fits to the H1 data, using different prescriptions: solid curve: standard fit using the massive heavy flavour scheme; dashed curve: fit in the massless scheme; dotted curve: fit in the massless scheme using a Mellin n space program.*

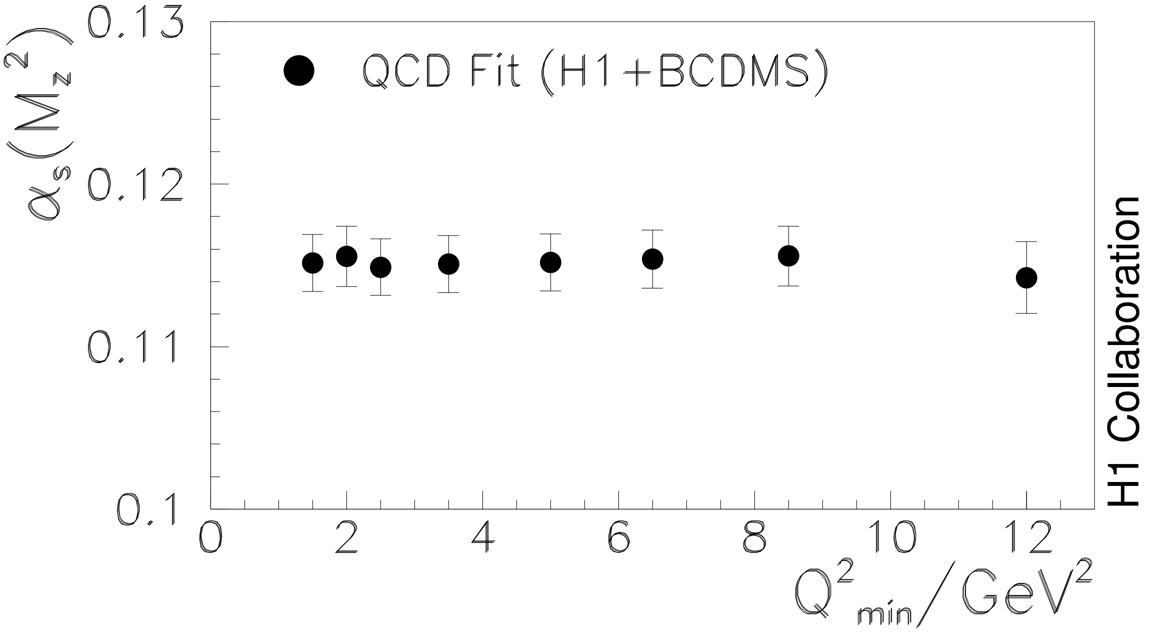

Figure 20: *Dependence of $\alpha_s(M_Z^2)$ obtained in fits to the H1 and BCDMS data on the minimum Q^2 value used. The error bars denote the experimental uncertainty of $\alpha_s(M_Z^2)$. Note that the BCDMS data have an intrinsic Q^2_{min} of 7.5 GeV^2 and are limited in this analysis to $y_\mu \geq 0.3$ (see text). An increase of Q^2_{min} implies that the minimum x rises correspondingly, i.e. from $x = 3.2 \cdot 10^{-5}$ at $Q^2_{min} = 1.5$ GeV^2 to $x = 8 \cdot 10^{-4}$ at $Q^2_{min} = 12$ GeV^2 .*

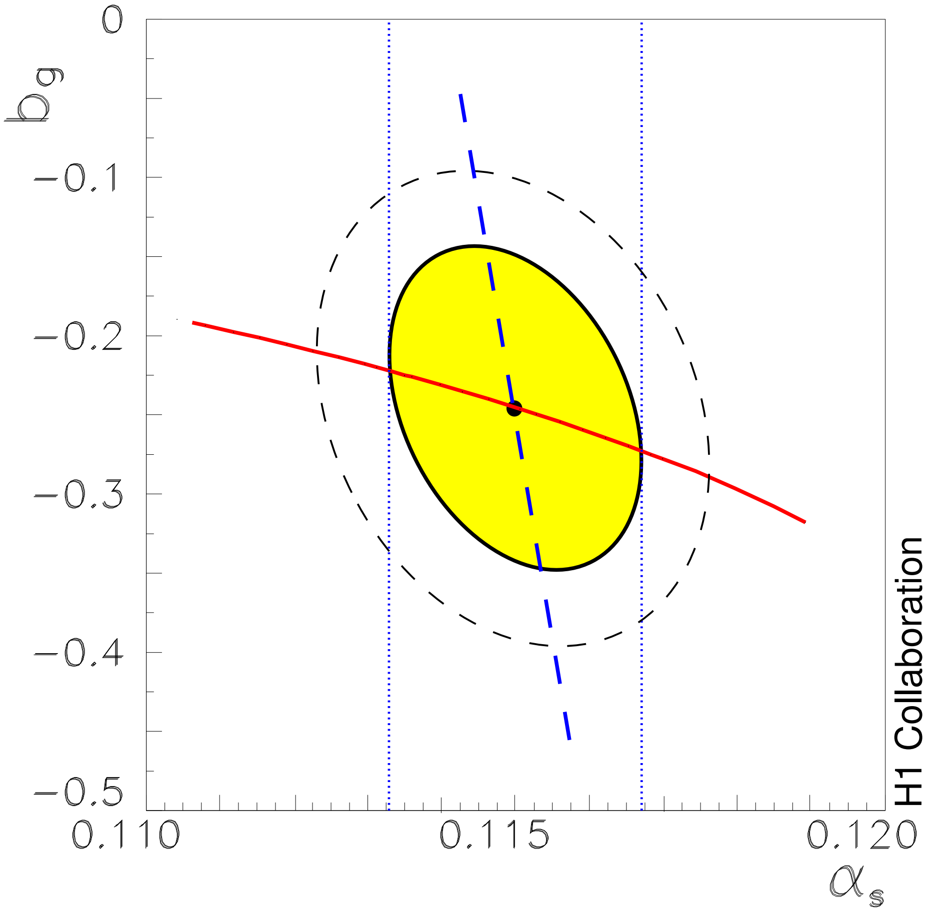

Figure 21: *The correlation of the gluon distribution parameter b_g with α_s in the fit to H1 and BCDMS data. The parameter b_g governs the low x behaviour of $xg(x, Q_0^2) \propto x^{b_g}$ for the chosen $Q_0^2 = 4\,$GeV^2. The solid (dashed) ellipse marks the $\chi^2 + 1$ ($\chi^2 + 2.3$) contour around the minimum of χ^2. The solid (dashed) line indicates the resulting value of b_g (α_s) for a given α_s (b_g) when all parameters but the latter are allowed to vary in the minimisation procedure. The correlation coefficient of b_g and α_s is -0.25.*

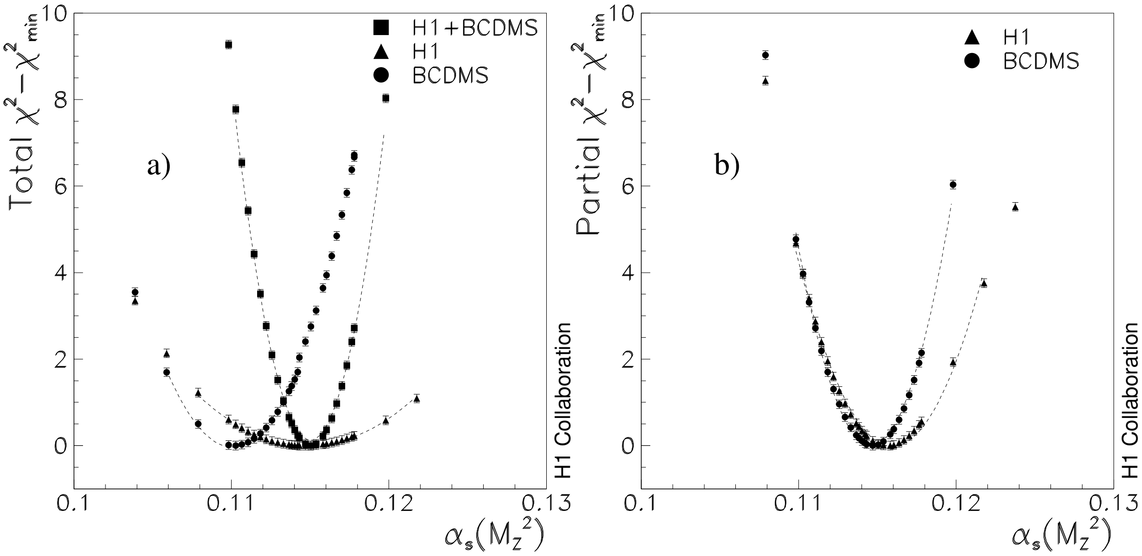

Figure 22: *Determination of the strong coupling constant $\alpha_s(M_Z^2)$ in NLO DGLAP QCD. a) total χ^2 for fits to the H1 ep and BCDMS μp data ($y_\mu > 0.3$) separately and for the fit using data of the two experiments combined; b) partial χ^2 contributions of the H1 and BCDMS proton data in the fit to determine α_s using both experiments.*

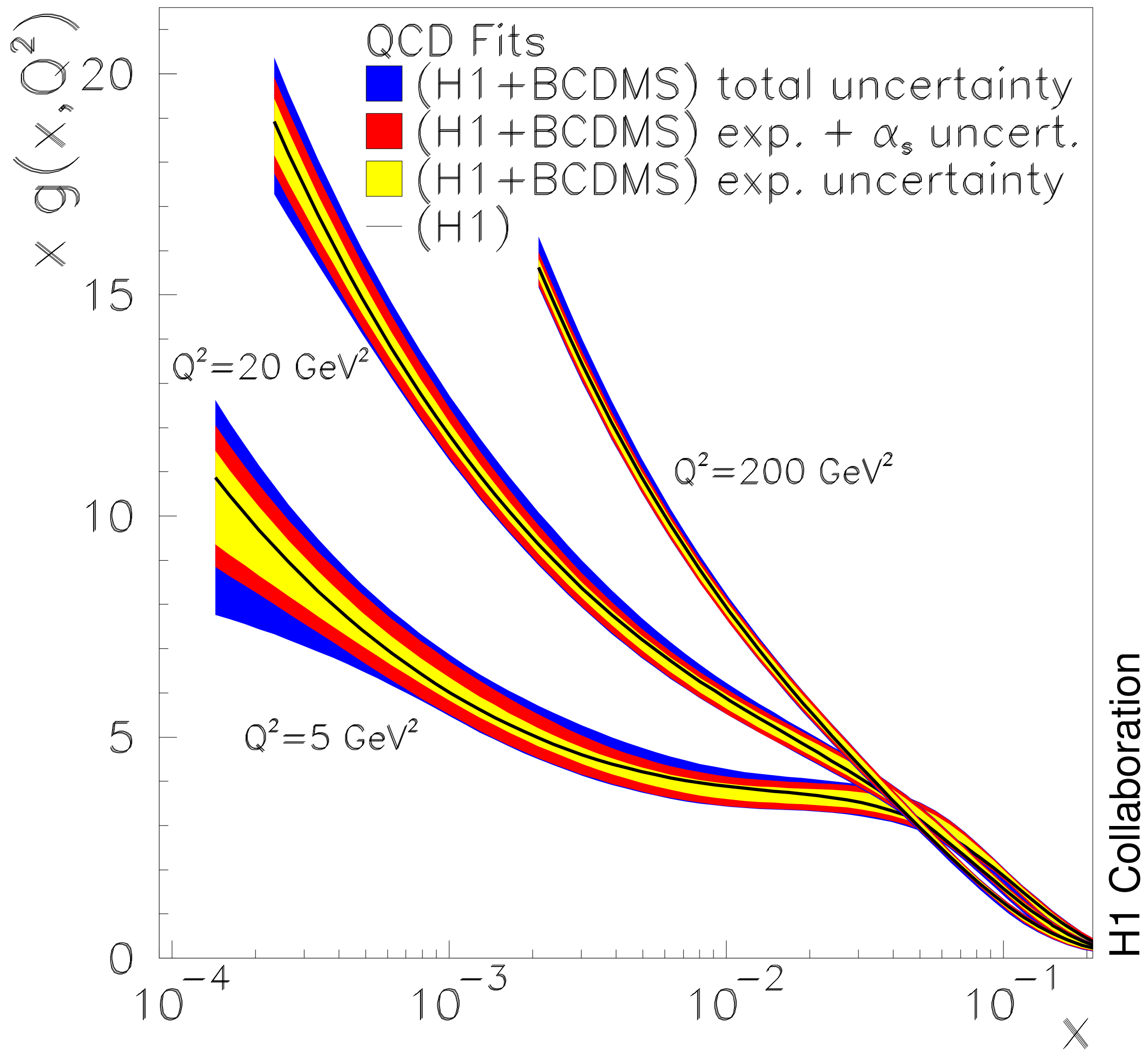

Figure 23: *Gluon distribution resulting from the NLO DGLAP QCD fit to H1 ep and BCDMS μp cross section data in the massive heavy flavour scheme. The innermost error bands represent the experimental error for fixed $\alpha_s(M_Z^2)$ =0.1150. The middle error bands include in addition the contribution due to the simultaneous fit of α_s . The outer error bands also include the uncertainties related to the QCD model and data range. The solid lines inside the error band represent the gluon distribution obtained in the fit to the H1 data alone.*

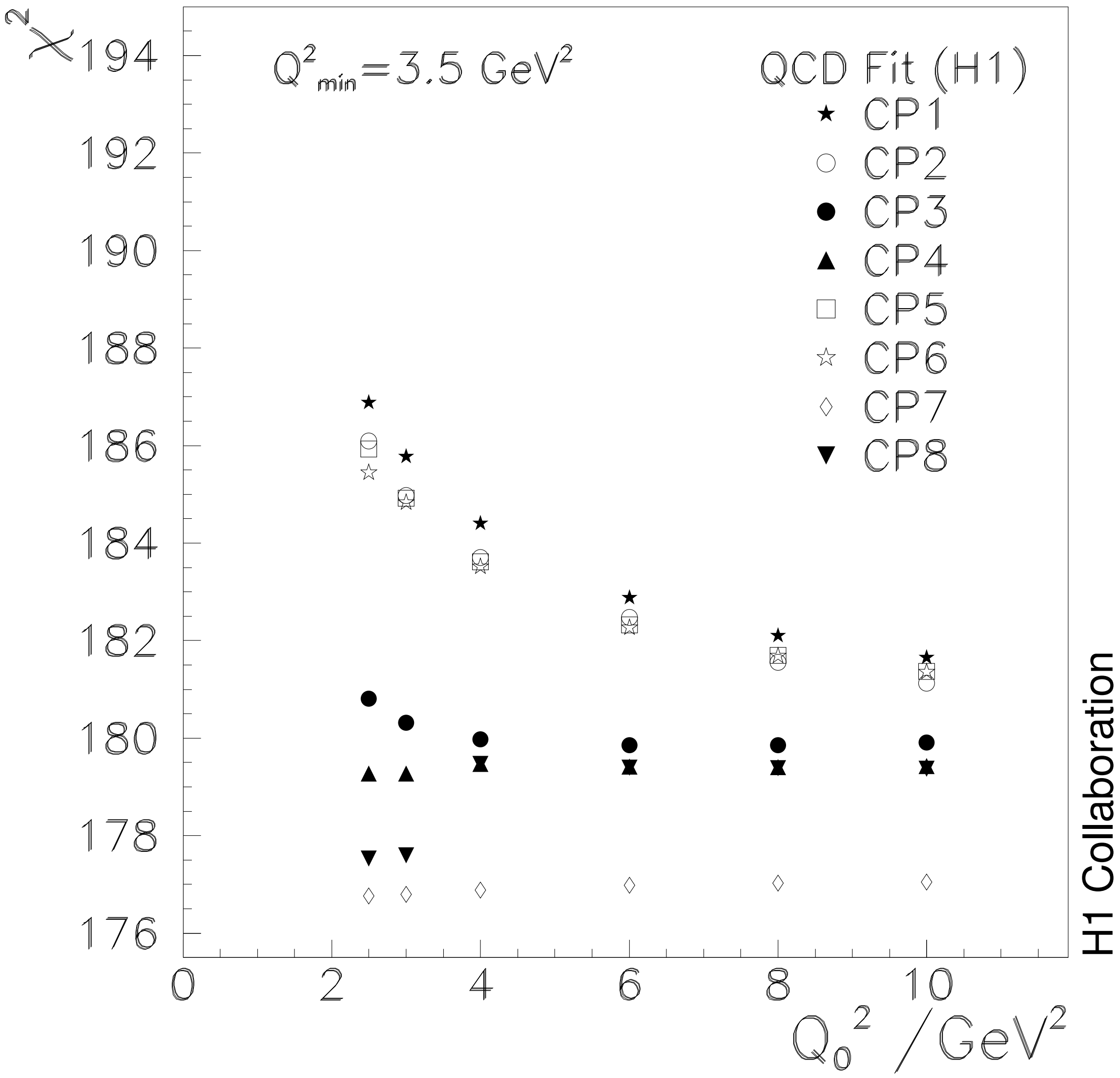

Figure 24: *Dependence of χ^2 on the initial scale parameter Q_0^2 for different parameterisations of the parton distributions xg and A (appendix A.3, table 8) in the NLO QCD fit to the H1 data.*

Q^2/GeV^2	x	y	σ_r	R	F_2	δ_{tot}	δ_{sta}	δ_{unc}	δ_{cor}
1.5	0.0000320	0.518	0.786	0.346	0.832	5.5	1.3	3.5	4.0
1.5	0.0000500	0.331	0.739	0.290	0.752	4.9	1.9	3.9	2.3
1.5	0.0000800	0.207	0.698	0.242	0.702	8.6	4.2	6.8	3.2
2.0	0.0000327	0.675	0.805	–	–	7.4	1.5	6.3	3.6
2.0	0.0000500	0.442	0.823	0.278	0.851	3.5	0.9	2.8	1.9
2.0	0.0000800	0.276	0.740	0.242	0.748	3.5	1.0	2.7	2.0
2.0	0.000130	0.170	0.714	0.209	0.716	3.7	1.3	2.9	1.8
2.0	0.000200	0.111	0.653	0.183	0.654	4.7	1.2	3.0	3.4
2.0	0.000320	0.069	0.625	0.159	0.626	4.4	1.4	3.1	2.8
2.0	0.000500	0.044	0.620	0.139	0.620	5.8	1.5	3.3	4.6
2.0	0.00100	0.022	0.512	0.115	0.513	4.5	1.2	3.0	3.2
2.0	0.00320	0.007	0.424	0.112	0.424	6.6	1.5	4.3	4.7
2.5	0.0000409	0.675	0.899	–	–	7.4	1.6	6.2	3.6
2.5	0.0000500	0.552	0.859	0.276	0.909	3.7	1.3	2.2	2.7
2.5	0.0000800	0.345	0.814	0.246	0.828	2.6	0.9	1.8	1.7
2.5	0.000130	0.212	0.763	0.219	0.767	2.5	0.9	1.6	1.7
2.5	0.000200	0.138	0.690	0.198	0.691	3.0	1.0	2.7	1.1
2.5	0.000320	0.086	0.637	0.177	0.638	3.1	1.0	2.7	1.4
2.5	0.000500	0.055	0.603	0.161	0.603	3.0	1.0	2.7	0.9
2.5	0.000800	0.035	0.555	0.147	0.555	3.1	1.1	2.7	1.1
2.5	0.00158	0.018	0.516	0.137	0.516	2.9	0.8	2.6	1.1
2.5	0.00500	0.005	0.403	0.167	0.403	5.2	1.0	3.9	3.3
3.5	0.0000573	0.675	0.897	–	–	7.0	2.1	6.2	2.6
3.5	0.0000800	0.483	0.928	0.254	0.964	2.9	1.1	1.8	2.1
3.5	0.000130	0.297	0.876	0.233	0.886	2.2	0.9	1.5	1.4
3.5	0.000200	0.193	0.822	0.216	0.826	2.3	0.9	1.5	1.5
3.5	0.000320	0.121	0.760	0.201	0.761	2.6	1.0	1.6	1.7
3.5	0.000500	0.078	0.715	0.188	0.716	2.7	1.0	1.6	1.9
3.5	0.000800	0.048	0.647	0.178	0.647	2.4	1.0	1.7	1.4
3.5	0.00130	0.030	0.601	0.173	0.601	2.6	1.0	1.7	1.7
3.5	0.00251	0.015	0.532	0.176	0.532	2.1	0.8	1.5	1.2
3.5	0.00800	0.005	0.418	0.236	0.418	4.2	0.9	3.3	2.4

Table 9: *The H1 measurement of the reduced deep-inelastic cross section with data taken in a dedicated low Q^2 trigger run in 1997. For $y < 0.6$ the structure function F_2 is extracted using the quoted values of R, derived from a QCD fit to the H1 cross section data. Fractional cross section errors are quoted in %. The total error (δ_{tot}) is the quadratic sum of the uncorrelated (δ_{unc}), the correlated (δ_{cor}) and the experimental statistical error (δ_{sta}).*

Q^2/GeV^2	x	y	σ_r	R	F_2	δ_{tot}	δ_{sta}	δ_{unc}	δ_{cor}
5.0	0.0000818	0.675	1.019	–	–	6.6	2.1	4.8	3.9
5.0	0.000130	0.425	1.015	0.245	1.043	2.4	1.1	1.7	1.4
5.0	0.000200	0.276	0.965	0.232	0.974	2.3	1.0	1.4	1.5
5.0	0.000320	0.173	0.887	0.220	0.890	2.4	1.1	1.6	1.5
5.0	0.000500	0.111	0.791	0.210	0.792	2.3	1.1	1.6	1.4
5.0	0.000800	0.069	0.703	0.202	0.704	2.5	1.1	1.6	1.5
5.0	0.00130	0.043	0.661	0.198	0.661	3.0	1.1	1.6	2.3
5.0	0.00200	0.028	0.621	0.199	0.621	2.5	1.1	1.6	1.5
5.0	0.00398	0.014	0.538	0.213	0.538	2.3	0.9	1.5	1.5
5.0	0.0130	0.004	0.410	0.281	0.410	3.9	1.0	3.2	2.1
6.5	0.000130	0.552	1.089	0.252	1.148	3.5	1.6	1.7	2.6
6.5	0.000200	0.359	1.073	0.241	1.092	2.3	1.1	1.6	1.3
6.5	0.000320	0.224	0.957	0.230	0.963	2.1	1.2	1.4	1.2
6.5	0.000500	0.144	0.875	0.222	0.877	2.7	1.2	1.5	1.8
6.5	0.000800	0.090	0.800	0.215	0.801	2.5	1.2	1.5	1.5
6.5	0.00130	0.055	0.708	0.211	0.708	2.5	1.2	1.5	1.4
6.5	0.00200	0.036	0.672	0.212	0.672	2.7	1.3	1.6	1.7
6.5	0.00398	0.018	0.587	0.223	0.587	2.3	0.9	1.4	1.6
6.5	0.0130	0.005	0.432	0.273	0.432	3.6	1.0	3.2	1.4
8.5	0.000139	0.675	1.097	–	–	4.9	2.1	1.8	4.1
8.5	0.000200	0.470	1.152	0.247	1.193	2.9	1.4	1.6	2.0
8.5	0.000320	0.293	1.080	0.238	1.092	2.5	1.3	1.5	1.6
8.5	0.000500	0.188	0.992	0.231	0.996	2.3	1.3	1.4	1.3
8.5	0.000800	0.118	0.893	0.225	0.894	2.5	1.4	1.5	1.4
8.5	0.00130	0.072	0.797	0.222	0.797	2.8	1.4	1.6	1.8
8.5	0.00200	0.047	0.725	0.222	0.725	2.8	1.4	1.6	1.8
8.5	0.00320	0.029	0.632	0.226	0.632	2.8	1.5	1.6	1.8
8.5	0.00631	0.015	0.565	0.242	0.565	2.3	1.1	1.5	1.3
8.5	0.0200	0.005	0.419	0.268	0.419	4.2	1.2	3.2	2.4
12.0	0.000800	0.166	0.986	0.233	0.989	2.7	1.6	1.6	1.5
12.0	0.00130	0.102	0.878	0.230	0.879	2.3	1.6	1.6	0.6
12.0	0.00200	0.066	0.825	0.229	0.825	2.7	1.6	1.6	1.5
12.0	0.00320	0.041	0.725	0.231	0.725	2.9	1.6	1.6	1.7
12.0	0.00631	0.021	0.613	0.241	0.613	2.4	1.2	1.5	1.5
12.0	0.0200	0.007	0.459	0.249	0.459	4.0	1.4	3.2	1.9

Table 10: *The H1 measurement of the reduced deep-inelastic cross section with data taken in a dedicated low Q^2 trigger run in 1997. For $y < 0.6$ the structure function F_2 is extracted using the quoted values of R, derived from a QCD fit to the H1 cross section data. Fractional cross section errors are quoted in %.*

Q^2/GeV^2	x	y	σ_r	R	F_2	δ_{tot}	δ_{sta}	δ_{unc}	δ_{cor}
12.0	0.000161	0.825	1.226	–	–	5.8	4.1	3.8	1.8
12.0	0.000197	0.675	1.269	–	–	3.5	0.9	2.1	2.7
12.0	0.000320	0.415	1.217	0.245	1.249	2.0	0.6	1.7	1.0
12.0	0.000500	0.266	1.146	0.239	1.156	1.8	0.7	1.4	1.0
15.0	0.000201	0.825	1.255	–	–	5.2	3.2	3.6	1.9
15.0	0.000246	0.675	1.361	–	–	3.3	0.9	2.1	2.4
15.0	0.000320	0.519	1.283	0.249	1.342	2.4	0.7	1.9	1.4
15.0	0.000500	0.332	1.228	0.243	1.247	1.9	0.6	1.6	0.7
15.0	0.000800	0.208	1.115	0.238	1.121	1.7	0.6	1.4	0.8
15.0	0.00130	0.127	0.969	0.234	0.971	2.9	0.6	1.4	2.4
15.0	0.00200	0.083	0.865	0.232	0.866	2.5	0.6	1.5	2.0
15.0	0.00320	0.052	0.774	0.234	0.774	2.5	0.7	1.5	1.9
15.0	0.00500	0.033	0.708	0.237	0.708	2.4	0.8	1.5	1.7
15.0	0.0100	0.017	0.575	0.244	0.575	2.7	0.7	1.4	2.2
15.0	0.0320	0.005	0.453	0.211	0.453	6.4	1.0	3.3	5.5
20.0	0.000268	0.825	1.313	–	–	5.2	3.2	3.6	1.8
20.0	0.000328	0.675	1.383	–	–	2.7	1.0	2.0	1.5
20.0	0.000500	0.443	1.285	0.246	1.324	2.0	0.6	1.6	0.9
20.0	0.000800	0.277	1.178	0.241	1.190	1.8	0.6	1.4	1.0
20.0	0.00130	0.170	1.059	0.237	1.062	1.8	0.6	1.4	1.0
20.0	0.00200	0.111	0.939	0.235	0.940	2.8	0.7	1.4	2.3
20.0	0.00320	0.069	0.819	0.234	0.819	2.3	0.7	1.5	1.7
20.0	0.00500	0.044	0.747	0.235	0.747	2.2	0.8	1.5	1.3
20.0	0.0100	0.022	0.610	0.238	0.610	2.4	0.7	1.4	1.8
20.0	0.0320	0.007	0.455	0.198	0.455	6.8	1.0	3.3	5.9
25.0	0.000335	0.825	1.379	–	–	5.9	4.1	3.9	1.8
25.0	0.000410	0.675	1.371	–	–	2.6	1.2	2.0	1.2
25.0	0.000500	0.553	1.345	0.248	1.417	2.4	1.0	1.8	1.2
25.0	0.000800	0.346	1.242	0.243	1.263	1.9	0.7	1.6	0.9
25.0	0.00130	0.213	1.091	0.238	1.097	1.8	0.7	1.4	0.9
25.0	0.00200	0.138	0.985	0.236	0.987	2.9	0.8	1.4	2.4
25.0	0.00320	0.086	0.879	0.234	0.880	2.8	0.8	1.5	2.2
25.0	0.00500	0.055	0.754	0.234	0.754	2.4	0.9	1.5	1.6
25.0	0.00800	0.034	0.663	0.234	0.663	2.5	0.9	1.5	1.8
25.0	0.0158	0.018	0.547	0.226	0.547	3.7	0.9	1.5	3.3
25.0	0.0500	0.005	0.447	0.148	0.447	7.5	1.3	3.3	6.6
35.0	0.000574	0.675	1.473	–	–	2.7	1.4	2.0	1.2
35.0	0.000800	0.484	1.354	0.244	1.405	2.2	0.9	1.7	1.1
35.0	0.00130	0.298	1.181	0.239	1.195	1.8	0.8	1.4	0.8
35.0	0.00200	0.194	1.031	0.235	1.035	1.8	0.8	1.4	0.8

Table 11: *The H1 measurement of the reduced deep-inelastic cross section with data taken in 1996/97. For* $y < 0.6$ *the structure function* F_2 *is extracted using the quoted values of* R*, derived from a QCD fit to the H1 cross section data. Fractional cross section errors are quoted in %.*

Q^2/GeV^2	x	y	σ_r	R	F_2	δ_{tot}	δ_{sta}	δ_{unc}	δ_{cor}
35.0	0.00320	0.121	0.935	0.233	0.936	3.1	0.9	1.5	2.5
35.0	0.00500	0.077	0.821	0.231	0.821	2.7	0.9	1.5	2.0
35.0	0.00800	0.048	0.719	0.228	0.719	2.4	1.0	1.5	1.6
35.0	0.0130	0.030	0.625	0.222	0.625	3.2	1.1	1.6	2.6
35.0	0.0251	0.015	0.524	0.195	0.524	4.1	1.1	1.6	3.6
35.0	0.0800	0.005	0.413	0.095	0.413	9.2	1.8	3.5	8.3
45.0	0.00130	0.383	1.282	0.238	1.309	1.9	0.9	1.7	0.3
45.0	0.00200	0.249	1.107	0.234	1.115	1.8	0.9	1.4	0.6
45.0	0.00320	0.156	0.979	0.231	0.982	1.8	0.9	1.4	0.7
45.0	0.00500	0.099	0.872	0.228	0.873	2.8	1.1	1.5	2.1
45.0	0.00800	0.062	0.743	0.224	0.743	2.5	1.1	1.5	1.6
45.0	0.0130	0.038	0.649	0.215	0.649	2.8	1.3	1.6	2.0
45.0	0.0251	0.020	0.525	0.187	0.525	4.3	1.2	1.6	3.8
45.0	0.0800	0.006	0.396	0.091	0.396	7.6	2.1	3.5	6.4
60.0	0.00200	0.332	1.245	0.231	1.263	2.1	1.0	1.7	0.7
60.0	0.00320	0.208	1.052	0.227	1.057	1.9	1.1	1.4	0.7
60.0	0.00500	0.133	0.900	0.223	0.902	3.1	1.2	1.6	2.3
60.0	0.00800	0.083	0.803	0.218	0.804	2.8	1.3	1.6	1.9
60.0	0.0130	0.051	0.683	0.208	0.683	2.9	1.4	1.7	2.0
60.0	0.0200	0.033	0.597	0.192	0.597	4.1	1.7	1.8	3.2
60.0	0.0398	0.017	0.506	0.145	0.506	4.7	1.8	1.9	3.9
60.0	0.130	0.005	0.360	0.057	0.360	9.4	3.0	3.8	8.1
90.0	0.00320	0.311	1.107	0.221	1.120	2.6	1.4	1.8	1.2
90.0	0.00500	0.199	0.999	0.216	1.004	2.2	1.3	1.5	0.9
90.0	0.00800	0.124	0.845	0.209	0.846	3.3	1.5	1.7	2.5
90.0	0.0130	0.076	0.728	0.197	0.728	2.8	1.6	1.8	1.4
90.0	0.0200	0.050	0.618	0.180	0.618	3.9	1.8	1.9	2.8
90.0	0.0398	0.025	0.506	0.135	0.506	3.8	2.0	1.9	2.7
90.0	0.130	0.008	0.339	0.053	0.339	4.8	3.3	2.0	2.9
120.0	0.00500	0.266	1.011	0.210	1.019	3.7	2.4	2.1	1.9
120.0	0.00800	0.166	0.839	0.202	0.841	3.0	1.9	1.8	1.4
120.0	0.0130	0.102	0.744	0.190	0.745	4.6	2.1	2.0	3.6
120.0	0.0200	0.066	0.604	0.173	0.605	4.0	2.3	2.1	2.5
120.0	0.0320	0.041	0.558	0.145	0.558	5.8	2.8	2.5	4.5
120.0	0.0631	0.021	0.462	0.094	0.462	4.9	3.0	2.7	2.9
120.0	0.200	0.007	0.312	0.037	0.312	10.6	4.8	4.8	8.2
150.0	0.0200	0.083	0.709	0.167	0.709	8.9	4.4	3.8	6.6
150.0	0.0320	0.052	0.550	0.140	0.550	8.0	5.1	4.1	4.7
150.0	0.0631	0.026	0.418	0.090	0.418	9.0	5.7	4.4	5.4
150.0	0.200	0.008	0.296	0.036	0.296	12.9	8.4	7.1	6.7

Table 12: *The H1 measurement of the reduced deep-inelastic cross section with data taken in 1996/97. For $y < 0.6$ the structure function F_2 is extracted using the quoted values of R, derived from a QCD fit to the H1 cross section data. Fractional cross section errors are quoted in %.*

Q^2/GeV^2	x	y	$(\partial\sigma_r/\partial \ln y)_{Q^2}$	Δ_{sta}	Δ_{sys}	Δ_{tot}
1.5	0.000039	0.425	0.104	0.039	0.080	0.089
1.5	0.000062	0.269	0.088	0.070	0.114	0.134
2.2	0.000045	0.538	0.051	0.017	0.061	0.064
2.2	0.000075	0.325	0.139	0.015	0.025	0.029
2.2	0.000122	0.200	0.126	0.015	0.024	0.028
2.2	0.000194	0.125	0.118	0.018	0.031	0.036
2.2	0.000291	0.083	0.070	0.018	0.026	0.032
2.2	0.000454	0.054	0.082	0.014	0.026	0.030
2.2	0.000748	0.032	0.086	0.018	0.033	0.038
2.2	0.00122	0.020	0.081	0.016	0.039	0.042
2.2	0.00224	0.011	0.100	0.007	0.023	0.024
4.2	0.000086	0.538	0.002	0.031	0.057	0.065
4.2	0.000143	0.325	0.122	0.020	0.033	0.039
4.2	0.000232	0.200	0.148	0.017	0.023	0.029
4.2	0.000371	0.125	0.170	0.020	0.027	0.034
4.2	0.000556	0.083	0.140	0.019	0.019	0.027
4.2	0.000867	0.054	0.118	0.014	0.018	0.023
4.2	0.00143	0.032	0.095	0.014	0.016	0.022
4.2	0.00232	0.020	0.114	0.011	0.013	0.017
4.2	0.00488	0.009	0.106	0.004	0.013	0.013
7.5	0.000154	0.538	-0.004	0.034	0.049	0.059
7.5	0.000255	0.325	0.218	0.028	0.024	0.037
7.5	0.000414	0.200	0.193	0.024	0.031	0.039
7.5	0.000663	0.125	0.182	0.028	0.027	0.039
7.5	0.000992	0.083	0.203	0.026	0.021	0.034
7.5	0.00155	0.054	0.127	0.019	0.018	0.026
7.5	0.00255	0.032	0.189	0.024	0.021	0.032
7.5	0.00414	0.020	0.079	0.019	0.021	0.029
7.5	0.00764	0.011	0.149	0.008	0.016	0.018
7.5	0.0155	0.005	0.081	0.013	0.012	0.018
13.5	0.000199	0.748	-0.399	0.167	0.191	0.253
13.5	0.000277	0.538	0.151	0.018	0.051	0.054
13.5	0.000459	0.325	0.182	0.015	0.024	0.028
13.5	0.000746	0.200	0.299	0.016	0.054	0.056
13.5	0.00119	0.125	0.295	0.037	0.043	0.057
13.5	0.00179	0.083	0.148	0.037	0.035	0.051
13.5	0.00279	0.054	0.173	0.012	0.014	0.018
13.5	0.00459	0.032	0.203	0.019	0.017	0.025
13.5	0.00746	0.020	0.145	0.018	0.027	0.032
13.5	0.0137	0.011	0.135	0.010	0.015	0.018
13.5	0.0279	0.005	0.045	0.015	0.035	0.038

Table 13: *The H1 measurement of the cross section derivative* $(\partial\sigma_r/\partial \ln y)_{Q^2} = -(\partial\sigma_r/\partial \ln x)_{Q^2}$ *calculated at fixed* Q^2*. The errors are given in absolute values. The data below 13.5 GeV*^{2} *belong to the special low* Q^2 *run taken in 1997. The data at larger* Q^2 *were taken in 1996/97.*

Q^2/GeV^2	x	y	$(\partial\sigma_r/\partial\ln y)_{Q^2}$	Δ_{sta}	Δ_{sys}	Δ_{tot}
22.5	0.000332	0.748	-0.216	0.181	0.176	0.253
22.5	0.000462	0.538	0.198	0.020	0.032	0.037
22.5	0.000765	0.325	0.272	0.017	0.021	0.027
22.5	0.00124	0.200	0.249	0.014	0.032	0.035
22.5	0.00199	0.125	0.256	0.017	0.034	0.038
22.5	0.00298	0.083	0.277	0.016	0.026	0.031
22.5	0.00465	0.054	0.184	0.012	0.016	0.020
22.5	0.00765	0.032	0.185	0.013	0.024	0.027
22.5	0.0124	0.020	0.182	0.012	0.021	0.025
22.5	0.0229	0.011	0.099	0.007	0.025	0.027
40.0	0.000822	0.538	0.335	0.042	0.045	0.062
40.0	0.00136	0.325	0.386	0.023	0.026	0.034
40.0	0.00221	0.200	0.311	0.017	0.014	0.022
40.0	0.00354	0.125	0.204	0.021	0.058	0.062
40.0	0.00529	0.083	0.263	0.021	0.026	0.033
40.0	0.00826	0.054	0.206	0.015	0.019	0.024
40.0	0.0136	0.032	0.179	0.019	0.027	0.033
40.0	0.0221	0.020	0.163	0.016	0.017	0.024
40.0	0.0407	0.011	0.124	0.012	0.023	0.026
40.0	0.0826	0.005	0.039	0.022	0.024	0.032
75.0	0.00255	0.325	0.442	0.035	0.029	0.045
75.0	0.00414	0.200	0.303	0.024	0.024	0.034
75.0	0.00663	0.125	0.271	0.037	0.042	0.056
75.0	0.00992	0.083	0.222	0.036	0.038	0.053
75.0	0.0155	0.054	0.232	0.018	0.031	0.036
75.0	0.0255	0.032	0.177	0.026	0.028	0.038
75.0	0.0414	0.020	0.102	0.027	0.033	0.042
75.0	0.0764	0.011	0.152	0.019	0.019	0.027
75.0	0.155	0.005	0.099	0.029	0.038	0.048
135.0	0.00746	0.200	0.352	0.055	0.045	0.071
135.0	0.0119	0.125	0.176	0.054	0.088	0.103
135.0	0.0179	0.083	0.292	0.049	0.041	0.064
135.0	0.0279	0.054	0.140	0.035	0.052	0.063
135.0	0.0459	0.032	0.161	0.039	0.032	0.050

Table 14: *The H1 measurement of the cross section derivative* $(\partial\sigma_r/\partial\ln y)_{Q^2} = -(\partial\sigma_r/\partial\ln x)_{Q^2}$ *calculated at fixed* Q^2*.* Δ_{sta} *denotes the uncertainty due to the data statistics. The uncertainties are given in absolute values.*

Q^2/GeV^2	x	y	$F_L(x,Q^2)$	δ_{sta}	δ_{sys}	δ_{met}	δ_{tot}
2.2	0.000045	0.538	0.100	0.030	0.107	0.025	0.114
4.2	0.000086	0.538	0.273	0.055	0.101	0.027	0.118
7.5	0.000154	0.538	0.385	0.058	0.088	0.039	0.112
12.0	0.000161	0.825	0.429	0.076	0.095	0.045	0.130
12.0	0.000197	0.675	0.411	0.027	0.136	0.058	0.150
12.0	0.000320	0.415	0.456	0.054	0.279	0.096	0.300
15.0	0.000201	0.825	0.453	0.061	0.092	0.042	0.118
15.0	0.000246	0.675	0.285	0.030	0.124	0.053	0.138
15.0	0.000320	0.519	0.417	0.040	0.194	0.069	0.210
20.0	0.000268	0.825	0.426	0.064	0.093	0.036	0.118
20.0	0.000328	0.675	0.315	0.035	0.119	0.045	0.132
20.0	0.000500	0.443	0.385	0.055	0.249	0.064	0.263
25.0	0.000335	0.825	0.360	0.085	0.098	0.030	0.134
25.0	0.000410	0.675	0.377	0.039	0.116	0.038	0.128
25.0	0.000500	0.553	0.404	0.055	0.164	0.047	0.179
35.0	0.000574	0.675	0.149	0.049	0.115	0.029	0.128
35.0	0.000800	0.484	0.239	0.064	0.213	0.047	0.228

Table 15: *The H1 determination of the longitudinal structure function $F_L(x,Q^2)$. The errors are given in absolute, δ_{sta} representing the experimental statistics. The systematic errors consider all contributions from correlated and uncorrelated systematic error sources. δ_{met} is due to the uncertainties connected with the representation of F_2 in the derivative method, for $Q^2 < 10$ GeV^2 , and in the QCD extrapolation method, for $Q^2 > 10$ GeV^2 .*

Q^2/GeV^2	x	y	$(\partial F_2/\partial \ln Q^2)_x$	Δ_{sta}	Δ_{sys}	Δ_{tot}
1.7	0.00005	0.383	0.342	0.055	0.097	0.112
2.2	0.00005	0.495	0.261	0.062	0.094	0.113
1.7	0.00008	0.240	0.159	0.106	0.164	0.196
2.2	0.00008	0.309	0.359	0.046	0.064	0.079
3.0	0.00008	0.409	0.403	0.037	0.066	0.076
2.2	0.00013	0.190	0.228	0.052	0.075	0.091
3.0	0.00013	0.252	0.355	0.031	0.034	0.046
4.2	0.00013	0.356	0.439	0.039	0.036	0.052
5.7	0.00013	0.485	0.399	0.081	0.081	0.115
2.2	0.00020	0.124	0.166	0.046	0.115	0.124
3.0	0.00020	0.164	0.400	0.030	0.048	0.057
4.2	0.00020	0.232	0.417	0.035	0.029	0.046
5.7	0.00020	0.316	0.450	0.060	0.043	0.074
7.4	0.00020	0.411	0.374	0.078	0.069	0.104
2.2	0.00032	0.077	0.054	0.047	0.105	0.115
3.0	0.00032	0.102	0.366	0.029	0.047	0.055
4.2	0.00032	0.145	0.362	0.035	0.036	0.050
5.7	0.00032	0.197	0.276	0.057	0.084	0.102
7.4	0.00032	0.257	0.482	0.067	0.049	0.083
10.1	0.00032	0.349	0.453	0.045	0.048	0.066
13.4	0.00032	0.464	0.415	0.052	0.090	0.104
2.2	0.00050	0.050	-0.076	0.049	0.148	0.156
3.0	0.00050	0.065	0.334	0.027	0.048	0.056
4.2	0.00050	0.093	0.214	0.031	0.032	0.045
5.7	0.00050	0.126	0.325	0.052	0.049	0.071
7.4	0.00050	0.165	0.445	0.063	0.093	0.113
10.1	0.00050	0.224	0.464	0.044	0.039	0.059
13.4	0.00050	0.297	0.403	0.047	0.064	0.080
17.3	0.00050	0.383	0.270	0.039	0.046	0.060
22.4	0.00050	0.495	0.417	0.076	0.091	0.119
2.2	0.00080	0.031	0.119	0.039	0.094	0.102
3.0	0.00080	0.041	0.275	0.026	0.041	0.049
4.2	0.00080	0.058	0.158	0.028	0.041	0.050
5.7	0.00080	0.079	0.369	0.048	0.040	0.062
7.4	0.00080	0.103	0.349	0.059	0.043	0.073
10.1	0.00080	0.140	0.276	0.057	0.041	0.070
13.4	0.00080	0.186	0.586	0.075	0.108	0.131
17.3	0.00080	0.240	0.240	0.034	0.038	0.051
22.4	0.00080	0.309	0.328	0.050	0.052	0.072
29.6	0.00080	0.409	0.423	0.045	0.044	0.062

Table 16: *The H1 Measurement of the derivative* $(\partial F_2/\partial \ln Q^2)_x$. Δ_{sta} *denotes the uncertainty due to the data statistics. The uncertainties are given in absolute values.*

Q^2/GeV^2	x	y	$(\partial F_2/\partial \ln Q^2)_x$	Δ_{sta}	Δ_{sys}	Δ_{tot}
3.0	0.0013	0.025	0.205	0.023	0.040	0.046
4.2	0.0013	0.036	0.168	0.027	0.033	0.043
5.7	0.0013	0.049	0.181	0.044	0.042	0.061
7.4	0.0013	0.063	0.330	0.053	0.044	0.069
10.1	0.0013	0.086	0.239	0.051	0.047	0.069
13.4	0.0013	0.114	0.409	0.067	0.096	0.117
17.3	0.0013	0.147	0.318	0.032	0.110	0.114
22.4	0.0013	0.190	0.154	0.045	0.043	0.062
29.6	0.0013	0.252	0.291	0.035	0.032	0.048
39.7	0.0013	0.338	0.454	0.060	0.058	0.084
4.2	0.0020	0.023	0.185	0.023	0.029	0.037
5.7	0.0020	0.032	0.194	0.042	0.039	0.058
7.4	0.0020	0.041	0.200	0.049	0.048	0.069
10.1	0.0020	0.056	0.289	0.048	0.034	0.059
13.4	0.0020	0.074	0.183	0.064	0.058	0.086
17.3	0.0020	0.096	0.258	0.030	0.041	0.050
22.4	0.0020	0.124	0.209	0.044	0.054	0.070
29.6	0.0020	0.164	0.145	0.033	0.085	0.091
39.7	0.0020	0.220	0.318	0.050	0.040	0.064
52.0	0.0020	0.288	0.513	0.057	0.052	0.077
5.7	0.0032	0.020	0.200	0.029	0.027	0.040
7.4	0.0032	0.026	0.064	0.041	0.044	0.060
10.1	0.0032	0.035	0.270	0.043	0.034	0.055
13.4	0.0032	0.046	0.219	0.058	0.056	0.081
17.3	0.0032	0.060	0.157	0.028	0.033	0.044
22.4	0.0032	0.077	0.271	0.041	0.053	0.067
29.6	0.0032	0.102	0.167	0.032	0.036	0.048
39.7	0.0032	0.137	0.182	0.050	0.103	0.114
52.0	0.0032	0.180	0.261	0.051	0.041	0.065
73.5	0.0032	0.254	0.156	0.047	0.054	0.071
10.1	0.0050	0.022	0.153	0.030	0.022	0.038
13.4	0.0050	0.030	0.265	0.043	0.043	0.061
17.3	0.0050	0.038	0.137	0.027	0.033	0.043
22.4	0.0050	0.050	0.029	0.039	0.050	0.064
29.6	0.0050	0.065	0.200	0.030	0.032	0.044
39.7	0.0050	0.088	0.206	0.048	0.045	0.066
52.0	0.0050	0.115	0.101	0.051	0.042	0.066
73.5	0.0050	0.163	0.251	0.042	0.072	0.083
103.9	0.0050	0.230	0.054	0.095	0.089	0.130

Table 17: *The H1 measurement of the derivative* $(\partial F_2/\partial \ln Q^2)_x$. Δ_{sta} *denotes the uncertainty due to the data statistics. The uncertainties are given in absolute values.*

Q^2/GeV^2	x	y	$(\partial F_2/\partial \ln Q^2)_x$	Δ_{sta}	Δ_{sys}	Δ_{tot}
17.3	0.008	0.024	0.138	0.021	0.025	0.033
22.4	0.008	0.031	0.074	0.034	0.056	0.065
29.6	0.008	0.041	0.166	0.028	0.029	0.040
39.7	0.008	0.055	0.098	0.044	0.039	0.059
52.0	0.008	0.072	0.209	0.047	0.039	0.061
73.5	0.008	0.102	0.105	0.041	0.037	0.055
103.9	0.008	0.144	-0.017	0.072	0.098	0.122
29.6	0.013	0.025	0.148	0.026	0.027	0.037
39.7	0.013	0.034	0.095	0.044	0.046	0.063
52.0	0.013	0.044	0.117	0.045	0.036	0.057
73.5	0.013	0.063	0.113	0.038	0.037	0.053
103.9	0.013	0.088	0.058	0.068	0.089	0.112
39.7	0.020	0.022	0.014	0.037	0.033	0.050
52.0	0.020	0.029	0.136	0.043	0.042	0.060
73.5	0.020	0.041	0.053	0.037	0.030	0.048
103.9	0.020	0.058	-0.047	0.062	0.057	0.084
134.2	0.020	0.074	0.463	0.153	0.221	0.268
73.5	0.032	0.025	0.008	0.035	0.045	0.057
103.9	0.032	0.036	0.074	0.065	0.070	0.096
134.2	0.032	0.046	-0.038	0.141	0.143	0.201
134.2	0.050	0.030	-0.205	0.131	0.116	0.175

Table 18: *The H1 measurement of the derivative* $\partial F_2/\partial \ln Q^2$. Δ_{sta} *denotes the uncertainty due to the data statistics. The uncertainties are given in absolute values.*